

## **NOTE TO USERS**

**This reproduction is the best copy available.**

**UMI<sup>®</sup>**



**TOTAL MARROW IRRADIATION USING  
HELICAL TOMOTHERAPY**

by

Lourdes Maria Garcia-Fernandez, M.Sc.

A thesis submitted to the  
Faculty of Graduate Studies and Research  
in partial fulfillment of the requirements  
for the degree of  
Doctor of Philosophy

Ottawa-Carleton Institute for Physics  
Department of Physics, Carleton University

Ottawa, Ontario, Canada

November 2009

© Copyright 2010, Lourdes M. Garcia-Fernandez



Library and Archives  
Canada

Published Heritage  
Branch

395 Wellington Street  
Ottawa ON K1A 0N4  
Canada

Bibliothèque et  
Archives Canada

Direction du  
Patrimoine de l'édition

395, rue Wellington  
Ottawa ON K1A 0N4  
Canada

*Your file* *Votre référence*  
ISBN: 978-0-494-63848-4  
*Our file* *Notre référence*  
ISBN: 978-0-494-63848-4

**NOTICE:**

The author has granted a non-exclusive license allowing Library and Archives Canada to reproduce, publish, archive, preserve, conserve, communicate to the public by telecommunication or on the Internet, loan, distribute and sell theses worldwide, for commercial or non-commercial purposes, in microform, paper, electronic and/or any other formats.

The author retains copyright ownership and moral rights in this thesis. Neither the thesis nor substantial extracts from it may be printed or otherwise reproduced without the author's permission.

---

In compliance with the Canadian Privacy Act some supporting forms may have been removed from this thesis.

While these forms may be included in the document page count, their removal does not represent any loss of content from the thesis.

**AVIS:**

L'auteur a accordé une licence non exclusive permettant à la Bibliothèque et Archives Canada de reproduire, publier, archiver, sauvegarder, conserver, transmettre au public par télécommunication ou par l'Internet, prêter, distribuer et vendre des thèses partout dans le monde, à des fins commerciales ou autres, sur support microforme, papier, électronique et/ou autres formats.

L'auteur conserve la propriété du droit d'auteur et des droits moraux qui protègent cette thèse. Ni la thèse ni des extraits substantiels de celle-ci ne doivent être imprimés ou autrement reproduits sans son autorisation.

---

Conformément à la loi canadienne sur la protection de la vie privée, quelques formulaires secondaires ont été enlevés de cette thèse.

Bien que ces formulaires aient inclus dans la pagination, il n'y aura aucun contenu manquant.

  
**Canada**

# Abstract

Clinical dose response data of human tumours are limited or restricted to a radiation dose range determined by the level of toxicity to the normal tissues. This is the case for the most common disseminated plasma cell neoplasm, multiple myeloma, where the maximum dose deliverable to the entire bony skeleton using a standard total body irradiation (TBI) technique is limited to about 12 Gy. This study is part of scientific background of a *phase I/II* dose escalation clinical trial for multiple myeloma using image-guided intensity modulated radiotherapy (IG-IMRT) to deliver high dose to the entire volume of bone marrow with Helical TomoTherapy (HT). This relatively new technology can deliver highly conformal dose distributions to complex target shapes while reducing the dose to critical normal tissues.

In this study tools for comparing and predicting the effectiveness of different approaches to total marrow irradiation (TMI) using HT were provided. The expected dose response for plasma cell neoplasms was computed and a radiobiological evaluation of different treatment cohorts in a dose escalating study was performed. Normal tissue complication probability (NTCP) and tumour control probability (TCP) models were applied to an actual TMI treatment plan for a patient and the implications of using different longitudinal field widths were assessed. The optimum dose was ~39 Gy for which a predicted tumour control of 95% ( $\pm 3\%$ ) was obtained, with a predicted 3% (0, 8%) occurrence of radiation pneumonitis. Tissue sparing was seen by using smaller field widths only in the organs of the head. This suggests it would be beneficial to use the small fields in the head only since using small fields for the whole treatment would lead to long treatment times.

In TMI it may be necessary to junction two longitudinally adjacent treatment volumes to form a contiguous planning target volume PTV. For instance, this is the case when a different SUP-INF spatial resolution is required or when the PTV length exceeds the bed travel distance. In this work, the dosimetric challenges associated with junctioning longitudinally adjacent PTVs with HT were analyzed and the feasibility of PTV junctioning was demonstrated. The benefits of spatially dividing or splitting the treatment into a few sub-treatments along the longitudinal direction were also investigated.

# Acknowledgements

I would like to express my sincere gratitude to my thesis supervisors, Dr. David Wilkins and Dr. G. Peter Raaphorst for the guidance and support provided throughout the course of this work. This thesis would not appear in its present form without the kind assistance and insightful suggestion of Dr. Lee Gerig. To all of you thank you for the constant encouragement and supervision.

I am also grateful to Dr. Balazs Nyiri for his advices and useful discussions. I would also like to thank Dr. Harold L. Atkins, Dr. Rajiv Samant and Lynn Montgomery for their valuable inputs.

I would like to express my sincere thanks to all people in the Medical Physics Department at the Ottawa Hospital Cancer Centre for making my stay enjoyable and memorable.

I would like to thank my professors at Carleton University for sharing their knowledge and constant support.

I especially want to recognize the support of my colleagues and friends for their advices and valuable feedbacks. In no particular order I extend my gratitude to, Arturo Cardenas, Elena Gil, Sorina Truica, Jared Strydhorst, and Amanda Cherpak.

Thanks from my heart to my family, for their love, support and encouragement. The greatest thanks to my daughter Daniela for her unconditional understanding when instead of playing or reading a good night story I was studying or working.

Thank you all.

# Contents

<b>Abstract</b>	<b>ii</b>
<b>Acknowledgements</b>	<b>iv</b>
<b>Contents</b>	<b>vi</b>
<b>List of Tables</b>	<b>x</b>
<b>List of Figures</b>	<b>xii</b>
<b>Glossary</b>	<b>xviii</b>
<b>1. Introduction</b>	<b>1</b>
1.1 Multiple myeloma.....	1
1.2 Radiation in multiple myeloma.....	2
1.3 Helical TomoTherapy.....	4

1.4 Objectives.....	8
<b>2. Radiation dose response of plasma cell neoplasms</b>	<b>10</b>
2.1 Introduction.....	10
2.2 Study selection criteria.....	13
2.3 Dose response model.....	17
2.4 Maximum likelihood method.....	19
2.4.1 Variance and confidence region of the MLE.....	22
2.4.2 Maximum likelihood estimators for TCP.....	27
2.4.3 Uncertainty analysis based on Monte Carlo.....	30
2.5 Results.....	33
2.5.1 Compiled clinical data.....	33
2.5.2 ML fit of the clinical data.....	38
2.6 Discussion.....	45
<b>3. Radiobiological modeling of a proposed dose escalation in TMI</b>	<b>49</b>
3.1 Introduction.....	49
3.2 Materials and methods.....	50
3.2.1 Dose escalation study in a patient.....	50
3.2.2 Normal tissue complication probability.....	53
3.2.3 Tumour control probability.....	55
3.3 Results.....	55
3.3.1 Dose distribution and DVHs.....	55
3.3.2 Tumour control probabilities in TMI.....	58

3.3.3 Normal tissue complication probabilities in TMI.....	60
3.4 Discussion.....	60
<b>4. Junctioning longitudinally adjacent PTVs with Helical TomoTherapy</b>	<b>67</b>
4.1 Introduction.....	67
4.2 Materials and methods.....	69
4.2.1 Geometry and setup.....	70
4.2.2 Treatment planning procedure.....	73
4.3 Results.....	74
4.3.1 Penumbral slope.....	74
4.3.2 Field width, pitch and off-axis distance effects on dose gradients..	77
4.3.3 Matching fields of equal width.....	79
4.3.4 Matching fields of different widths.....	86
4.3.5 Pitch and on/off-axis dependences.....	93
4.4 Discussion.....	94
<b>5. Optimum frequency of spatial registration in image guided radiation therapy in TMI</b>	<b>101</b>
5.1 Introduction.....	101
5.2 Materials and methods.....	105
5.2.1 Geometry and setup.....	105
5.2.2 Treatment planning procedure.....	111
5.2.3 Radiobiological assessment.....	112
5.3 Results.....	113
5.4 Discussion.....	119

<b>6. Conclusions and future directions</b>	<b>125</b>
6.1 Summary.....	125
6.2 Conclusions of Chapter 2.....	127
6.3 Conclusions of Chapter 3.....	127
6.4 Conclusions of Chapter 4.....	128
6.5 Conclusions of Chapter 5.....	129
6.6 Future directions.....	129
<b>Appendix A. TMI clinical trial overview</b>	<b>131</b>
A.1 Study aim and rationale.....	132
A.2 Treatment overview.....	133
A.3 TMI radiobiological modeling.....	134
<b>Appendix B. Conferences and publications</b>	<b>136</b>
<b>References</b>	<b>137</b>

# List of Tables

2.1	Example of the dose range selection criteria for Strojan <i>et al.</i> data.....	14
2.2	Clinical data for solitary plasmacytomas used in this study. Median dose, LC rate, number of patients treated, 95% CI for binomial proportion, the dose range and the references to the original paper.....	34
2.3	The TCP parameters $D_{50}$ and $\gamma_{50}$ from the ML fit and their symmetric errors (SD) for EMP, SPB and SPB+EMP clinical data. The 95% CI from Monte Carlo analysis (the lower and upper limits: [LL, UL]). Similarly the resulting values for SPB data but including 12 Gy zero local control TBI data point (SPB*).....	40
3.1	Normal tissue tolerance parameters and end published by Burman <i>et al.</i> <sup>39, 40</sup> The $TD_{50}$ is the tolerance dose to the whole organ that would yield a complication probability of 50%, $m$ is a measure of the slope of the dose-response relationship and $n$ describes the volume effect. The end points for which the parameters were calculated are also shown.....	54

3.2	Doses for 80%, 50% and 10% of the volume ( $D_{80}$ , $D_{50}$ and $D_{10}$ ) from 20 Gy TMI and 12 Gy TBI plans in lung.....	58
3.3	TCP values of a 20 Gy TMI plan for 25 mm and 50 mm field widths and uniform dose of 20 Gy. TCP values were obtained from applying Poisson model to the tumour dose distribution in a TMI patient.....	58
4.1	Planned and measured CC penumbral slopes, on- and off-axis, for 50 mm field width and pitch of 0.3.....	78
4.2	Planned and measured CC penumbral slopes, on- and off-axis, for 25 mm field width and pitch of 0.3.....	78
4.3	On- and off-axis dose gradients at 50% of $D_p$ for 25 mm and 50 mm fields and pitches of 0.3 and 0.45.....	79
4.4	On-axis PTVJ mean, SD, Min and Max doses, and SM depending on junction spacing from matching equal fields of 25 mm or 50 mm, and pitch of 0.3.....	81
4.5	On-axis PTVJ mean, SD, Min and Max doses, and SM depending on junction spacing from matching different fields of 25 mm and 50 mm, and pitch of 0.3.....	86
5.1	$D_{80}$ , $D_{50}$ , $D_{20}$ and $D_{10}$ of 20 Gy plan for iPRV with a maximum margin of 10 mm and 50 mm field for the cases of no-junction, one-junction and two-junctions.....	114
5.2	TCP and NTCP for iPTV and iPRV for a 20 Gy plan and no-junction. Maximum margins of 5 mm, 10 mm and 15 mm and different field widths of 25 mm and 50 mm are shown.....	118
5.3	TCP and NTCP for iPTV and iPRV for a 20 Gy plan and one-junction. Maximum margins of 5 mm, 10 mm and 15 mm and different field widths of 25 mm and 50 mm are shown.....	118
5.4	TCP and NTCP for iPTV and iPRV for a 20 Gy plan and two-junctions. Maximum margins of 5 mm, 10 mm and 15 mm and different field widths of 25 mm and 50 mm are shown.....	118
A.1	Investigators involved in the TMI clinical trial and their field of expertise.....	132

# List of Figures

1.1	TomoTherapy system. <i>Figure courtesy of TomoTherapy Inc</i> .....	5
1.2	Conventional axes direction, the fan-beam and field width definition. Notice that the field width is defined along the longitudinal direction (along Y axis).....	5
2.1	Graphical illustration of the meaning of parameters $D_{50}$ and $\gamma_{50}$ in a TCP Poisson model.....	19
2.2	Graphical illustration of $\ln L$ function as a function of $\theta$ with the MLE and the corresponding standard deviation.....	25
2.3	Histogram of the number of patients per dose range for EMP, SPB and SPB+EMP.....	37
2.4	LC clinical data and ML fit as a function of the radiation dose for patients with EMP. Error bars represent the 68% CI for a binomial proportion.....	39

2.5	LC clinical data and ML fit as a function of the radiation dose for patients with SPB. Error bars represent the 68% CI for a binomial proportion.....	39
2.6	LC clinical data and ML fit as a function of the radiation dose for patients with SPB+EMP. Error bars represent the 68% CI for a binomial proportion.....	40
2.7	MLEs from fitting the LC clinical data for EMP (star), SPB (square) and SPB+EMP (circle). The corresponding 68% (inner curves) and 95% (outer curves) CRs are also shown.....	41
2.8	2D MC histogram of parameters $D_{50}$ and $\gamma_{50}$ for EMP.....	42
2.9	Colour map of the 2D MC histograms for SPB and EMP on the parameter space. The likelihood CRs are represented by the white curves. The inner and outer curves represent the 68% and 95% likelihood CRs respectively.....	42
2.10	Histograms for parameters $D_{50}$ (a) and $\gamma_{50}$ (b) obtained from MC experiment.....	44
3.1	Coronal view of a TMI plan to a $D_P$ of 20 Gy. The dose distribution is also shown (Isodoses from 6 to 21.4 Gy).....	57
3.2	DVHs for some normal organs: Left lung (blue), left kidney (green), liver (cyan), brain (pink), oral cavity (yellow), lens (black). The DVH for the GTV is in red. The two dashed lines at the dose of 20 Gy and 87% of the volume show that the plan of delivering 20 Gy to 87% of the GTV was achieved.....	57
3.3	GTV differential DVHs for a patient receiving 20 Gy TMI for 25 mm (red) and 50 mm (blue) field widths. The 25 mm field resulted in a more homogeneous dose distribution to the target than 50 mm field width.....	59
3.4	TCP curves as a function of $D_P$ for TMI treatment with 25 and 50 mm field widths. TCP curves as a function of $D_P$ for TMI treatment with 25 mm (red) and 50 mm (blue) field widths. The curves exhibited little variation. The curves were obtained using Poisson model and linearly escalating the DVHs to any prescribed dose.....	59

3.5	NTCP curves as a function of the $D_p$ for TMI treatment with 25 (solid) and 50 mm (dashed) field widths. The major normal organs, in the torso (a) and the head (b). There was not a substantial difference between NTCP values using 25 mm or 50 mm field widths for most of the organs in the torso. The normal tissue sparing effect is seen by using smaller fields (25 mm) in the organs of the head. The curves were obtained using Lyman model and linearly escalating the DVHs to any prescribed dose.....	62
3.6	The curves of NTCP, TCP and the probability of uncomplicated cure $TCP(1-NTCP)$ as a function of $D_p$ for 50 mm field width for left lung. The curves were obtained using Poisson and Lyman models and linearly escalating the DVHs to any prescribed dose.	64
4.1	Axial (a), coronal (b) and sagittal (c) views of the phantom, PTVs, and isodose distribution calculated by the TPS for 25 mm field and pitch of 0.3.....	71
4.2	Scheme of PTVJ definition within the junction region.....	72
4.3	Comparison of on- and off-axis PTVs dose profiles for 50 mm field width for deliveries with a pitch of 0.3 obtained in this study (a).The 3D planned dose distribution is in part (b). The arrows show where the profiles where taken along the Y direction at X of -94 mm (right), 0 mm (on-axis) and +94 mm (left). Z=0.....	75
4.4	Comparison of on-axis planned and measured dose profiles for 50 mm field width for deliveries with a pitch of 0.3.....	77
4.5	Comparison of on-axis dose profiles depending on junction spacing resulting from matching fields of equal width of 25 mm (a) or 50 mm (b) for deliveries with a pitch of 0.3.....	80
4.6	DVHs for on-axis PTVJ arising from the matching of equal fields of 25 mm (a) and 50 mm (b) for deliveries with a pitch of 0.3. The references represent the DVH for continuous field (no junction)...	82
4.7	Normalized differential DVHs for on-axis PTVJ arising from the matching of equal fields (optimal JSpac) are represented by solid lines for fields of 25 mm (a) and 50 mm (b) for deliveries with a pitch of 0.3. Corresponding references for on-axis PTV are shown in dashed lines.....	85

4.8	Comparison of on-axis dose profiles depending on junction spacing resulting from matching fields of different widths of 25 mm and 50 mm for deliveries with a pitch of 0.3 (a). Detailed representation of on-axis profiles for fields widths of 25 and 50 mm (black and red curves). In green the summed profile for JSpac of 36 mm is shown .....	87
4.9	DVHs for on-axis PTVJ arising from the matching of two different fields of 25 mm and 50 mm for deliveries with a pitch of 0.3.....	88
4.10	Normalized differential DVH for on-axis PTVJ arising from the matching of different fields of 25 mm and 50 mm (optimal JSpac) for deliveries with a pitch of 0.3.....	88
4.11	INF end of the PTV simulated profiles for field widths of 25 mm and 50 mm, and the simulated stepped dose profiles from breaking the PTVs into smaller subPTVs for deliveries with 25 mm field width.....	90
4.12	Comparison of on-axis dose profiles depending on junction spacing resulting from matching fields of different widths of 25 mm (4-steps) and 50 mm for deliveries with a pitch of 0.3.....	90
4.13	DVHs for on-axis PTVJ arising from the matching of two different fields of 25 mm (4-steps) and 50 mm for deliveries with a pitch of 0.3.....	91
4.14	Isodose maps from the matching of equal fields of 50 mm width (a), different fields of 25 mm and 50mm (b), and different fields of 25 mm (4-steps) and 50mm (c). The figures represent the dose distribution for the optimal JSpac corresponding to 48 mm (a), 36 mm (b) and 48 mm (c) respectively.....	92
4.15	Off-axis threading effect from junctioning two equal 50 mm width fields for pitches of 0.3 and 0.45, and JSpac of 45 mm and 48 mm (profiles along the central axis of the right PTVJ).....	93

4.16	(a) On-axis longitudinal dose profiles for few ideal rotations for a unity pitch are represented in different colours (1 <sup>st</sup> in black, 2 <sup>nd</sup> in red, 3 <sup>rd</sup> in green, 4 <sup>th</sup> in blue and 5 <sup>th</sup> in cyan). The total dose is also represented in pink. (b) Similar but real profiles are schematically represented. The thread effect can be seen when single-rotation profiles differ from the ideal triangular shape.....	95
4.17	Dose second moments about $D_P$ as a function of the JSpac for on-axis PTVJ from junctioning equal fields of 50 mm and 25 mm and different fields of 25 mm and 50 mm.....	97
5.1	Transversal (a) and sagittal (b) views of the patient's TomoImage (blue) and the planning image (grey).....	106
5.2	Register tab of the TomoTherapy System.....	107
5.3	Scheme representing a plane view of the increasing margin along Y-axis for a simulated cylindrical OAR (Lung) (a). Comparison of the increasing margins for different maximum margin of 5 mm, 10 mm and 15 mm at the INF extreme of the structure (b).....	108
5.4	Axial (a), coronal (b) and sagittal (c) views of the phantom, iPTVs and iPRVs. Maximum margin of 15 mm. The circles in pink represent the lungs, the structures in dark green and yellow are the ribs and in the centre in blue is the spine. The linearly increasing margin of the iPTVs and iPRVs can be seen on the coronal and sagittal views.....	110
5.5	The increasing margins representing the iPRV for a lung for three cases: no-junction (a), one-junction (b) and two-junctions (c). The figures represent the case of a maximum margin of 15 mm.....	111
5.6	Comparison of the iPTV and iPRV's DVHs between no-junction, one-junction and two-junctions for maximum margin of 10 mm and field width of 50 mm.....	115
5.7	Comparison of the TCP curves as a function of the maximum margin for no-junction, one-junction and two-junction cases. The field width was 50 mm.....	117

5.8	Comparison of the NTCP curves as a function of the maximum margin for no- junction, one-junction and two-junction cases. The field width was 50 mm.....	117
5.9	Probability of uncomplicated cure estimates for no-junction, one- junction and two-junction cases and different maximum margins. The field width was 50 mm.....	120
5.10	TCP vs. NTCP estimates for no-junction, one-junction and two- junction cases and different maximum margins. The field width was 50 mm. The figure has been divided into four quadrants by two lines at NTCP=5% and TCP= 80%. The second quadrant shows the region for a successful treatment.....	123

# Glossary

$\gamma_{50}$ :	Slope at 50% of TCP in Poisson model
$\chi^2(n_{df})$ :	Chi-Square distribution for $n_{df}$ degree of freedom
CC:	Cranial-Caudal
CI:	Confidence interval
CR:	Confidence region
CT:	Computed tomography
CTV:	Clinical target volume
$D_{50}$ :	Dose at 50% of TCP in Poisson model
$D_{P/50}$ :	$D_P$ to the GTV that would lead to a normal organ complication of 50% from the TMI plan using HT
$D_P$ :	Prescribed dose
DVH:	Dose volume histograms

EMP:	Extramedullary plasmacytomas
EUD:	Equivalent uniform dose
GTV:	Gross tumour volume
HT:	Helical TomoTherapy
IG-IMRT:	Image-guided intensity modulated radiotherapy
INF:	Inferior
iPRV:	Increasing planning organ at risk volume
iPTV:	Increasing planning treatment volume
Jspac:	Junction spacing or inter-PTV spacing
LC:	Local control
LKB:	Kutcher-Burman reduction algorithm
lnL:	Log-likelihood function
MC:	Monte Carlo
ML:	Maximum likelihood
MLE:	Maximum likelihood estimators
MM:	Multiple myeloma
MVCT:	Megavoltage CT scan
NTCP:	Normal tissue complication probability
OAR:	Organs at risk
pdf:	Probability distribution function
PTV:	Planning target volume
PTVJ:	New cylindrical PTV defined to contain the volumes of the junctions between the initial PTVs

PRV:	Planning organ at risk volumes
RT:	Radiation therapy
S(D):	Survival probability for dose D
SD:	Standard deviation
SM:	Second moment about $D_p$
SPB:	Solitary plasmacytomas of the bones
SPB+EMP:	Both types of plasmacytomas without distinction
SUP:	Superior
TBI:	Total body irradiation
TCP:	Tumour control probability
$TD_{50}$ :	Tolerance dose to the whole organ that would yield a complication probability of 50%,
TMI:	Total marrow irradiation
TPS:	TomoTherapy Planning Station
[LL, UL]:	Lower and upper limits

# Chapter 1

## Introduction

This study provides scientific background for a *phase III* dose escalation clinical trial for the treatment of multiple myeloma, using image-guided intensity modulated radiotherapy (IG-IMRT) to deliver high dose to the entire volume of bone marrow with Helical TomoTherapy (HT).

### 1.1 Multiple myeloma

Multiple myeloma (MM) is a disseminated plasma cell neoplasm that results from malignant transformation of a single plasma cell and a subsequent clonal expansion and proliferation of tumour cells in the bone marrow. Plasma cells are made by white blood cells and produce antibodies. Cancer cells then crowd out

normal plasma cells causing anemia, hypercalcemia, bone fractures, susceptibility to infections and renal failure. MM can be identified by the presence of a monoclonal immunoglobulin in the serum and urine, multiple discrete areas of bone rarefaction or osteoporosis, and morphologically abnormal plasma cells.<sup>1, 2</sup> The median overall survival of MM patients is about 2½ years. Although in some cases the survival could be extended, in virtually all patients the disease progression is fatal.

The standard treatment for MM is high dose chemotherapy followed by hematopoietic stem cell transplantation. Standard conditioning regimens of 12 Gy (in six fractions) total body irradiation (TBI) in combination with high dose chemotherapy have also been used prior to bone marrow transplant. The principal rationale for TBI is not only to suppress the immune system, but also radiation sterilization of distributed malignant cells. Because TBI is currently given with high dose of chemotherapy, it is difficult to associate specific toxicities strictly to TBI.

## **1.2 Radiation in multiple myeloma**

Radiotherapy has played an important role in the treatment of plasma cell disorders. Local radiotherapy has successfully been used for decades as an

effective treatment of symptomatic localized bone and soft tissue lesions in MM and solitary plasmacytomas providing high rates of local control.<sup>3-5</sup>

Solitary plasmacytomas are rare entities, which are histologically the same as MM, but limited to just one site of the bones or soft tissues without bone marrow involvement. Long term control of localized lesions and solitary plasmacytomas using local radiation therapy in the dose range of or over 30 Gy indicates high radiosensitivity of plasma cell neoplasm and suggests radiation therapy as a potentially therapeutic modality.

On the other hand, the TBI technique has been used for the treatment of hematological malignancies as part of the bone marrow and stem cell transplantation protocols as mentioned above. There has been evidence that dose escalation beyond 12 Gy could improve outcomes and reduce relapses. However, the increased toxicity to critical organs associated with higher doses of radiation has restricted further dose escalation. Lungs and kidneys are considered the most critical structures; and if radiation doses to these structures can be limited, then dose escalation is possible up to at least 20 Gy.<sup>6</sup>

In summary, the main difficulty of using radiation therapy for MM is treating the large volume of bone marrow involved without excessive normal tissue toxicity. Helical TomoTherapy (HT) is an attractive option for TMI since it allows delivery of highly conformal dose distributions. Thus, high doses can be delivered to the

entire bone marrow while achieving lower normal tissue toxicities compared to standard radiotherapy.<sup>7-11</sup>

### **1.3 Helical TomoTherapy**

Helical Tomotherapy is a relatively new modality for delivering image guided intensity modulated radiation therapy. The system in use since 2005 at The Ottawa Hospital Cancer Centre (TOHCC) is the TomoTherapy Hi-Art System (TomoTherapy Inc, Madison, Wisconsin). HT has a design similar to a modern CT scanner, except it uses a 6 MV linear accelerator producing a megavoltage photon beam in place of the X-Ray tube. The linac is mounted on a ring gantry and continuously rotates, with the central axis of the 6 MV beam intersecting the axis of rotation of the gantry (Y-axis), while the patient treatment couch moves with a constant velocity through the gantry bore and parallel to gantry axis of rotation, providing a helical radiation delivery pattern.<sup>12-14</sup> Figure 1.1 shows the TomoTherapy System.

The unfiltered 6 MV radiation beam is collimated to produce a rotating fan-beam with the long axis perpendicular to the axis of rotation. The fan beam width at isocentre (85 cm) has 3 preset values of 10, 25 and 50 mm. The beam is further collimated by a binary multileaf collimator of 64 leaves allowing a maximum field size of 40 cm in the transverse direction. Each leaf has a projected width of 6.25

mm at isocenter. A scheme of the conventional axes direction, the fan-beam and the field width definition are shown in Figure 1.2.

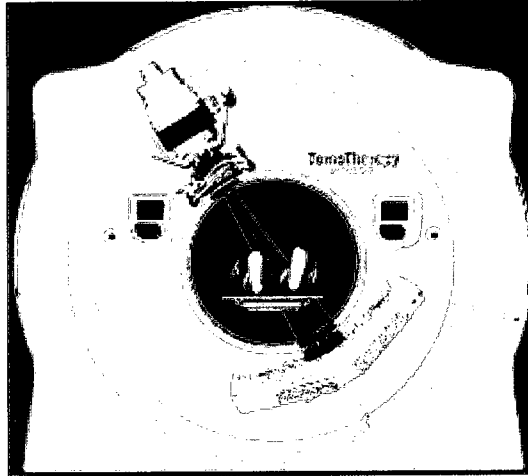


**Figure 1.1** TomoTherapy system. *Figure courtesy of TomoTherapy Inc.*

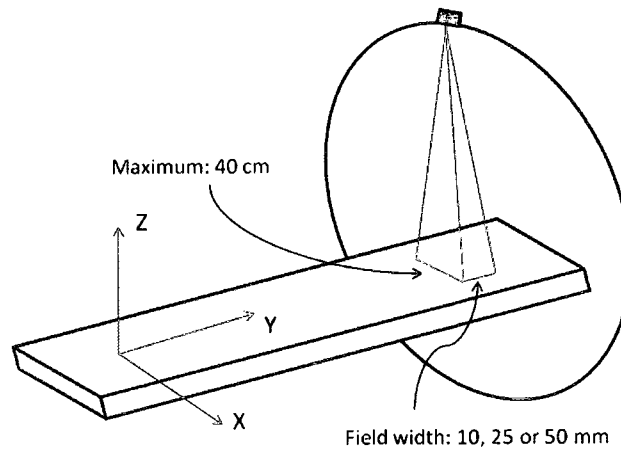


**Figure 1.2** Conventional axes direction, the fan-beam and field width definition. Notice that the field width is defined along the longitudinal direction (along Y axis)

By controlling the time that each leaf is open, the intensity of each segment of the fan-beam is modulated. Thus, the resulting intensity profile is defined by the cone-shaped profile from the fan beam and the open-time of the multileaf collimator leaves.

Another important delivery parameter is the pitch, defined as the ratio of the distance that the couch moves per gantry rotation divided by the field width.<sup>7</sup> This IMRT technique allows delivery of highly conformal dose distributions. Opposite to the beam source there is a system of radiation detectors that allows the use of the same linac as a megavoltage CT scanner by reducing the beam energy. Incorporating an imaging session into the treatment improves the reproducibility of the patient alignment by imaging the patient before delivery of each daily radiation fraction (known as image guided radiation therapy or IGRT).

The treatment procedures include a few basic steps: treatment planning; treatment plan optimization; setting up the patient in the treatment position; imaging the patient adjusting the patient position based on the imaging; and treatment delivery.

The treatment planning process is used to prescribe the treatment and starts with a 3D kV CT scan of the patient. These images are used by the radiation oncologist to delineate the planning target volume (PTV) and organs at risk (OAR) in each slice. To obtain the PTV, the radiation oncologist determines the gross tumour volume (GTV), generally defined as the visible target, and expands

it to include a reasonable expectation of a true target resulting from subclinical disease. This yields the clinical target volume (CTV). The CTV is again expanded to account for organ movement and setup errors yielding the PTV. Similarly, OARs are expanded to obtain the planning organ at risk volumes (PRV).

The treatment dose is prescribed to the PTV. The tumour and OAR dose constraints are also specified. The parameters necessary in the optimization procedure include: importance, maximum and minimum doses, DVH dose and penalties. Field width, pitch and modulation factor are also selected.

The planning system calculates the dose through an optimization process using a superposition algorithm. For this purpose, the beam is divided into 'beamlets'. The beamlets are determined from the 51 discrete projections of each full gantry rotation (spaced about  $7^\circ$  apart), the 64 segments corresponding to the leaves of the multileaf collimator multiplied by the number of rotations. The beamlets that do not pass through the PTVs are eliminated to reduce calculations. Then, the data from the CT scan of the patient are divided into a 3D matrix. The optimization routine calculates for each voxel the set of beam weightings to achieve the desired dose. The optimization parameters can be modified at any time until the required dose distributions are obtained and the optimization resumed. When the optimization is finished the fractionation schedule is selected.

Before each treatment fraction delivery, the patient undergoes a megavoltage CT scan (MVCT) on the TomoTherapy unit and the treatment position is verified and adjusted.

#### **1.4 Objectives**

The aim of this study is to provide tools for comparing and predicting the effectiveness of different approaches to TMI using HT.

The primary goal was to perform a radiobiological evaluation of different treatment cohorts in a dose escalation study in TMI. Because of the lack of radiation dose response for multiple myeloma in the literature, an extensive review of plasma cell neoplasm clinical data was performed and radiation dose response functions were defined by fitting the clinical data to previously published models of radiobiological response.

A secondary goal was to assess the implications of using different longitudinal field lengths with the final objective of reducing planning and delivery time without causing unacceptable increases in normal tissue toxicities while achieving similar tumour control. This work expects to describe the dosimetric challenges that arise when junctioning longitudinally adjacent PTVs with HT, which is necessary in clinical situations like TMI, and examine clinically viable solutions.

The last goal is to perform an analysis of the radiobiological benefits of spatial image guidance frequency in TMI.

# Chapter 2

## Radiation dose response of plasma cell neoplasms

### 2.1 Introduction

Clinical dose response data of human tumours are limited or restricted to a dose range determined by the level of toxicity to the normal tissues. This is the case for the most common disseminated plasma cell neoplasm, multiple myeloma (MM), where the maximum dose deliverable to the entire bony skeleton using a standard total body irradiation (TBI) technique is limited to about 12 Gy. Recently, new clinical trials have been developed for a more targeted treatment in MM patients using helical tomotherapy.<sup>8, 9, 11</sup> These studies included dose escalation trials for dose levels up to 18 Gy. However, there are not enough data

and/or complete or comprehensive data have not been published. In addition, many published clinical studies have insufficient periods of patient follow-up. This means that relatively short-term rates of local control must be used as the end-point, as opposed to a preferred long-term end-point such as 5 year disease-free survival.

For other less common plasma cell myelomas, like solitary plasmacytomas of the bones (SPB) or extramedullary plasmacytomas (EMP), much higher treatment doses have been used since they are more localized and easier to treat than MM, but they account for just 5-10% of all plasma cell neoplasms. These neoplasms are radiosensitive and high rates of local control (LC) can be achieved.<sup>3-5, 15</sup> However, there are no conclusive data on the optimal dose for plasmacytomas or a well-defined dose response relationship.

EMP most frequently originates in head and neck sites, in the nasopharynx and upper respiratory track, but also presents in the gastro-intestinal track and lymph nodes. EMP has a tendency to spread locally (high incidence of metastatic spread) to soft tissues and bones without diffuse bone marrow involvement. On the other hand, SPB occurs in the axial skeleton and less frequently in the bones of the extremities. Soft tissues are rarely involved and progression to MM occurs in the majority of SPB patients, a fact that leads some authors to believe that SPB could be an early stage of myelomatosis.<sup>1, 4, 16</sup>

Whether or not EMP, SPB and MM are part of the same disease spectrum is still controversial. The relationship between them is not well understood. They all are histologically the same and result from uncontrolled plasma cell proliferation; however, the different natural history and progression leave this question unclear.

Because of the lack of radiation dose response specifically for MM (or the data to be estimated), plasmacytoma clinical data were examined. Since all plasma cell tumours are histologically the same, and SPB can be considered an early presentation of MM<sup>1, 16-18</sup>, the analysis conducted on plasmacytoma data is a reasonable approach to achieve a preliminary quantification of MM radiation dose response.

Knowledge of the radiation dose response is crucial for radiobiological modeling, which can have an important role in assessing new treatment techniques and comparing different treatment approaches. In this study, the available published clinical dose response data for EMP and SPB were reviewed. Using these data, the expected dose response for plasma cell neoplasms based on estimates of the tumour control probability (TCP) was computed. Any possible difference between EMP and SPB dose response was also evaluated.

## **2.2 Study selection criteria**

Reports of from 27 studies on plasmacytomas were reviewed and analyzed, including single and multi-institutional trials. The clinical data fell into three different groups: studies for patients with SPB; studies for patients with EMP; and studies without a distinction between EMP and SPB. This last group is referred to as SPB+EMP. We also verified that in every case the data sourced from different institutions to avoid their over-representation.

In general, there are many factors that affect the patient cure, tumour control or survival rate. The history of the tumour, type of treatment, tumour staging and individual patient response are some of the factors which influence the treatment outcome. In order to isolate data as much as possible to radiation dose response and eliminate some of the influences mentioned above, the rate of LC was used as an end point in our searching criteria.

The main assumption is that a sufficient radiation dose will locally control any tumour. Ideally, if we were able to target all tumour cells with adequate dose, it would be possible to control the tumour.

In many clinical reports, the data are reported in dose ranges and only the median dose is stated. In those cases, only data within a range  $\leq 10$  Gy were analyzed. In a few cases, more detailed information was given and if required, data was regrouped into 10 Gy intervals. This was the case when the data were

published by individual patient. If many patients were treated with a specific dose, this dose value was kept and the LC rate determined from the reported LC outcome for each patient. Conversely, if the treatment dose varied among the patients the data were regrouped into 10 Gy intervals and the median and LC were then calculated. The dose range selection criteria are shown as an example for the data reported by Strojan *et al*<sup>19</sup> in Table 2.1. In the second last column, the data from three patients were grouped instead of following the criteria since they have very similar dose values. Having a larger number of patients will decrease the uncertainty and will not change the results since the three patients achieved LC.

**Table 2.1** Example of the dose range selection criteria for Strojan *et al.* data.

Dose Range (Gy) Selection Criteria	Median Dose (Gy)	LC	No. of Patients
D < 30	14.4	0	1
30 ≤ D < 40	40	0.88	16
40 ≤ D < 50	48	1	6
56, 60, 61.5	60	1	3
70	70	1	1

Nevertheless, most of the studies reported the data in dose ranges already; therefore, the doses used for the analysis are in general the median doses of dose intervals of at most 10 Gy. Restricting the analysis to dose ranges ≤10 Gy

represents a fair approximation considering the limitations of the published data. First, the majority of the data were reported with dose ranges  $\geq 10$  Gy, unless when reported by patient, limiting the use of smaller dose range. Using dose ranges  $> 10$  Gy would increase the uncertainty in a dose response analysis.

There were some limitations that unfortunately could not be included in the analysis. Variables such as tumour size, fraction size and follow-up time can have an important effect on LC rate. Most of the studies did not report tumour size. There were two exceptions: Tsang *et al.*<sup>5</sup> and Frassica *et al.*<sup>20</sup>, but the work of Frassica *et al.* could not be included because the data did not meet our 10 Gy dose range criteria. Thus, there was not sufficient information to perform an analysis on the tumour size influence.

Similarly, the fraction size was also ignored. Most patients were treated with a common regimen of 2 Gy/fx, but explicit fraction sizes were not well specified in all reference data sets. An assumption was made that all patients had the same fractionation, which can introduce uncertainty in the analysis. Follow-up time was also not accounted for in this analysis since in many studies it was not published or varied from one study to another one. In the studies where the data were published by patient, the follow-up time for patients achieving LC ranged from 2 to more than 15 years. In very few cases the LC was reported for less than 2 years but only when the patient died from other causes.

Patients with SPB and EMP are mainly treated with radiation therapy (RT). However, patients with local recurrence or multiple myeloma development were salvaged by high dose chemotherapy and/or extra radiotherapy. In the cases of patients with local relapse after the initial treatment (and if the information was fully published), the dose of the initial treatment and no LC was assumed, even though the LC was achieved after a second treatment (either RT or chemo). The initial treatment in most of the cases was RT alone. However, in some exceptional cases chemotherapy and surgery were also used. For example, in Susnerwala *et al.*<sup>21</sup> two patients out of 25 received an initial treatment of combined RT and chemotherapy because they had clinical involvement of cervical lymph nodes. In addition, there were papers where the clinical information was less specific (for example Knobel *et al.*<sup>15</sup>) where they reported using RT and chemotherapy for the treatment of SPB (without evidence of MM) where 32 patients had a combination of RT and chemotherapy and 169 patients had RT alone. Including patients receiving chemotherapy may affect the dose response analysis but given the limited published data I have chosen to include these patients.

The selected clinical data on SPB, EMP and SPB+EMP were used to perform a dose response analysis. Even though SPB, EMP and MM are histologically the same,<sup>1</sup> EMP differs from SPB in its pattern of spread and the site of preference of the primary tumours. In order to not bias our analysis all, the data groups were separately fitted. For the SPB patients, our data have been fitted two different

ways: one with and one without the inclusion of a 12 Gy zero local control data point (corresponding to TBI treatment). This was done for two reasons: First, to see how this data point affects the dose response function; and second, there is very good evidence that the natural history of SPB is to eventually express as MM leading to the belief that SPB is an early presentation of myelomatosis.<sup>1, 16-18</sup>

### 2.3 Dose response model

In this study a two-parameter Poisson model was used, which has often been applied in the analysis of tumour response data. Using more complicated models in the absence of very specific biological descriptions results in parameter correlation and difficulty in the interpretation of the results.<sup>22</sup>

TCP models assume that all tumour clonogens have to be killed to achieve tumour control. Poisson statistics predicts this probability as:

$$TCP = \exp(-N S(D)) \quad (2.1)$$

where  $N$  is the initial number of clonogens and  $S(D)$  is the survival probability for dose  $D$ . Cell survival is then assumed to be described by single hit mechanism, which is also assumed to be described by Poisson statistics:

$$S(D) = \exp(-\alpha D) \quad (2.2)$$

TCP models based on Poisson statistics<sup>22</sup> can be written in terms of  $D_{50}$  and  $\gamma_{50}$ , parameters that describe the dose and the slope at the point of 50% probability of control. The equation is shown below where  $D$  represents the dose:

$$TCP = \left(\frac{1}{2}\right)^{\exp[2\gamma_{50}(1-D/D_{50})/\ln 2]} \quad (2.3)$$

The meaning of parameters  $D_{50}$  and  $\gamma_{50}$  in a TCP Poisson model is illustrated in Figure 2.1. The  $D_{50}$  is the dose that will result in 50% of TCP. That is if 100 tumours or patients had been treated,  $D_{50}$  is the dose that would control half (50) of these tumours or patients. (The meaning of “control” depends on the endpoint of the study – in the studies selected, the endpoint was local control, meaning a disappearance of clinical or radiographic evidence of the tumour in the irradiated volume.) In Figure 2.1 the  $D_{50}$  was represented by the arrow in dashed line pointing at 22 Gy (arbitrary value). The  $\gamma_{50}$  represents the expected change in tumour control (TCP) due to 1% variation in dose about  $D_{50}$ . In Figure 2.1 the  $\gamma_{50}$  was represented by the thicker straight solid line on the TCP curve. This line symbolizes the slope of the TCP curve at the point ( $D_{50}$ ,  $TCP=50\%$ ). For illustrative purposes, an arbitrary value of 1.1%/‰ of  $\gamma_{50}$  was used in Figure 2.1.

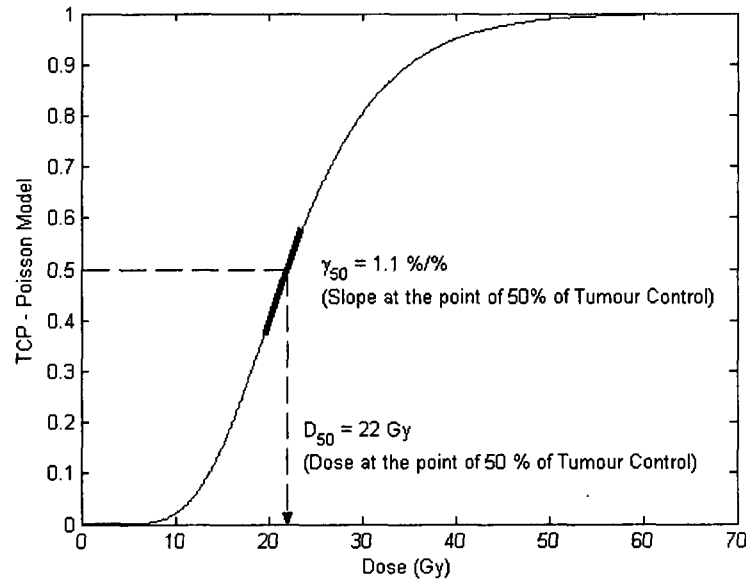


**Figure 2.1** Graphical illustration of the meaning of parameters  $D_{50}$  and  $\gamma_{50}$  in a TCP Poisson model.

## 2.4 Maximum likelihood method

Clinical or experimental data are often accompanied by errors. That is why the resultant outcomes of a dependent variable such as the TCP function vary even though the independent variables, in this case the dose, remain constant. Curve fitting is the procedure used to estimate the trend of the outcomes given by the shape of the model describing the data. The shape of the model is itself defined by the parameters of the model. The fit of clinical or experimental data to an approximating model is generally not unique for a given data set.

In this work, the maximum likelihood method (ML)<sup>23, 24</sup> was used. The method of ML estimates the parameters of the model that maximize the probability of the sample data, as it is shown below.

Assume that there is a random variable  $x$  distributed according to a known probability distribution function (pdf) represented by  $f(x; \theta)$ . However, the values of at least one of the  $m$  parameters  $\theta(\theta_1, \dots, \theta_m)$  are unknown. The ML estimates the values of the parameters given a finite sample data set. Consider  $x_1, \dots, x_n$ , the  $n$  measurements of the random variable  $x$  (the outcome of each individual observation). Assuming the hypothesis  $f(x; \theta)$ , including the value of  $\theta$ , the probability that the first measurement is in the interval  $[x_1, x_1 + dx_1]$  is  $f(x_1; \theta)dx_1$ . Assuming that all measurements are independent, then the probability to have at the same time the first measurement in  $[x_1, x_1 + dx_1]$ , the second one in  $[x_2, x_2 + dx_2]$  and so on, until  $n$  measurements is given by

$$\text{Probability of } x_i \text{ being in } [x_i, x_i + dx_i] \text{ for all } i: \prod_{i=1}^n f(x_i; \theta)dx_i, \quad (2.4)$$

If the hypothesis  $f(x; \theta)$  and the parameters were correct, the probability obtained using Equation 2.4 would be high. On the other hand, parameter values away from the true value would result in a low probability for the measurements. Since  $dx_i$  do not depend on  $\theta$  the same reasoning could be used for a function  $L$  given by

$$L(\theta) = \prod_{i=1}^n f(x_i; \theta) \quad (2.5)$$

$L(\theta)$  function is called likelihood function and it is defined by the joint pdf for all  $x_i$ .  $L$  in the ML method is considered to be a function of parameter  $\theta$ , while  $x_i$  are fixed and obtained from the measurements or individual observations. Therefore, the ML estimates the parameters that maximize the likelihood function  $L$ . These parameters are called maximum likelihood estimators (MLE) and represented by  $\tilde{\theta}(\tilde{\theta}_1, \dots, \tilde{\theta}_m)$ . Assuming  $L$  is a differentiable function of parameters  $\theta(\theta_1, \dots, \theta_m)$  and the maximum is not at the boundary of the parameter range, the MLE are determined by setting the first derivative of  $L$  function with respect to each parameter  $\theta_i$  equal zero. However, the logarithm of  $L$  is first constructed, since it is easier to deal with the derivative of a sum than with a derivative of a product. The function  $\ln L$  is referred to as the log-likelihood function.

$$\ell = \ln L(\theta) = \sum_{i=1}^n \ln f(x_i; \theta) \quad (2.6)$$

$$\ell' = \frac{\partial \ell}{\partial \theta_i} = 0, \quad i = 1, \dots, m \quad (2.7)$$

### 2.4.1 Variance and confidence region of the MLE

In many applications is very difficult to compute the variances analytically. Instead, in this section the Rao-Cramer-Frechet (RCF) inequality was used.<sup>23, 24</sup>

The RCF inequality, also called information inequality, gives a lower bound on the estimators' variance. This lower bound for the case of just one parameter is:

$$V[\tilde{\theta}] \geq \left(1 + \frac{\partial b}{\partial \theta}\right)^2 / E\left[-\frac{\partial^2 \ln L}{\partial \theta^2}\right] \quad (2.8)$$

where  $b$  is the bias and  $L$  is the likelihood function. A complete proof and practical examples could be found in Brandt<sup>23</sup> and Eadie<sup>25</sup>. In the large sample limit (infinite data sample) and for MLE, the RCF inequality becomes an equality (i.e. minimum variance).<sup>24,25</sup> Then, assuming zero bias Equation 2.8 for the case of more than one parameter  $\theta(\theta_1, \dots, \theta_m)$  reduces to:

$$(V^{-1})_{ij} = E\left[-\frac{\partial^2 \ln L}{\partial \theta_i \partial \theta_j}\right] \quad (2.9)$$

Since this property of the estimator  $\tilde{\theta}$  is valid for the case of an infinitely large data sample and in practice we have a finite sample, the analysis below is associated with the "asymptotic" properties of the likelihood function and MLE.

In practice, it is difficult to analytically determine the expectation value of the second derivative of the  $\ln L$  function. Then, the  $V^{-1}$  is estimated by evaluating the second derivative using the measured data and the MLE:

$$(\tilde{V}^{-1})_{ij} = - \left. \frac{\partial^2 \ln L}{\partial \theta_i \partial \theta_j} \right|_{\theta = \tilde{\theta}} \quad (2.10)$$

For a single parameter  $\theta$  this reduces to:

$$\tilde{\sigma}_{\theta}^2 = \left( -1 / \frac{\partial^2 \ln L}{\partial \theta^2} \right)_{\theta = \tilde{\theta}} \quad (2.11)$$

A graphical technique for obtaining the variance of MLE is just an extension of the previously discussed method. Expanding the log-likelihood function  $\ln L$  in a Taylor series about the MLE  $\tilde{\theta}$  (for simplicity the case of only one parameter is considered):

$$\ln L(\theta) = \ln L(\tilde{\theta}) + \left[ \frac{\partial \ln L}{\partial \theta} \right]_{\theta = \tilde{\theta}} (\theta - \tilde{\theta}) + \frac{1}{2!} \left[ \frac{\partial^2 \ln L}{\partial \theta^2} \right]_{\theta = \tilde{\theta}} (\theta - \tilde{\theta})^2 + \dots \quad (2.12)$$

The first term on the right of Equation 2.12 is where the function  $\ln L$  reaches the maximum by definition. The second term is equal zero since the first derivative at a maximum is zero. Then, using Equation 2.11 and ignoring higher order terms Equation 2.12 reduces to:

$$\ln L(\theta) = \ln L_{\max} - \frac{(\theta - \tilde{\theta})^2}{2\tilde{\sigma}_{\tilde{\theta}}^2} \quad (2.13)$$

In the large sample limit, the  $\ln L$  becomes Gaussian<sup>23, 24</sup> and of a parabolic shape and Equation 2.13 reduces to:

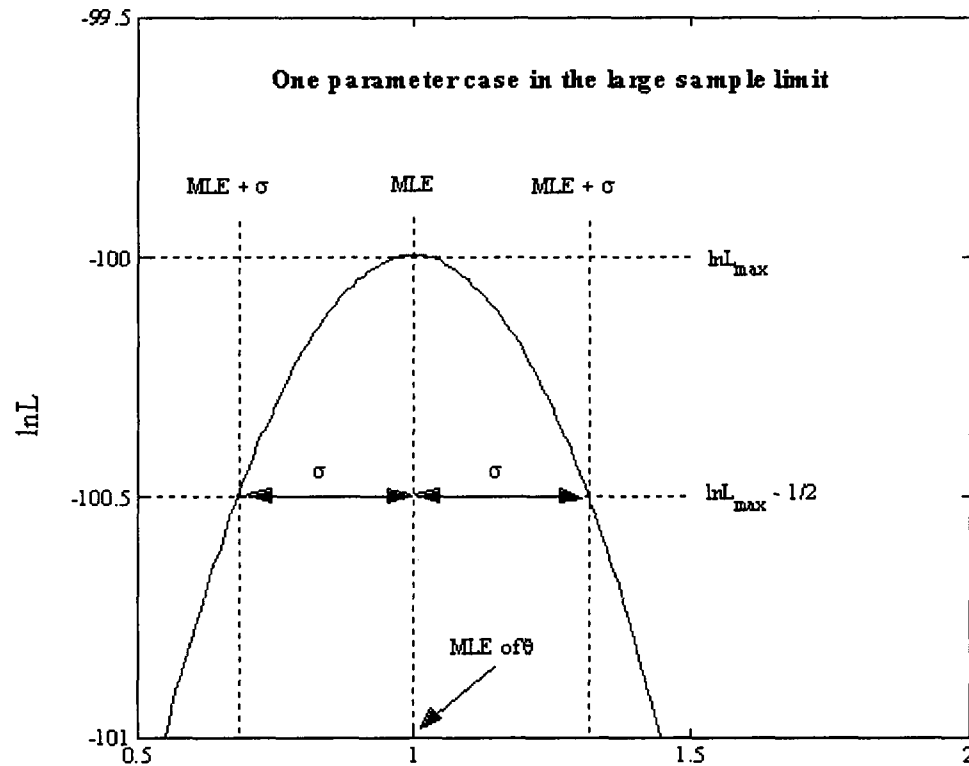
$$\ln L(\theta) = \ln L_{\max} - \frac{1}{2} \quad (2.14)$$

Figure 2.2 illustrates the  $\ln L$  function as a function of  $\theta$  with the MLE and the corresponding standard deviation.

Even for a non-Gaussian estimator, the confidence interval (CI) can be approximately determined using the likelihood function and  $\chi^2$  function. Consider a simple transformation to Equation 2.13:

$$\exp[\ln L(\theta)] = \exp\left[\ln L_{\max} - \frac{(\theta - \tilde{\theta})^2}{2\tilde{\sigma}_{\tilde{\theta}}^2}\right] \quad (2.15)$$

$$L(\theta) = L_{\max} \exp\left(-\frac{(\theta - \tilde{\theta})^2}{2\tilde{\sigma}_{\tilde{\theta}}^2}\right) \quad (2.16)$$



**Figure 2.2** Graphical illustration of  $\ln L$  function as a function of  $\theta$  with the MLE and the corresponding standard deviation.

The likelihood function  $L$  is of the form of a Gaussian function centered about the MLE  $\tilde{\theta}$ . The interval determined by  $\ln L_{\max} - 1/2$  in Figure 2.2 gives the 68.3% central CI and correspond to one standard deviation  $\tilde{\sigma}_{\tilde{\theta}}$  (also called symmetric error). A 68.3% CI means that the true parameter is contained within the interval with a probability of 0.683.

Even if the  $\ln L$  function is not parabolic ( $\ln L$  is not Gaussian), Equation 2.14 could be used as a measure of the statistical error. For small data samples, instead of

approximating the standard deviation  $\sigma_{\tilde{\theta}}$  using the half-width of the interval, the 68.3% central confidence interval can be approximated by giving the asymmetric errors corresponding to the lower and upper limits [LL, UL]. These limits are determined similarly to the description above, by  $\ln L_{\max} - \frac{1}{2}$  as shown in Figure 2.2. However, because the  $\ln L$  is less parabolic (asymmetric) the intervals will not be symmetric.

The general case for  $m$  parameter  $\theta(\theta_1, \dots, \theta_m)$  is usual to construct a confidence region (CR) in the parameter space such as the true parameter is contained within the region with certain probability. Similar to Equation 2.13 in a multidimensional analysis we have:

$$\ln L = \ln L_{\max} - \frac{Q_\gamma}{2} \quad (2.17)$$

where  $Q_\gamma$  is the quantile of order  $1-\gamma$  of the  $\chi^2(n_{df})$  distribution for  $n_{df}$  degrees of freedom. The value of  $Q_\gamma$  is chosen to correspond to a given probability,

$$\int_0^{q_\gamma} f(z; n_{df}) dz = 1 - \gamma \quad (2.18)$$

The region  $Q(\theta, \tilde{\theta}) \leq Q_\gamma$  is called the confidence region with a confidence level of  $1-\gamma$ . For the two-dimensional case (two parameters) the confidence region is constructed by finding the values at which  $\ln L$  function decreases by  $Q_\gamma/2$ . The  $\ln L$  function on the parameter space is described by a figure that approximates a

paraboloid and the CR resembles an ellipse (at least approximately). The Equation 2.17 as for the single-parameter case can still be used even if the InL function is not Gaussian; however, the CR is only approximate.

#### 2.4.2 Maximum likelihood estimators for TCP

The ML method<sup>23, 24</sup> was applied to estimate the values of the parameters  $D_{50}$  and  $\gamma_{50}$  for the TCP model. The method of ML estimates the parameters (MLE) that maximize the probability of the sample data.

In practice, the negative log-likelihood function (-InL) was minimized and a binomial distribution function<sup>23, 24</sup> was chosen as the hypothesis for the distribution of the LC-variable:

$$\text{Min} \left\{ -\ln L = -\sum_{i=1}^N \ln f(D_i, k_i, n_i; D_{50}, \gamma_{50}) \right\} \quad (2.19)$$

where InL is the log-likelihood function to be maximized,  $N$  is the number of data points,  $n_i$  is the number of patients treated for each dose  $D_i$  and  $k_i$  is the number of patients with LC outcome. The function  $f(D_i, k_i, n_i; D_{50}, \gamma_{50})$  is a binomial distribution function of the form:

$$f(D_i, k_i, n_i, p_i) = \left( \frac{n_i!}{k_i!(n_i - k_i)!} \right) p_i^{k_i} (1 - p_i)^{n_i - k_i} \quad (2.20)$$

$$p_i = TCP_i(D_i; D_{50}, \gamma_{50}) \quad (2.21)$$

The assumption above is justified since for each dose range we considered a series of independent observations or trials  $n_i^{Obs}$  (the observed number of patients treated within the dose range), each having two possible outcomes, either local control (success) or no local control (failure) with a certain and constant probability  $p_i$  of local control for each dose  $D_i$ . Using a Poisson TCP model, this probability  $p_i$  as a function of dose is estimated knowing the observed number of success  $k_i^{Obs}$  (patients with LC) and the observed number of patients  $n_i^{Obs}$  that have been treated for each dose range  $D_i$ . Therefore, for each independent data point  $p_i^{Obs}$  represents the observed probability defined by  $k_i^{Obs}/n_i^{Obs}$ . This quantity represents itself a MLE of the true probability for each independent data point (it is important not to confuse with  $p_i$  defined in Equation 2.21, which result from the fit of all data points to the TCP model). The ML method does not weight the data points as  $\chi^2$  does. However, when the frequency of an event is measured such as  $k_i^{Obs}/n_i^{Obs}$ , the variance of the frequency  $\sigma^2(k_i^{Obs}/n_i^{Obs})$  is proportional to  $1/n_i^{Obs}$  and this property is known as the law of larger numbers. This means that the error of each of the data points is inversely proportional to the number of patients.

The observed data points  $(D_i, p_i^{Obs})$  were found from EMP, SPB and EMP+SPB clinical data. The observed data were fitted. The estimates of  $p_i = TCP_i$  as

defined in Equation 2.21 were obtained by estimating  $D_{50}$  and  $\gamma_{50}$ . For simplicity, the superscript "Obs" has been removed from equations 2.19, 2.20 and 2.21.

Hence, combining Equations 2.19, 2.20 and 2.21 the values of  $D_{50}$  and  $\gamma_{50}$  were found by minimizing the following log-likelihood function:

$$-\ln L = -\sum_{i=1}^N [k_i \ln(TCP_i) + (n_i - k_i) \ln(1 - TCP_i)] \quad (2.22)$$

where  $k_i^{Obs}$  and  $n_i^{Obs}$  characterize the observational or clinical data while  $TCP_i$  represents the model to be found.

The Hessian matrix of the log-likelihood function (H), evaluated with the clinical data and ML estimators, was calculated to estimate the covariance matrix (V), from which the variance ( $\sigma^2$ ) and then the standard deviation (SD) of the parameters were determined.

The Hessian matrix of the log-likelihood function is the square matrix of second order partial derivatives with respect to parameters  $D_{50}$  and  $\gamma_{50}$ . Using Equation 2.10 the inverse covariance matrix is expressed for the case of two parameters as:

$$V^{-1} = -H = - \begin{pmatrix} \frac{\partial^2 \ln L}{\partial D_{50}^2} & \frac{\partial^2 \ln L}{\partial D_{50} \partial \gamma_{50}} \\ \frac{\partial^2 \ln L}{\partial D_{50} \partial \gamma_{50}} & \frac{\partial^2 \ln L}{\partial \gamma_{50}^2} \end{pmatrix}_{\substack{D_{50} = \bar{D}_{50} \\ \gamma_{50} = \bar{\gamma}_{50}}} \quad (2.23)$$

$$V(\text{Covariance Matrix}) = (-H)^{-1} = \begin{pmatrix} \sigma_{D_{50}}^2 & \text{cov}(D_{50}, \gamma_{50}) \\ \text{cov}(D_{50}, \gamma_{50}) & \sigma_{\gamma_{50}}^2 \end{pmatrix} \quad (2.24)$$

The SD can be used as a measure of the statistical error, however, since the distribution of the parameters is not known, the usual interpretation of confidence interval (CI) for Gaussian distributed variables cannot be applied. Therefore, the approximate likelihood confidence regions (CR) for asymptotic conditions (in the large sample limit) were calculated with a confidence level  $1-\gamma$  as defined in Equation 2.17.

### 2.4.3 Uncertainty analysis based on Monte Carlo

The Monte Carlo method (MC) is a technique which provides approximate solutions to a variety of mathematical and physical problems by performing statistical sampling experiments on a computer.

In modeling, Monte Carlo analysis has been widely used to provide accurate and reliable statistics for the parameters of the model fitting experimental data. A

number of MC generated values are used to evaluate a parameter estimator, as is done with real data.

The statistical accuracy of properly constructed estimators increases as the number  $n$  in the data sample increases. One can show that under certain fairly general conditions the variance is proportional to  $1/n$ .<sup>23, 24</sup> Thus, instead of repeating complicated experiments many times, which could be very time consuming, expensive or sometimes impossible, they are simulated to reduce the parameter uncertainty.

Consider  $n$  independent random variables  $x_1, \dots, x_n$  which are distributed according a known pdf  $f_1(x_1), \dots, f_n(x_n)$ , and one wants to determine the pdf  $g(a)$  of some function  $a(x_1, \dots, x_n)$ . Using MC method a value of  $x_i$  is generated according the corresponding  $f_i(x_i)$ . Then, the value of  $a(x_1, \dots, x_n)$  is calculated and recorded in a histogram. This procedure is repeated many times until the pdf  $g(a)$  is reconstructed with the desired statistical precision. An important condition is that the pdf  $f_1(x_1), \dots, f_n(x_n)$  of the random variables  $x_1, \dots, x_n$  must be known.

In this study, the pdf of the parameters  $D_{50}$  and  $\gamma_{50}$  are determined assuming one knows the distribution of the experimental or clinical data.

The nature of the selected clinical data is binomial with only two possible outcomes, LC or not LC of the patient tumour, as previously mentioned. The pdf

of such a variable is described by Equation 2.20. The ML method chooses the model parameters that make our data more likely than other values based on the clinical data ( $k_i^{Obs}$  and  $n_i^{Obs}$ ).

Using MC technique, the dependent LC-variable was generated from a random binomial distribution with probability  $p_i$  obtained from the ML fit, and the number of patients  $n_i^{Obs}$  obtained from the original clinical data. Therefore, the condition that the pdf of the variable representing the clinical data  $f_i(x_i)$  must be known, includes knowing the distribution (binomial) and that the TCP model properly describes the data. The latter is necessary since in Equations 2.20 and 2.21 the true probability is estimated by TCP Poisson model.

In addition, the dose which is the model independent variable is in fact the median dose of at most 10 Gy dose intervals. The dose was then randomly generated from a uniform distribution centred at the median dose, and varies within a 10 Gy dose range in correspondence with the original data.

Therefore, under the assumption discussed above, 10000 new MC data sets were generated, including both, dose and LC variables. These MC data sets were fitted and the distributions of the parameters were found. The 95% confidence intervals of the parameters were delimited with equal probability of 0.025 in the tail. These intervals are referred as  $CI_{MC}$ . A statistical test based on the MC parameter probability distributions to discriminate between different kinds of tumours was also performed.

## 2.5 Results

### 2.5.1 Compiled clinical data

A total of 12 publications were finally selected for the analysis. The LC of the disease was used as the end point and it represents the ratio of the number of patients that had local control to the total number of patients treated within the same dose range. Clinical data reported for a wider dose range (>10 Gy) was not included in the analysis. The clinical data, *e.g.* the median dose, LC probability, and the dose range of the data used in this study are shown in Table 2.2. With the exception of two studies,<sup>3, 15</sup> no errors or CI were reported with the data. Estimated CI for binomial proportions when sample size is small were calculated using the modified Wald method and the lower and upper limits ([LL, UL]) are provided in Table 2.2 as well as the references for the original data. For TBI a conventional treatment of 12 Gy<sup>9, 10, 26</sup> and no local control was assumed.

Any specific effects of chemotherapy and fractionation were ignored, although in the majority of the studies there was a common regimen. Radiation therapy was used as the sole treatment in more than 70 %. The other patients had surgery or chemotherapy either as adjuvant therapy or after local recurrence or MM development. Including patients who received chemotherapy overestimates the dose response. However, the information provided in the published reports of clinical studies was not specific enough to allow discrimination of patients treated with only radiation therapy. Given the limited published data we decided to

include these patients since it was clear that the majority of the patients were treated with radiation therapy alone.

**Table 2.2** Clinical data for solitary plasmacytomas used in this study. Median dose, LC rate, number of patients treated, 95% CI for binomial proportion, the dose range and the references to the original paper.

Median Dose (Gy)	LC	No. of Patients	95% Wald CI [LL, UL]	Dose Range (Gy)	Type	Study
14.4	0	1	[0, 0.78]	14.4	EMP	Strojan 2002 <sup>19</sup>
35	0.78	9	[0.44, 0.95]	25-35	EMP	Susnerwala 1997 <sup>21</sup>
40	0.88	16	[0.63, 0.98]	30-40	EMP	Strojan 2002 <sup>19</sup>
40	0.85	7	[0.47, 0.99]	35-45	EMP	Jyothirmayi 1997 <sup>27</sup>
44	1	11	[0.77, 1.00]	40-46	EMP	Chao 2005 <sup>28</sup>
45	0.53	15	[0.30, 0.75]	36-45	EMP	Susnerwala 1997 <sup>21</sup>
48	1	6	[0.64, 1.00]	40-50	EMP	Strojan 2002 <sup>19</sup>
50	1	1	[0.22, 1.00]	50-50.4	EMP	Chao 2005 <sup>28</sup>
50	1	1	[0.60, 1.00]	50	EMP	Susnerwala 1997 <sup>21</sup>
60	1	3	[0.47, 1.00]	56-65	EMP	Strojan 2002 <sup>19</sup>
70	1	1	[0.22, 1.00]	70	EMP	Strojan 2002 <sup>19</sup>
25	0.92	25	[0.74, 0.99]	20-30	SPB	Knobel 2006 <sup>15</sup>
30	1	3	[0.47, 1.00]	30	SPB	Dimopolous 1992 <sup>29</sup>
35	0.91	55	[0.80, 0.96]	30-40	SPB	Knobel 2006 <sup>15</sup>
36	0.83	6	[0.42, 0.99]	33-38	SPB	Chang 1994 <sup>30</sup>
45	0.88	65	[0.77, 0.94]	40-50	SPB	Knobel 2006 <sup>15</sup>
45	1	53	[0.94, 1.00]	40-50	SPB	Aviles 1996 <sup>31</sup>
46	1	3	[0.47, 1.00]	45-48	SPB	Chang 1994 <sup>30</sup>
50	1	18	[0.85, 1.00]	46-55	SPB	Dimopolous 1992 <sup>29</sup>

52	1	6	[0.64, 1.00]	50-55	SPB	Chang 1994 <sup>30</sup>
22.5	0.75	4	[0.29, 0.97]	20-30	SPB+EMP	Mayr 1990 <sup>32</sup>
25	0.96	27	[0.80, 1.00]	20-30	SPB+EMP	Ozsahin 2006 <sup>3</sup>
27.5	0.86	7	[0.47, 0.99]	25-30	SPB+EMP	Tsang 2001 <sup>5</sup>
34.5	0.8	5	[0.36, 0.98]	30-40	SPB+EMP	Shih 1995 <sup>4</sup>
35	1	3	[0.47, 1.00]	30-40	SPB+EMP	Mayr 1990 <sup>32</sup>
35	0.85	27	[0.67, 0.95]	35	SPB+EMP	Tsang 2001 <sup>5</sup>
35	0.9	70	[0.80, 0.95]	30-40	SPB+EMP	Ozsahin 2006 <sup>3</sup>
41	0.78	9	[0.44, 0.95]	40-50	SPB+EMP	Mayr 1990 <sup>32</sup>
42	1	4	[0.54, 1.00]	40-50	SPB+EMP	Shih 1995 <sup>4</sup>
45	0.73	76	[0.61, 0.81]	40-50	SPB+EMP	Ozsahin 2006 <sup>3</sup>
45	0.83	12	[0.54, 0.96]	40-50	SPB+EMP	Tsang 2001 <sup>5</sup>
50	1	10	[0.75, 1.00]	50-60	SPB+EMP	Shih 1995 <sup>4</sup>
51	0.93	14	[0.66, 1.00]	50-60	SPB+EMP	Mayr 1990 <sup>32</sup>
62.5	0.5	2	[0.09, 0.91]	60-65	SPB+EMP	Shih 1995 <sup>4</sup>

The dose per fraction ranged from 1 to 5 Gy with ~2 Gy/fx being the most common. Explicit fractions sizes were not always specified in the papers reviewed. However, those studies reporting large deviations from the standard fractionation regimen of 2 Gy/fx mentioned that the common regimen was 2Gy/fx. This introduces uncertainty in the analysis but eliminating these data sets would have significantly reduced the already small pool of available data.

In addition, tumours are early responding tissues. The tumour cells cycle quickly and express radiation damage reasonably quickly; while late responding tissues, such as most organs at risk, cycle slowly and express radiation damage after a longer period (months). Due to this difference in tissue response, the mechanisms of cell killing in tumours depends mainly on the total dose delivered and are less affected by the fractionation scheme. On the other hand, fractionation becomes an important strategy in order to spare the normal tissues, giving time for late responding tissues to repair the damage caused by radiation. For this reason, including data from the small number of patients treated with fraction sizes different from 2 Gy/day is expected to have little effect on the determination of tumour dose response parameters.

Although there were not sufficient data from any one institution to perform a dose response analysis based on single-institutional trial, in some cases such as Knobel *et al*<sup>15</sup>, there were a few data points for different doses.

This study shows how the absence of a common treatment procedure increases the uncertainty and could affect the analysis even for a single institution. In columns 12, 14 and 16 of Table 2.2, the data of Knobel *et al.* are shown. A decrease of the LC probability while increasing the dose is evident. Variables such as tumour size, fraction size, and adjuvant chemotherapy were not included. Knobel *et al* reported 16% of the patients having chemotherapy. They also reported the largest variation in the fractionation scheme used in the

treatments. Tumour size was not reported. These shortcomings of the data could have an important effect on LC rate, and could explain the apparent anomalous data showing a slight decrease of LC rate with increasing dose.

Figure 2.3 shows a histogram representing the distribution of doses for patients treated, by disease. Most of the patients were treated with doses between 20 and 50 Gy leaving a gap in the low dose region. There are also more cases of SPB and SPB+EMP than EMP.

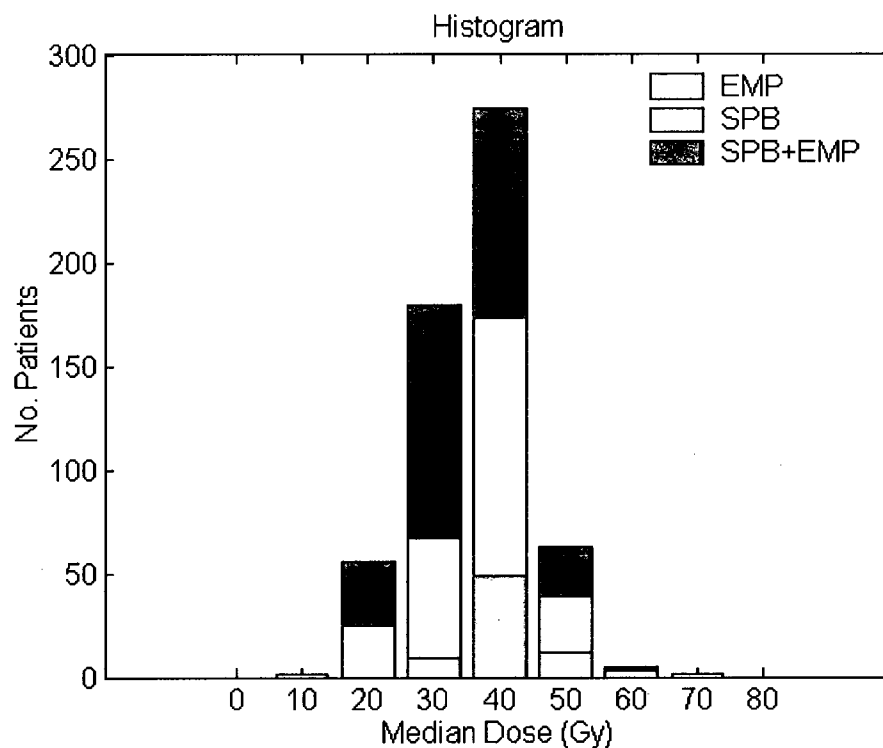


**Figure 2.3** Histogram of the number of patients per dose range for EMP, SPB and SPB+EMP.

### 2.5.2 ML fit of the clinical data

The clinical data selected for SPB, EMP and SPB+EMP and the ML fits are shown in Figures 2.4, 2.5 and 2.6 respectively. The y-axes of the graphs are labelled as TCP; however we estimated the tumour control probability using LC of the tumour as the end point.

Therefore, each data point in these figures represents the estimated LC probability given by the number of patients with LC (number of successes) divided by the total number of patients treated (number in trial) with the corresponding dose. This is equivalent in a binomial distribution to  $k_i^{Obs}/n_i^{Obs}$ , where  $k_i^{Obs}$  is the number of successes and  $n_i^{Obs}$  is the total number of trials for each dose  $D_i$  as explained in section 2.4.2. Even though each data point is associated in the graph to specific dose value  $D_i$ , the dose is in fact the median dose of an interval of at most 10 Gy. For example, the third row of Table 2.1 shows that 6 patients were treated with doses between 40 to 50 Gy (exact 50 Gy not included) and the median dose was 48 Gy. The LC probability was 1, which means that all 6 patients treated had achieved LC of the tumour ( $k_i^{Obs}/n_i^{Obs} = 6/6 = 1$ ).

The error bars represent the 68% Wald CI for binomial distribution. A zero dose zero LC data point (0,0) was also included in all cases, which assumes that the probability of LC would be equal to zero if no dose were delivered to the tumour.

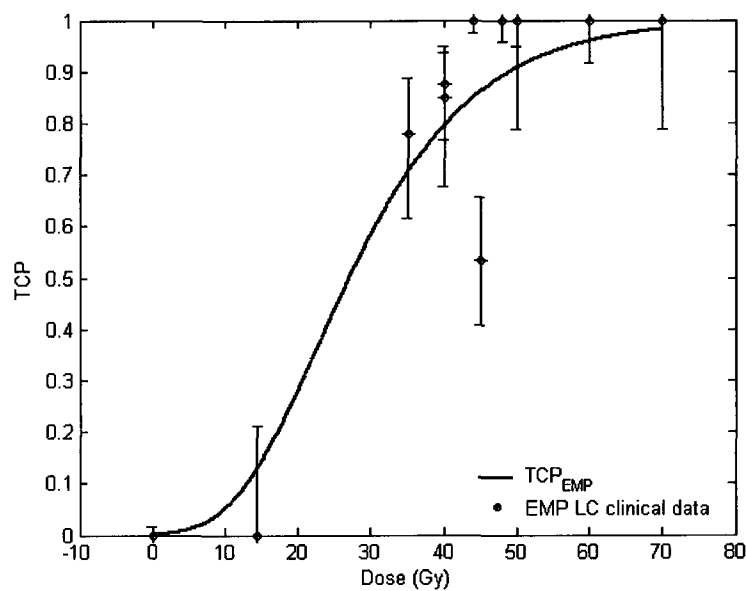


**Figure 2.4** LC clinical data and ML fit as a function of the radiation dose for patients with EMP. Error bars represent the 68% CI for a binomial proportion.

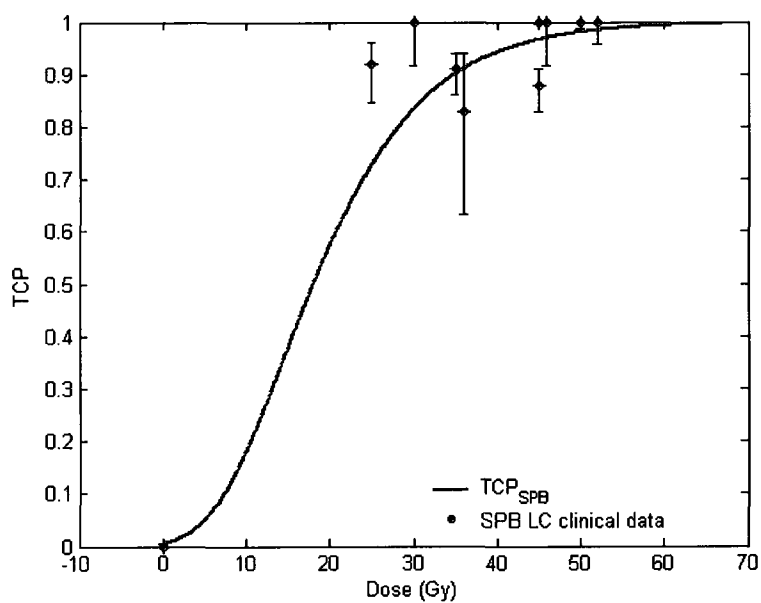


**Figure 2.5** LC clinical data and ML fit as a function of the radiation dose for patients with SPB. Error bars represent the 68% CI for a binomial proportion.

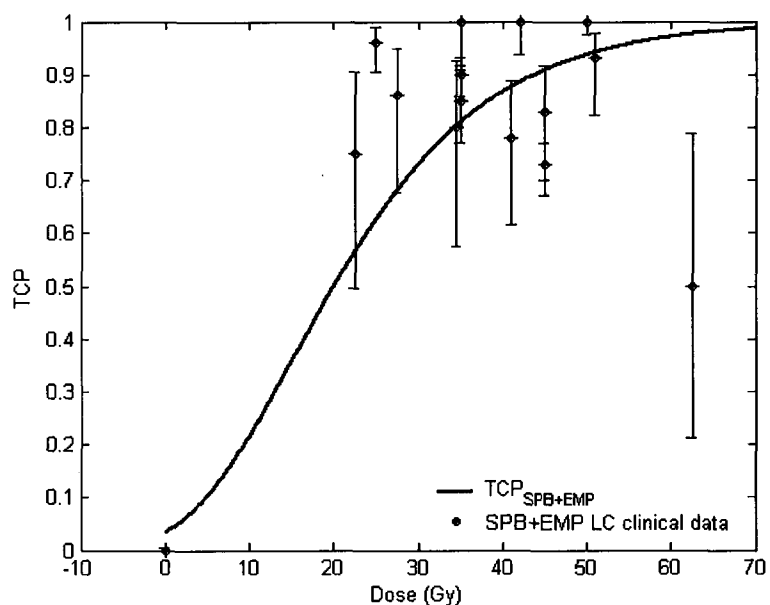


**Figure 2.6** LC clinical data and ML fit as a function of the radiation dose for patients with SPB+EMP. Error bars represent the 68% CI for a binomial proportion.

**Table 2.3** The TCP parameters  $D_{50}$  and  $\gamma_{50}$  from the ML fit and their symmetric errors (SD) for EMP, SPB and SPB+EMP clinical data. The 95% CI from Monte Carlo analysis (the lower and upper limits: [LL, UL]). Similarly the resulting values for SPB data but including 12 Gy zero local control TBI data point (SPB<sup>\*</sup>).

	$D_{50}$ (Gy)			$\gamma_{50}$ (%/%)		
	MLE	SD	95% CI <sub>MC</sub>	MLE	SD	95% CI <sub>MC</sub>
EMP	27	5	[21, 35]	0.8	0.4	[0.6, 1.9]
SPB	18	2	[14, 24]	0.7	0.1	[0.5, 1.4]
SPB+EMP	20	2	[17, 24]	0.6	0.1	[0.4, 1.4]
SPB <sup>*</sup>	23	1	[19, 27]	1.2	0.1	[0.8, 2.0]

<sup>\*</sup>Including 12 Gy zero LC TBI data point.

Table 2.3 shows the MLE of the TCP parameters and their SD. Using MC distributions, the 95%  $CI_{MC}$  were delimited with equal probability of 0.025 in the tail (2.5% each side). The lower and upper limits [LL, UL] of the 95%  $CI_{MC}$  for each parameter are also shown in Table 2.3.

Figure 2.7 graphically shows the MLE and the 68% (inner curves) and 95% (outer curves) likelihood CR defined by Equation 2.17 for EMP, SPB and SPB+EMP.

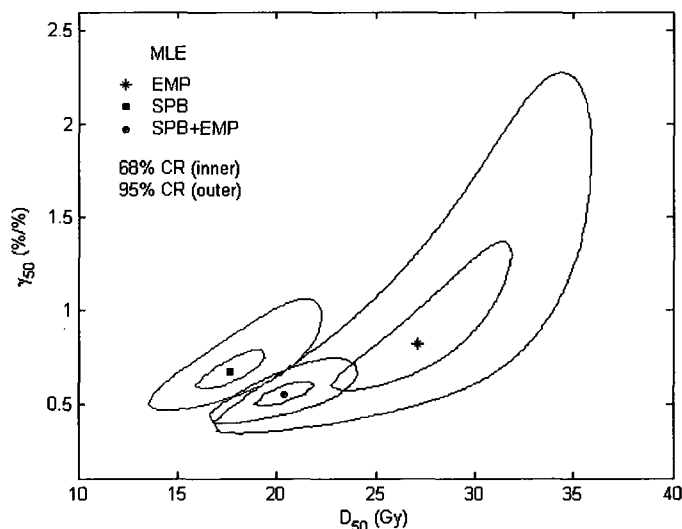


**Figure 2.7** MLEs from fitting the LC clinical data for EMP (star), SPB (square) and SPB+EMP (circle). The corresponding 68% (inner curves) and 95% (outer curves) CRs are also shown.

The 2D normalized histogram resulting from MC is shown in Figure 2.8 for EMP as an example. The colour map in Figure 2.9 shows simultaneously the 2D histograms on the parameter space for SPB and EMP MC data.

The 2D histogram is a plot of the parameter's value on the parameter space. Using MC 10000 simulated data sets were generated. Each simulated set was fitted resulting in one point in the histogram. This point simultaneously represents the values of  $D_{50}$  and  $\gamma_{50}$  (x and y axes). In total, 10000 data points are plotted. The colour scale corresponded to event frequency. The 68% and 95% likelihood CRs given by Equation 2.17 are also superimposed on the map for comparison.

In spite of the lack of LC clinical data for low doses, the results show that there are differences between the MLE obtained for EMP and SPB, which could lead to tumour discrimination. For instance, Table 2.3 shows that there is a significant difference between  $D_{50}$  values of the TCP model for EMP and SPB. By performing a simple statistical test, we can quantify how well the observed data agrees with either of the hypotheses, called  $H_{SPB}$  and  $H_{EMP}$ . Figure 2.10 shows the MC histograms for parameters  $D_{50}$  (a) and  $\gamma_{50}$  (b) for EMP and SPB data.

$H_{SPB}$  was considered the hypothesis to be tested against an alternative hypothesis  $H_{EMP}$ . A Type I error would occur when  $H_{SPB}$  is rejected, when it is in fact true. The critical value for the hypothesis test was simply defined as a 5% significant level. Thus, the probability of rejecting  $H_{SPB}$  if  $H_{SPB}$  is true is just 0.05. The probability of not rejecting  $H_{SPB}$  when  $H_{EMP}$  is true was 0.09. The power of the test to discriminate  $H_{SPB}$  against the alternative  $H_{EMP}$  was then 0.91. No significant difference was seen for  $\gamma_{50}$  as seen in Figure 2.10 (b) and Table 2.3.

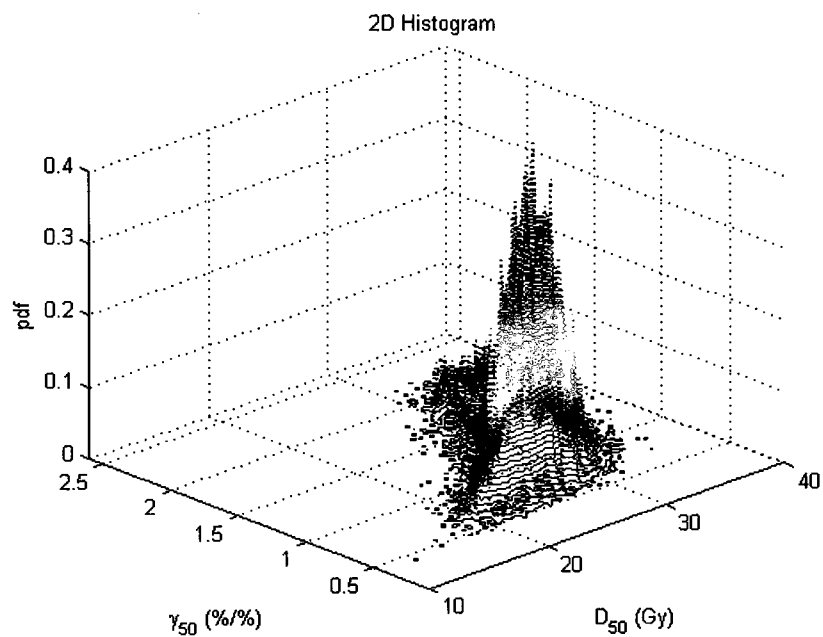


Figure 2.8 2D MC histogram of parameters  $D_{50}$  and  $\gamma_{50}$  for EMP.

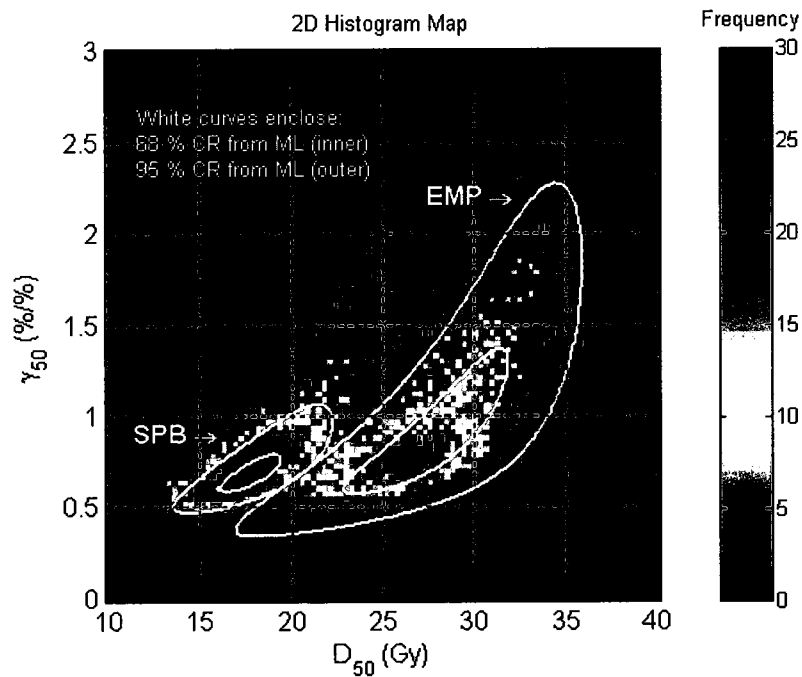


Figure 2.9 Colour map of the 2D MC histograms for SPB and EMP on the parameter space. The likelihood CRs are represented by the white curves. The inner and outer curves represent the 68% and 95% likelihood CRs respectively.

## 2.6 Discussion

Several authors have previously studied tumour dose response to radiation. However, TCP parameters have been mostly estimated for microscopic disease.<sup>33</sup> Okunieff *et al.* have done an extensive analysis on published clinical dose response data for many human tumours, but they did not include any plasma cell neoplasms.

Although a large volume of dose response data on plasmacytomas was reviewed in this study in an attempt to be inclusive, there were not sufficient data from any one institution to perform a dose response analysis. In a multi-institutional analysis, a more reliable analysis is difficult because of the absence of a common treatment procedure. Any specific effects of chemotherapy, fraction size and fractionation schedule were ignored. The follow-up time was not consistently available or differed from one report to another and so was also ignored. However, the majority of the studies had the common elements of radiation therapy as the main treatment and fraction size of about 2 Gy/fx. In spite of the limitations of a lack of low dose data and the reporting of data within dose ranges, the approach taken here represents a reasonable approximation and can be considered as a preliminary assessment of the dose response relationship for plasma cell neoplasms, considering the quality of published data.

The concept of MM, SPB and EMP being just a variation of one tumour type or completely different diseases, is not clear and varies depending on the author,

resulting in clinical data published separately for SPB and EMP or together (SPB+EMP). Therefore, in each case data were collected and analyzed independently.

EMP data show a well-defined trend, but this is not the case of SPB and SPB+EMP data. All the data that met our initial criteria were kept for the fit even if it did not follow the general trend. For example, in Figure 2.4 there was a study that reported an observed LC probability of 0.53 at 45 Gy equivalent to 8 LC cases out of 15 patients treated, much lower than expected. However, if our model is considered correct, an outcome like this would take place in one out of 1000 times so it is still statistically possible. A similar situation happened at 62.5 Gy for SPB+EMP data (Figure 2.6), especially if only 2 patients were included within this dose range.

The non-elliptical shape of the likelihood CR suggests that the distribution of at least one of the parameters is not Gaussian leading to asymmetric errors. It should be kept in mind that likelihood CRs are an approximation of the classical confidence interval that would be exact only in the large sample limit. In consequence, EMP data is more affected and have a larger CR since the sample size is smaller than for SPB. In addition, the MC data showed a noticeable increase of possible  $\gamma_{50}$  due to the inclusion of 10 Gy dose range. The lack of low dose response data and the fact that the data is given within a dose range affect the parameter accuracy. The parameter  $\gamma_{50}$  is more sensitive to biological

differences (tumour size, growth site, histology) and variation in the treatment<sup>34-36</sup> than  $D_{50}$ . To obtain more reliable values of  $\gamma_{50}$ , more data along the low dose region are necessary.<sup>33</sup>

In spite of the uncertainty of the parameters, significant differences were seen between the MLE obtained for EMP and SPB. Figure 2.9 shows that the 95% likelihood CRs did not intercept and even including the 10 Gy dose interval, MC analysis showed that the power of the test to discriminate SPB and EMP data based on  $D_{50}$  distribution was 0.91. However,  $\gamma_{50}$  did not show any significant difference.

Localized plasmacytomas, *e.g.* SPB and EMP, in contrast to MM, could be cured and a long-term survival could be achieved as a result of radiation therapy treatment. Even though EMP is considered to have better outcomes than SPB, the dose at 50% control probability for SPB (18 Gy) is 33% lower than for EMP (27 Gy) as seen in Table 2.3. This is due to the fact that this study was intentionally based on LC clinical data since we tried to discriminate dose response relationship from many other associated factors. It is recognized that SPB often progress to MM despite successful LC of the tumour. Overall survival and disease free survival are usually lower than LC rates, the adverse factors being patient older age and bone involvement.<sup>3, 5</sup> Using LC as the end point is a reasonable approach for a dose response study. However, the tumour size was not taken into account because of the absence of this information in the majority

of the clinical reports. This can affect the LC-data since larger tumours are associated with local failure in several studies of solitary plasmacytomas treated with radiation therapy.<sup>3, 5</sup> Special attention should be paid to this issue in future analysis.

In this study, a dose response relationship for plasma cell neoplasms was estimated and possible differences between SPB and EMP were evaluated. However, the results should be interpreted with caution in any further application or use of the values due to the present limitations of the available data. More reliable outcomes could be found if the data were more specific and all details of the data were included in the publication, which is recommend for future clinical studies.

# **Chapter 3**

## **Radiobiological modeling of a proposed dose escalation in TMI**

### **3.1 Introduction**

Clinical dose response data of human tumours are limited or restricted to a dose range determined by the level of toxicity to the normal tissues. This is the case for a common disseminated plasma cell neoplasm, multiple myeloma (MM), where the maximum dose deliverable to the entire bony skeleton using a standard total body irradiation (TBI) technique is limited to about 12 Gy. The main limitation is treating the large volumes of bone marrow involved in this disease without excessive normal tissue complications. Recently, clinical trials

have been developed for targeted treatment in MM patients using total marrow irradiation (TMI) with Helical TomoTherapy (HT).<sup>8, 9, 11</sup>

The aim of this study was to provide a tool for comparing and predicting the effectiveness of different approaches to TMI using HT. The primary goal was to perform a radiobiological evaluation of different treatment cohorts in a dose escalation study. Normal tissue complication probability (NTCP) and tumour control probability (TCP) models were applied to an actual TMI treatment plan for a patient. A secondary goal was to assess the implications of using different longitudinal field lengths with the goal of reducing planning and delivery time while maintaining TCP without causing unacceptable increases in NTCP.

## **3.2 Materials and methods**

### **3.2.1 Dose escalation study in a patient**

A whole-body CT scan from a 55 year-old male was used for this study. This patient was not a multiple myeloma patient and did not undergo TMI treatment. The whole-body CT scan was performed for medical reasons related to management of the patient's cancer and with his consent the scan data was used for planning studies for TMI. The TMI treatment was planned on the TomoTherapy Hi-Art treatment planning system. The target region was defined as all skeletal bone superior to the mid-femur. Bone in the lower extremities was

excluded since the maximum distance that the patient treatment couch can travel is 160 cm, which limits the length of the treatment volume. The treatment was designed to deliver 20 Gy in 10 fractions with 87% of the GTV to be covered by the prescribed dose ( $D_p$ ).<sup>11</sup> Planning modulation factor was 2 and pitch was 0.287. The pitch value was chosen to reduce the thread effect that characterizes helical delivery and will be discussed in the next chapter. Field widths of 25 and 50 mm were examined. Total marrow irradiation using HT is a relatively new type of treatment for patients with MM. Some details of the procedure and their rationale are still under study and development.<sup>8, 9, 11</sup>

The treatment plan was designed to deliver the prescribed dose to 87% of the GTV. It is very difficult to deliver the standard 95% to the entire bone marrow without violating the toxicity dose limits to the critical organs. Previous studies have reported values of 82% and 85%<sup>8, 9, 11</sup> so we went a bit further without exceeding the normal tissue dose limits established by the oncologist.

In addition, the GTV was considered the target rather than the PTV. No margins were included to account for the set up uncertainties and organ movements as is normally done in conventional radiotherapy. In a reasonable treatment plan, the margins should vary along the body depending on tumour size and the dose tolerance of the organs at risk surrounding the target. This would complicate the model and needs further study. From the fact that just 87% of the GTV is planned

to receive the prescription and that margins were not included, some underdosing of the target is expected.

Tumour and sensitive structure constraints were optimized for a 20 Gy TMI plan with 25 mm field width and kept the same for 50 mm field width treatment plan. The dose escalation study was performed by linearly escalating the 20 Gy DVH to other prescribed doses.

The dose constraints used during the plan optimization were given by the oncologist and were based on clinical experience with 12 Gy TBI treatments and other studies.

The dose limiting constraints to the OAR were:

1. Between 75-80% of the volume of the OARs should receive less than 12 Gy.
2. 25% of kidneys should not receive more than 25 Gy and 10% of the kidneys should not receive more than 10 Gy.
3. For other OARs, 30% of the volume should not receive more than 12 Gy.
4. By order of importance the OAR were: Lungs, kidneys, liver, brain, heart, oral cavity, small bowel. Other organs also used in the analysis had low importance.

5. Keep OAR dose as low as possible, consistent with achieving the goal of delivering the prescribed dose to 87% of the GTV.

### 3.2.2 Normal tissue complication probability

The assessment of treatment-related normal tissue toxicities was based on the NTCP from dose volume histograms (DVH). The Lyman probit model<sup>37</sup> with the Kutcher-Burman reduction algorithm (LKB)<sup>38</sup> was used to evaluate NTCP. The Lyman model empirically describes the sigmoidal dose response curve of normal tissues using the probit form:

$$NTCP = \Phi\left(\frac{EUD - TD_{50}}{mTD_{50}}\right) \quad (3.1)$$

$$\Phi(x) = \frac{1}{\sqrt{2\pi}} \int_{-\infty}^x \exp\left(-\frac{t^2}{2}\right) dt = \frac{1}{2} \left[ 1 + \operatorname{erf}\left(\frac{x}{\sqrt{2}}\right) \right] \quad (3.2)$$

$$EUD = \left( \sum_i V_i D_i^{1/n} \right)^n \quad (3.3)$$

where  $\Phi(x)$  is the probit function defined by Equation 3.2 with  $x=(EUD-TD_{50})/mTD_{50}$ .  $TD_{50}$  is the tolerance dose to the whole organ that would yield a complication probability of 50%  $m$  is a measure of the slope of the dose-response relationship and  $n$  describes the volume effect. EUD is the equivalent uniform dose which represents the dose that, if delivered uniformly to the entire

organ, would produce the same effect as the given heterogeneous dose distribution as specified by the DVH.<sup>22, 38</sup>  $V_i$  and  $D_i$  are the volume and the dose. EUD was assumed to be equal to generalized mean dose and was calculated from dose-volume pairs  $(D_i, V_i)$  using Equation 3.3. The parameters characterizing NTCP were obtained from the results published by Burman *et al.*<sup>39</sup> from fitting the tolerance data for many organs compiled by Emami *et al.*<sup>40</sup> The values of the NTCP parameters used are shown in Table 3.1.

**Table 3.1** Normal tissue tolerance parameters and end points published by Burman *et al.*<sup>39, 40</sup> The  $TD_{50}$  is the tolerance dose to the whole organ that would yield a complication probability of 50%,  $m$  is a measure of the slope of the dose-response relationship and  $n$  describes the volume effect. The end points for which the parameters were calculated are also shown.

Organ	Fit parameters			End Point
	$n$	$m$	$TD_{50}$	
Bowel	0.15	0.16	55	Obstruction/Perforation
Brain	0.25	0.15	60	Necrosis/Infarction
Esophagus*	0.06	0.11	68	Stricture/Perforation
Heart	0.35	0.10	48	Pericarditis
Kidney	0.70	0.10	28	Nephritis
Lens	0.30	0.27	18	Cataract
Liver	0.32	0.15	40	Liver failure
Lung	0.87	0.18	24.5	Pneumonitis
Parotid**	0.70	0.18	46	Xerostomia
Retina	0.20	0.19	65	Blindness

Values also used for oral cavity for the end points of mucositis\* and xerostomia\*\*

### 3.2.3 Tumour control probability

Tumour control was evaluated using a TCP model based on Poisson statistics.<sup>22</sup> In Chapter 2, it was shown that this model can be written in terms of  $D_{50}$  and  $\gamma_{50}$ , parameters that describe the dose and the slope at the point of 50% probability of control. In inhomogeneous irradiation the overall probability of tumour control is the product of control probability in each  $i^{\text{th}}$ -subvolume  $V_i$  under the assumption of subvolume independence. Then Equation 2.1 becomes:

$$TCP = \prod_i TCP(D_i, V_i) = \left(\frac{1}{2}\right)^{\sum_i V_i \exp[2\gamma_{50}(1-D_i/D_{50})/\ln 2]} \quad (3.4)$$

The TCP parameters used [ $D_{50} = 23\text{Gy}$  (95%CI: 19, 27) and  $\gamma_{50} = 1.2\%/%$  (95%CI: 0.8, 2)] were obtained previously in Chapter 2. Dose escalation analysis was performed by linearly escalating the differential DVHs obtained from the original 20 Gy TMI plans for 25 and 50 mm field widths to any prescribed dose.

## 3.3 Results

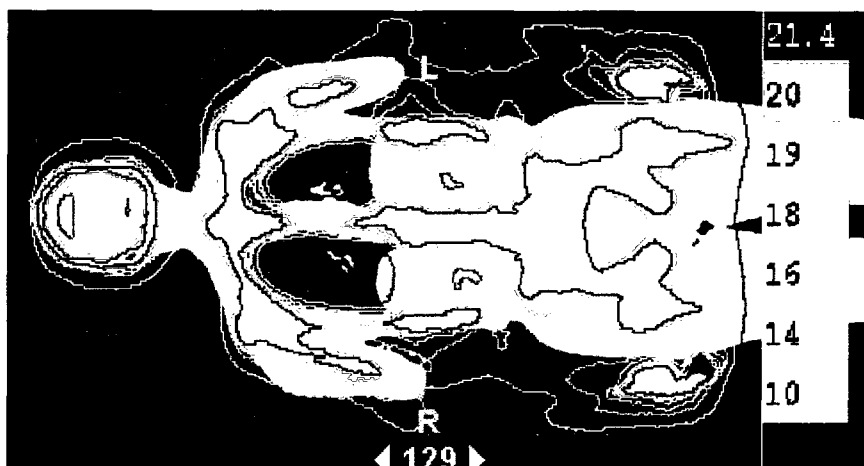
### 3.3.1 Dose distribution and DVHs

The aim of this study was to provide a tool to compare and predict the effectiveness of different approaches to TMI using HT. One of the first results was that the treatments last twice as long with the smaller field as with the larger

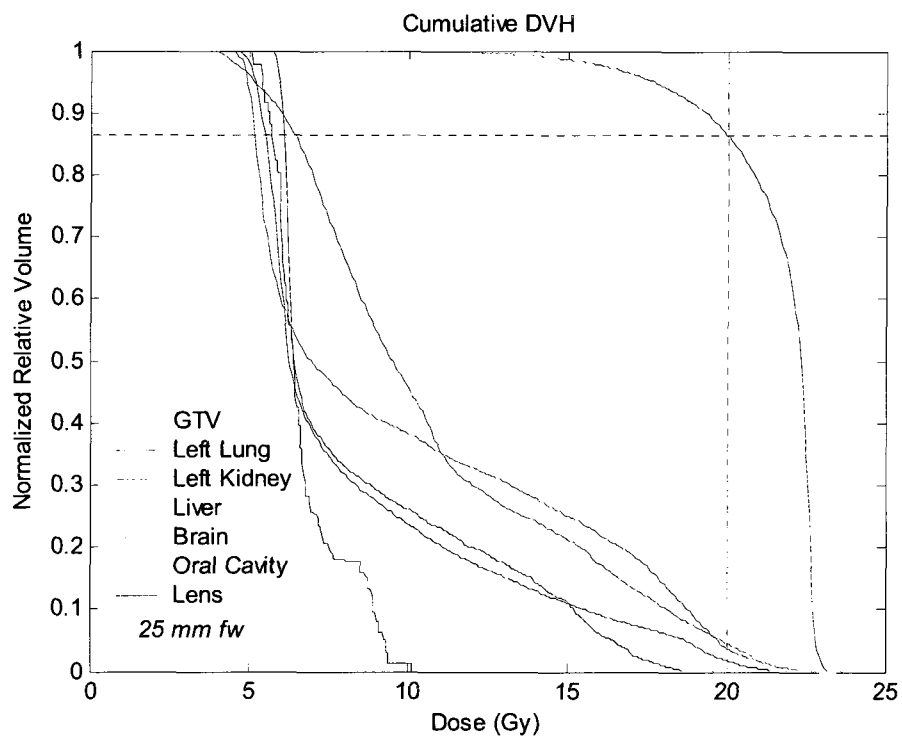
field width. The treatment times were 46.8 min and 23.7 min for a field width of 25 mm and 50 mm respectively. In radiation therapy, minimizing beam-on time while achieving a reasonable treatment is one of the goals. In TMI this is even more important since the target is large and it is not only uncomfortable for the patient, but positioning uncertainty increases if the patient lies on the treatment table for long periods of time, due to patient motion and organ motion. In addition, long treatment times lead to lower patient throughput per treatment machine, and consume scarce health care resources.

Figure 3.1 shows a coronal view of the dose distribution for a patient receiving 20 Gy TMI with a field width of 25 mm. The figure shows most of the bone structure and the isodose map. In the region of the thorax between lungs, and in the neck, the isodose distribution shows regions of underdosing. These are apparent cold areas which do not appear in all slices, since one slice of 3 mm cannot pass through the entire bone structure along the coronal view. However, some underdosing is also expected based on the treatment plan (87% of the GTV receiving prescription). There are studies showing the limitations of the superposition algorithm used in HT in regions of lateral electronic disequilibrium.

The DVHs for the GTV and major organs at risk are shown in Figure 3.2. Doses for 80%, 50% and 10% of the volume of the left lung from 20 Gy TMI are in Table 3.2. Values from a previous study from 12 Gy TBI are also shown for comparison.



**Figure 3.1** Coronal view of a TMI plan to a  $D_p$  of 20 Gy. The dose distribution is also shown (Isodoses from 6 to 21.4 Gy).



**Figure 3.2** DVHs for some normal organs: Left lung (blue), left kidney (green), liver (cyan), brain (pink), oral cavity (yellow), lens (black). The DVH for the GTV is in red. The two dashed lines at the dose of 20 Gy and 87% of the volume show that the plan of delivering 20Gy to 87% of the GTV was achieved.

**Table 3.2** Doses for 80%, 50% and 10% of the volume ( $D_{80}$ ,  $D_{50}$  and  $D_{10}$ ) from 20 Gy TMI and 12 Gy TBI plans in lung.

	TBI 12 Gy Wong <i>et al.</i>	TMI 20 Gy This study
$D_{80}$	7.0	5.6
$D_{50}$	9.4	6.3
$D_{10}$	12.3	15.7

### 3.3.2 Tumour control probabilities in TMI

A comparison between GTV differential DVHs for 25 and 50 mm field width is shown in Figure 3.3. Even though a 25 mm field resulted in a more homogeneous dose distribution to the target than 50 mm field width, TCP curves exhibited little variation as seen in Figure 3.4. The TCPs for the original  $D_P$  of 20 Gy TMI plan for 25 mm and 50 mm field widths are in Table 3.3.

**Table 3.3** TCP values of a 20 Gy TMI plan for 25 mm and 50 mm field widths and uniform dose of 20 Gy. TCP values were obtained from applying Poisson model to the tumour dose distribution in a TMI patient.

TCP ( $\pm 9\%$ )		
Field Width		
20 Gy	25 mm	50 mm
TMI	40%	42%
Uniform	35%	

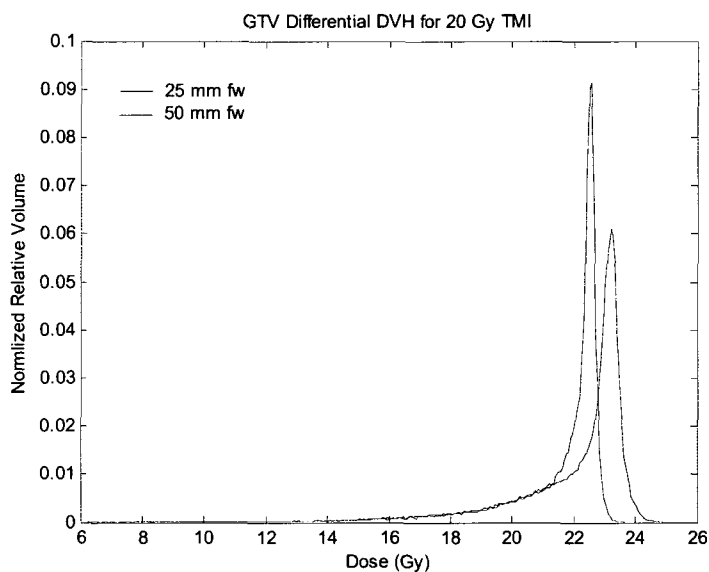


**Figure 3.3** GTV differential DVHs for a patient receiving 20 Gy TMI for 25 mm (red) and 50 mm (blue) field widths. The 25 mm field resulted in a more homogeneous dose distribution to the target than 50 mm field width.

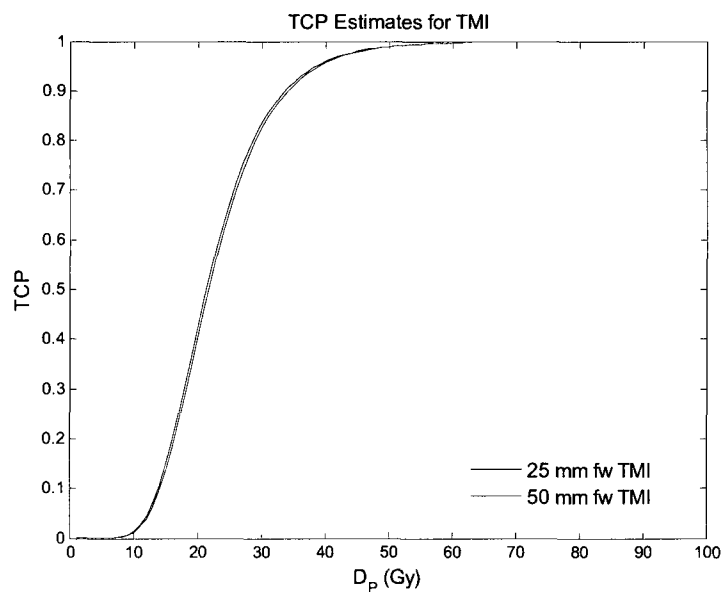


**Figure 3.4** TCP curves as a function of  $D_p$  for TMI treatment with 25 mm (red) and 50 mm (blue) field widths. The curves exhibited little variation. The curves were obtained using Poisson model and linearly escalating the DVH to any prescribed dose.

### **3.3.3 Normal tissue complication probabilities in TMI**

NTCP estimates for some of the major normal organs studied are shown in Figure 3.5, organs in the torso (a) and head (b) as a function of the prescribed dose to the GTV. A comparison between 25 mm (solid) and 50 mm (dashed) fields is shown. The curves on the left of the graphs represent the organs experiencing higher tissue complication at lower doses. The organs experiencing higher tissue complication were lungs, kidneys, liver and lens in Figure 3.5.

## **3.4 Discussion**

The TMI treatment was planned on the TomoTherapy planning system and the longitudinal treatment length is limited to about 140 cm. The longitudinal travel of the treatment couch inside the bore is 160 cm, but there are various reasons why this full length is not available for treatment. However, longitudinal junctioning is not supported by the TomoTherapy treatment planning software. That is why the model presented here was restricted to bone superior to the mid-femur, excluding bone in the lower extremities (which contain a small proportion of the marrow of the body). However, the important organs at risk are located superior to mid-femur and were all included. Thus, the specific values of TCP resulting from the analysis could vary for the total marrow study; however, the general understanding and main conclusions are still valid.

In addition, the treatment plan was designed to deliver the prescribed dose to 87% of the GTV. From the fact that just 87% of the treatment volume was planned to receive the prescription and that margins were not included, underdosing of the target was expected. However, historically MM patients have not been treated with the levels of radiation used in this study. The usual treatments are a combination of chemotherapy, 12 Gy TBI, and bone marrow transplant, which leaves the patients with an overall survival of about 2 ½ year. Therefore, the rationale for TMI treatment as discussed in Chapter 1 is still reasonable.

TCP values did not show significant differences between TMI treatments with 25 and 50 mm field widths as seen in Figure 3.4 and low tumour control is expected (TCP about 40%) for 20 Gy TMI plan.

The organs experiencing higher normal tissue complication were lungs, kidneys, liver and lens in Figure 3.5. This corresponded to the organs with lower tolerance doses for whole uniform volume irradiation whose TD<sub>50</sub> values were 24.5, 28, 40 and 18 Gy respectively, for the end points of pneumonitis, clinical nephritis, liver failures and cataracts.<sup>39, 40</sup> Lens has a very low tolerance (18 Gy) and even with a conformal irradiation technique like HT toxicities are expected. However, cataract is a complication that is easily treatable, especially when the aim of TMI is the management of multiple myeloma patients with relapse or otherwise poor prognosis.

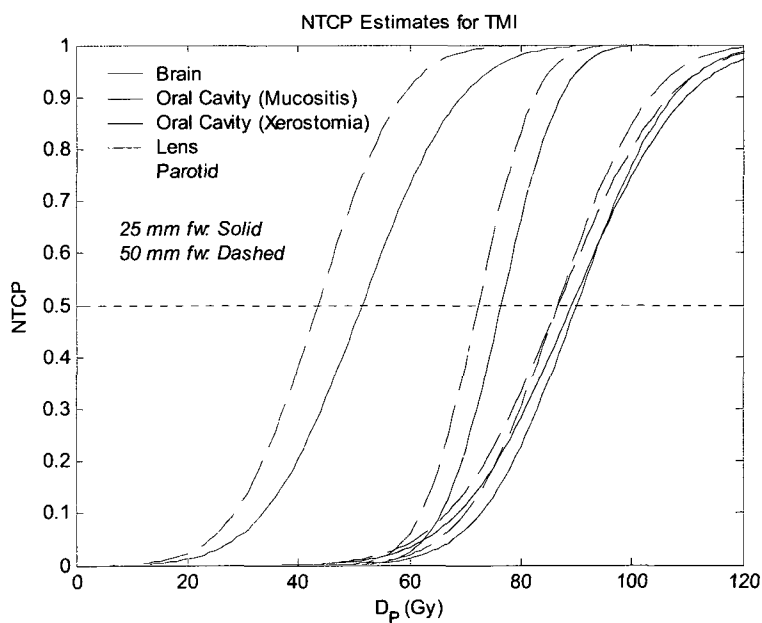
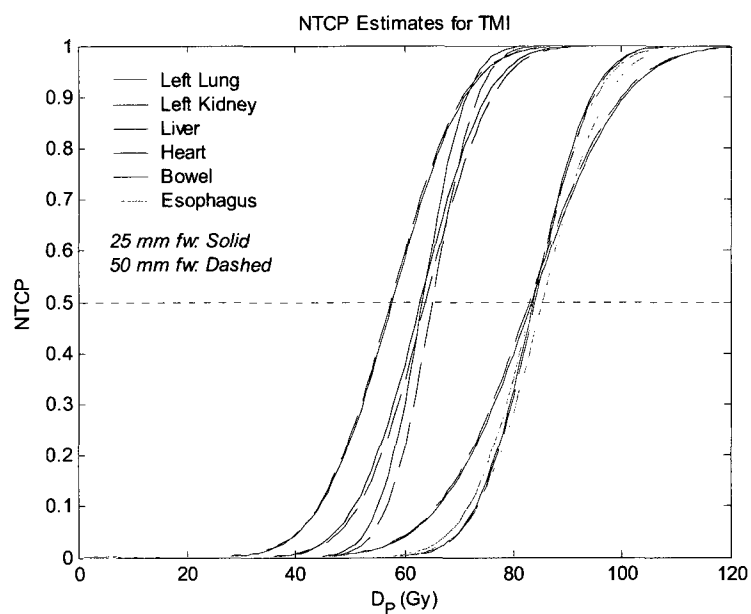


**Figure 3.5** NTCP curves as a function of the  $D_p$  for TMI treatment with 25 (solid) and 50 mm (dashed) field widths. The major normal organs, in the torso (a) and the head (b). There was not a substantial difference between NTCP values using 25 mm or 50 mm field widths for most of the organs in the torso. The normal tissue sparing effect is seen by using smaller fields (25 mm) in the organs of the head. The curves were obtained using Lyman model and linearly escalating the DVHs to any prescribed dose.

There was not a substantial difference between NTCP values using 25 or 50 mm field widths for most of the organs in the torso. The prescribed dose to the GTV that would lead to a normal organ complication of 50% from the TMI plan using HT ( $D_{P/50}$ ) is represented by the dose at the intersection of each NTCP curve and the horizontal dotted black line (NTCP equal 0.5). For organs of the torso, the difference in  $D_{P/50}$  between 25 and 50 mm was less than 3% (see Figure 3.5 (a)). For organs in the head, the  $D_{P/50}$  for 50 mm field width was consistently lower by up to 15% compared to 25 mm field width (see Figure 3.5 (b)). Changes in TCP and NTCP for organs in the torso do not support the use of the 25 mm field. In addition there are no ostensible advantages particularly when treatments with 25 mm field (46.8 min) last twice as long as those with 50 mm (23.7 min). The gantry period was 20 s in both cases.

The normal tissue sparing effect seen by using smaller fields in the organs of the head is significant. These calculations suggest that it would be advantageous to use the smaller field width in the head to achieve lower NTCP, but switch to 50 mm field width in the torso in order to reduce overall treatment time. The challenges associated with junctioning two tomotherapy treatments with different field widths are addressed in Chapter 4.

The optimum choice of radiation dose in a treatment is that which simultaneously maximizes the TCP and minimizes the NTCP. This criteria is represented by the product of  $TCP(1-NTCP)$ , called probability of uncomplicated cure. Lungs happen

to be one of the most important organs at risk in TMI, with the lowest  $D_{P/50}$  (57 Gy) after lens (44 Gy). Figure 3.6 shows TCP, NTCP for the left lung and TCP(1-NTCP) curves for 50 mm field width as a function of the  $D_P$ . Left and right lungs were analyzed separately and differences between them were very small. Then, the left lung was plotted since left lung includes large volume of the heart, but the analysis was performed in both lungs and showed minimal difference. Independently of the field width and for both lungs, the maximum was reached between 38 and 39 Gy, for which 95% ( $\pm 3\%$ ) of tumour control and 3% (0, 8%) occurrence of radiation pneumonitis was obtained.

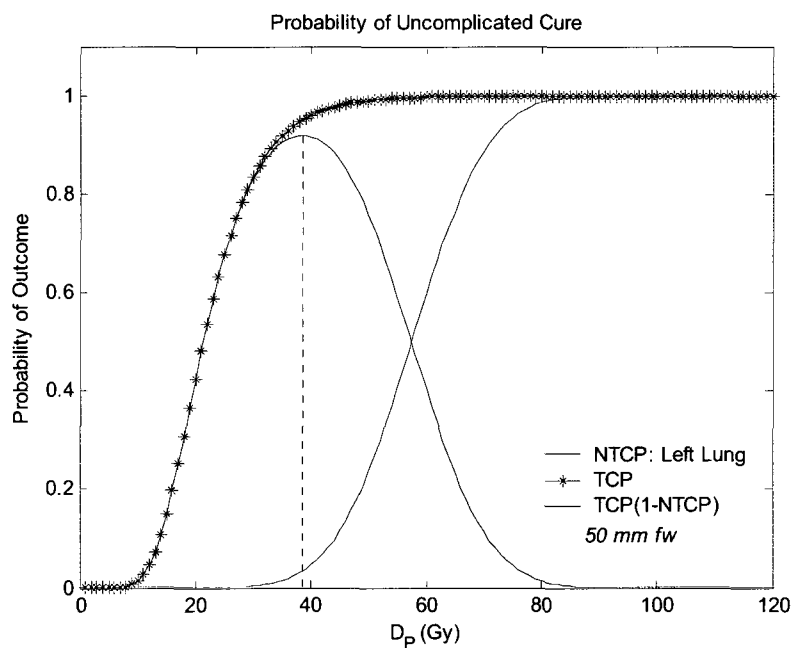


**Figure 3.6** The curves of NTCP, TCP and the probability of uncomplicated cure TCP(1-NTCP) as a function of  $D_P$  for 50 mm field width for left lung. The curves were obtained using Poisson and Lyman models and linearly escalating the DVHs to any prescribed dose.

Even though according to this model 39 Gy seems to be the optimum radiation dose, there are some conditions of the model that need to be taken into account. The initial treatment plan was designed to deliver a prescription of 20 Gy. The plan was optimized based on the normal tissue criteria set by the oncologist and the dose limits obtained from 12 Gy TBI studies. In section 3.2.1 the dose limiting constraints used during the optimization were reported. The DVHs in Figure 3.2 showed that the first constraint was easy to achieve, and 75% of the volume of the OARs received a dose much less than 12 Gy. However, the second and third conditions were barely achieved in some cases (kidneys, lens, oral cavity and brain), while in liver it was not achieved.

The dose escalation study was performed by linearly escalating the 20 Gy DVH to other prescribed doses, which translates in Figure 3.2 to a shift in the entire DVH to the new prescribed dose. For example, if the new prescription was to deliver 25 Gy instead of 20 Gy (5 Gy more), all histograms would shift to the right. The 87% of the PTV would still be covered by the prescription but this time would be at 25 Gy. The first planning constraint would also still be met (if  $D_{80}$  for lungs was 5.6 Gy in the 20 Gy TMI plan, then for the 25 Gy TMI plan it would be 10.6 Gy). However, it would be impossible to achieve the second and third planning constraints.

How normal organs respond to inhomogeneous dose to the volume (also called volume effect or dependence), varies for each particular organ and further

studies are needed. That is why the patients involved in the clinical trial receive doses just between 12 to 28 Gy. Analyzing the patient response from the clinical trial should allow us to validate and improve the model.

# Chapter 4

## Junctioning longitudinally adjacent PTVs with Helical TomoTherapy

### 4.1 Introduction

Helical Tomotherapy (HT) is a relatively new radiation therapy technology that can deliver highly conformal dose distributions to complex target shapes while reducing the dose to critical normal tissues. It is an accepted treatment modality for many cancers such as head and neck,<sup>41-49</sup> prostate,<sup>50-52</sup> spinal metastasis,<sup>53</sup> CNS<sup>41</sup> *etc.* where the ability to plan and deliver highly conformal complex dose distributions under image guidance is thought to hold benefit.

There arise clinical situations where it is necessary or of benefit to junction two different longitudinally adjacent treatment volumes to form a contiguous treated

volume (PTV). A common clinical example is the need to treat a recurrence (or new lesion) PTV that is just superior or inferior to a previously treated PTV. Another example, as important but less obvious, is where significant clinical gain can be achieved by treating different longitudinally adjacent volumes with different field widths. Such a case could arise where the transverse cross section in one portion of the PTV varies slowly in the SUP-INF direction, but in another region the transverse cross section varies rapidly with longitudinal position. The former would lend itself to treatment by a large field while the later would receive a more conformal distribution (reduced NTCP) if treated by a smaller field width. With the existing Tomotherapy unit, this requires planning two separate PTVs, each with a different beam, to form one contiguous dose volume.

Another instance of clinical importance where we see this, and the primary objective of this work, is when breaking a contiguous PTV into two regions to allow one region to be treated with a small field to gain better PTV/OAR conformance and the second region to be treated with a larger treatment field to reduce the overall treatment time. A clinical example of where this is useful is total marrow irradiation. Tomotherapy also limits the bed travel to 160 cm, so for treatments such as total marrow irradiation<sup>7-10</sup> of tall patients two separate adjacent PTVs must be planned and treated to form a contiguous volume.

TomoTherapy software does not currently support longitudinal junctioning of two treatment volumes that have been separately planned. In this work we examine

the dosimetric issues of longitudinally adjacent PTV junctioning with Tomotherapy and the influence that parameters such as field width, pitch, and PTV location have on the integral dose distribution.

## **4.2 Materials and methods**

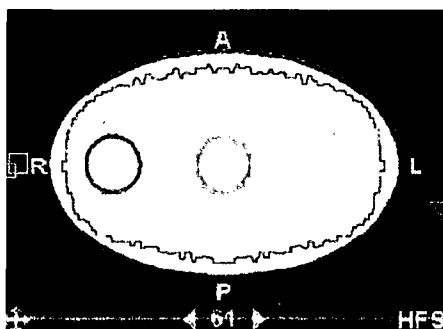
Irradiation of longitudinally adjacent PTVs with HT may be clinically necessary. In this work, the parameters which influence the cumulative dose distribution resulting from treating longitudinally adjacent PTVs are examined, including field width, pitch, and PTV location. In-phantom dose distributions were calculated for various on and off axis cylindrical PTVs and were verified by ion chamber and film measurement.

Integral dose distributions resulting from the junctioning of identical and different fields were calculated by summing individual dose distributions separated by different spacings. The study considers adjacent fields of different pitches and field widths and also examines cases where the volumes of interest are at different distances from the gantry axis. Cumulative and differential dose volume histograms were calculated and analyzed.

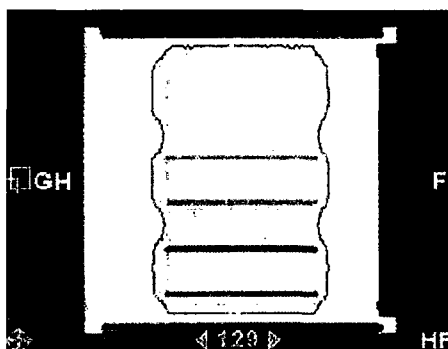
#### 4.2.1 Geometry and setup

Planning and measurements were performed on a pseudo-anthropomorphic homogeneous phantom, consisting of an acrylic (PMMA) elliptical (major axis 30 cm, minor axis 20 cm) cylinder (27 cm long). Within the phantom three parallel cylindrical 14.4 cm long PTVs were defined. The axis of each PTV is parallel to the Y-axis<sup>54</sup> of the HT machine with one being on the Y-axis (on-axis, X=0), and the other two being off-axis at X equal +9.4 (left) and -9.4 cm (right). There was a 6 cm margin between the caudal and cranial edges of the phantom and INF and SUP borders of the PTVs respectively. The axial, sagittal and coronal views of the phantom and the PTVs are shown in Figure 4.1. A TomoTherapy Hi-Art System (TomoTherapy Inc., Madison, WI, USA) was used for the planning, optimization and dose delivery.

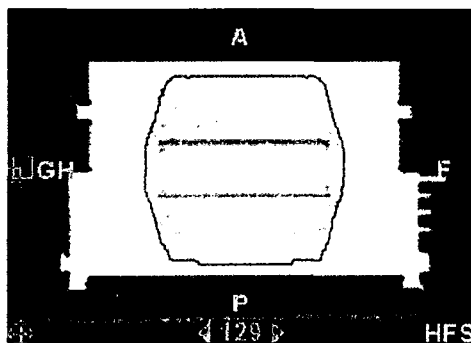
The first experimental step in this work was to dosimetrically verify the dose distributions predicted by the planning system. Experiments consisted of creating plans to deliver 4 Gy per fraction to each PTV for two of the three available field widths. The planned treatments were then delivered to the phantom and the resulting dose distributions for single PTV plans were measured with Kodak EDR2 film. A single point in each PTV was measured with an ADCL calibrated Standard Imaging A1SL ion chamber and Fluke electrometer (model: KEITHLEY 35040 Therapy Dosimeter).



(a)



(b)



(c)

**Figure 4.1** Axial (a), coronal (b) and sagittal (c) views of the phantom, PTVs, and isodose distribution calculated by the TPS for 25 mm field and pitch of 0.3.

The calculated 3D dose distributions for each of the different field widths, pitches, off axis distances and PTVs were then exported as DICOM images for offline processing in MATLAB R2007a. In this environment and with software developed for this task, the 3D junctioned dose distributions were calculated as the sum of two dose distributions and then analyzed. This was done by summing two different distributions spatially offset from each other to correspond to the cranial-caudal (CC) distance between two adjacent PTVs used to form a contiguous volume. This offset distance will be referred to as junction spacing (JSpac) as seen in Figure 4.2.

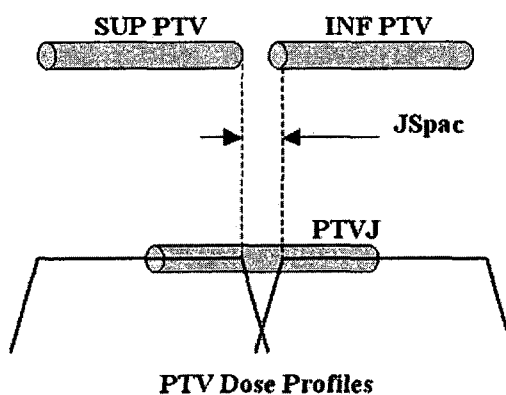


**Figure 4.2** Scheme of PTVJ definition within the junction region.

New cylindrical PTVs, referred to as PTVJs were then defined to contain the volumes of the junctions between the initial PTVs. In order to assess the dose homogeneity and compare to a reference dose distribution, the PTVJs were

selected such that the junction region was included (in the middle) and had the same cross-sectional area and length as the original SUP and INF PTVs shown in Figure 4.2. Having all the same volume (PTVs and PTVJs), the DVHs and dose profiles in these PTVJs are compared to reference dose distributions for a single PTV planned and treated with a continuous field.

#### **4.2.2 Treatment planning procedure**

The phantom was imaged on a Philips Brilliance CT-Simulator at 120 KV. The Hounsfield number to physical density (used in HT planning) included a value for PMMA ( $1.18 \text{ g/cm}^3$ )

A total of 120 slices, 3 mm thick, were acquired. The PTVs were outlined on the PINNACLE<sup>3</sup> version 7.6c planning station and exported to TomoTherapy Planning Station (TPS). The prescription was 20 Gy in 5 fractions (4Gy/fx) with 95% of the PTVs to be covered by the prescribed dose ( $D_p$ ). Treatments were designed to deliver a uniform dose to one or multiple PTVs. Field widths of 25 and 50 mm at pitches of 0.3 and 0.45 were examined. An initial modulation factor of 2 was used. The other parameters of the planning process including importance, maximum and minimum doses, DVH dose and penalties were optimized at the beginning and kept constant for all subsequent experiments. Figure 4.1 shows the axial, coronal and sagittal phantom images, the PTVs and

the planned isodose distribution for a 25 mm field and a pitch of 0.3. The 3D dose matrices calculated by the TPS and the vectors defining the PTV structures were then exported for offline processing in MATLAB.

In order to verify the agreement between the planned and delivered dose, the CC penumbral slopes were confirmed with film dosimetry. Treatments were delivered to coronal films located at the center of the phantom. The slopes were calculated for field widths of 25 and 50 mm and pitch of 0.3. CC penumbral slopes were determined from central longitudinal dose profiles for on/off-axis PTVs from both measured and planned dose distributions.

## **4.3 Results**

### **4.3.1 Penumbral slope**

On/off-axis planned dose profiles along the central axis of each PTV are shown in Figure 4.3 (a) for a 50 mm field delivered at a pitch of 0.3. A large thread effect was seen off-axis. The dose variation pattern described as a 'ripple' is characteristic of HT and results from the helical beam junctioning. This effect has been previously studied in the literature.<sup>55</sup> The complex off-axis dose profiles are a consequence of the beam divergence in the fan beam geometry of HT and the scattering tails that extend deep into near rotations.

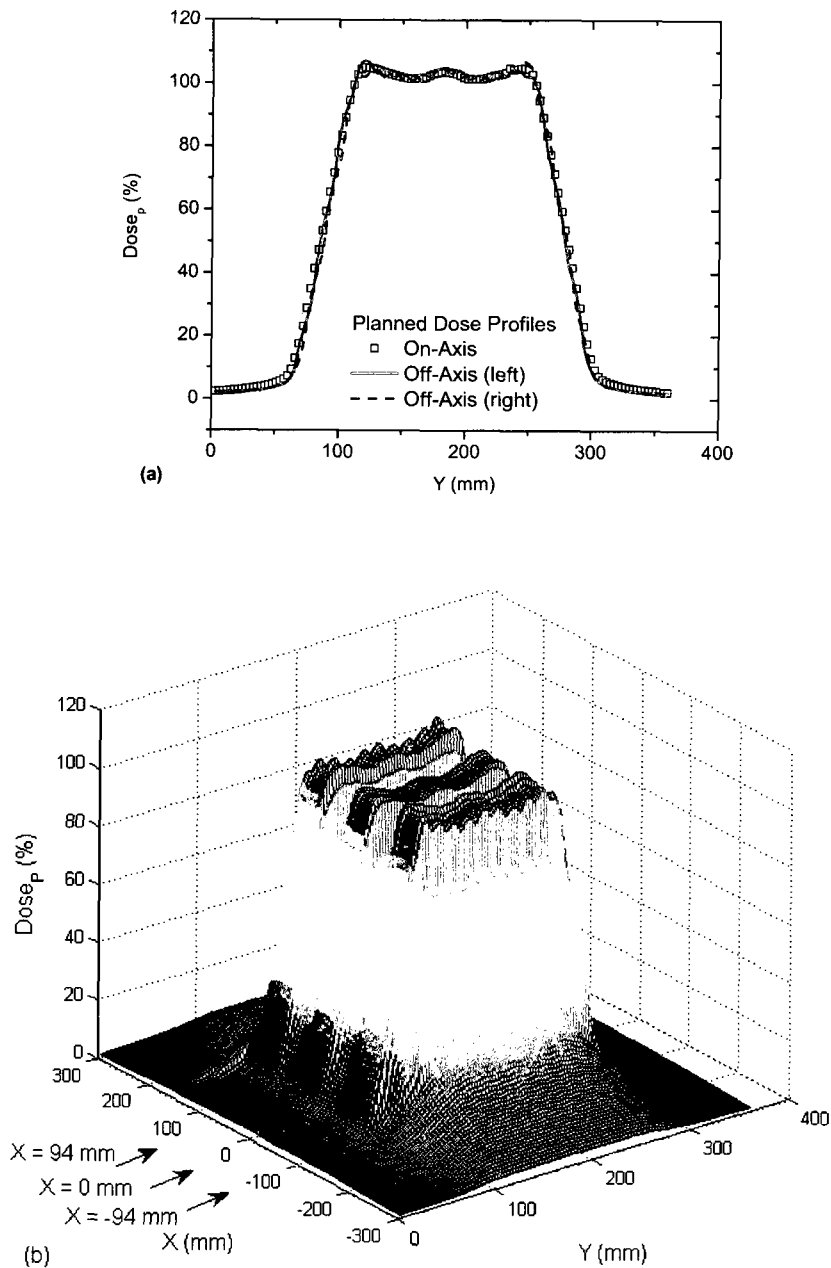


**Figure 4.3** Comparison of on- and off-axis PTVs dose profiles for 50 mm field width for deliveries with a pitch of 0.3 obtained in this study (a). The 3D planned dose distribution is in part (b). The arrows show where the profiles were taken along the Y direction at X of -94 mm (right), 0 mm (on-axis) and +94 mm (left). Z=0

Kissick *et al.*<sup>55</sup> studied the thread effect for different off-axis distances of 0, 3, 5, 7 and 9 cm for continuous rotation at pitch of 1 for an unmodulated beam. The largest ripple was seen at the largest off-axis distance (9 cm). In our study the central axes of the off-axis PTVs were defined at  $\pm 9.4$  cm from the central axis of the machine, and then the large thread effect off-axis seen in Figure 4.3 (a) was expected. The Figure 4.3 (b) shows the planned dose distribution on the central coronal plane ( $Z=0$ ) and where the arrows show where the on/off- axis profiles were taken represented in part (a).

To confirm the TPS dose distributions, the axial profiles from planning were compared to those extracted from coronal film measurements made in the phantom for the same treatment. Typical axial planned and measured dose profiles are shown in Figure 4.4 for 50 mm field width and pitch of 0.3. The profiles were normalized to  $D_p$ .

In addition to beam profiles, CC penumbral slopes were also computed and compared. These results are shown in Table 4.1 for 50 mm field width and in Table 4.2 for 25 mm field width. The reported uncertainties are the parametric error from the fit. The last row on Tables 4.1 and 4.2 gives the percent difference between measured and planned slopes. The agreement between CC penumbral slopes from measurements and planning was better than 5% for all the cases included in this study and the distance to dose agreement was always less than

3 mm. No statistically significant difference between the cranial and caudal gradients was seen.

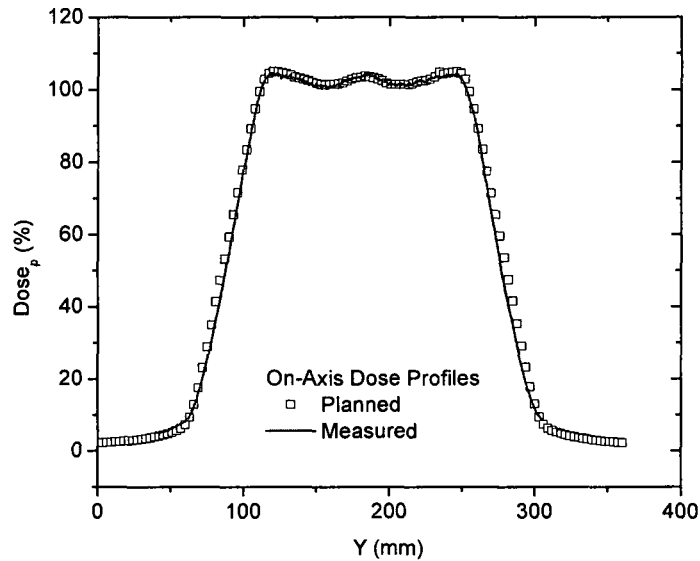


**Figure 4.4** Comparison of on-axis planned and measured dose profiles for 50 mm field width for deliveries with a pitch of 0.3.

#### 4.3.2 Field width, pitch and off-axis distance effects on dose gradients

CC penumbral dose gradients at 50% of  $D_p$  were found to be inversely proportional to the field width ( $\approx D_p \times 100\% / \text{field width}$ ). The dose gradients are shown in Table 4.3. Slightly larger CC gradients were seen off-axis than on-axis. The dose gradients were found to be independent of pitch except as influenced

by the thread effect, which increases with off-axis distance.<sup>55</sup> Gradients were not affected by simultaneously treating 1, 2 or all three PTVs.

**Table 4.1** Planned and measured CC penumbral slopes, on- and off-axis, for 50 mm field width and pitch of 0.3.

Profiles	PTV's Penumbral Slope (Gy/mm)					
	On-Axis (Central)		Off-Axis (Right)		Off-Axis (Left)	
	Cranial	Caudal	Cranial	Caudal	Cranial	Caudal
Planning	0.0798 ±0.0004	0.0794 ±0.0004	0.083 ±0.002	0.084 ±0.002	0.085 ±0.002	0.083 ±0.002
Measurement	0.0795 ±0.0006	0.0793 ±0.0006	0.084 ±0.001	0.0816 ±0.0008	0.0811 ±0.0008	0.083 ±0.001
% Diff	0.4	0.1	1.2	2.9	4.8	0.0

**Table 4.2** Planned and measured CC penumbral slopes, on- and off-axis, for 25 mm field width and pitch of 0.3.

Profiles	PTV's Penumbral Slope (Gy/mm)					
	On-Axis (Central)		Off-Axis (Right)		Off-Axis (Left)	
	Cranial	Caudal	Cranial	Caudal	Cranial	Caudal
Planning	0.151 ±0.003	0.151 ±0.003	0.166 ±0.002	0.165 ±0.003	0.164 ±0.003	0.165 ±0.002
Measurement	0.153 ±0.002	0.154 ±0.002	0.162 ±0.003	0.160 ±0.002	0.161 ±0.003	0.164 ±0.004
% Diff	1.5	1.6	2.2	2.3	2.1	0.7

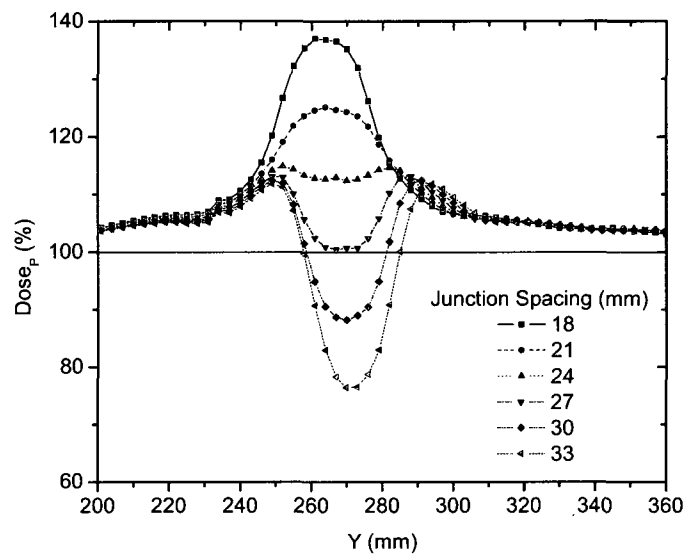
**Table 4.3** On- and off-axis dose gradients at 50% of  $D_p$  for 25 mm and 50 mm fields and pitches of 0.3 and 0.45.

Dose Gradients ( $< \pm 0.1$ %/mm)				
Pitch	0.3		0.45	
Field width (mm)	50	25	50	25
On-axis	2.0	3.8	2.0	3.8
Off-axis				
Right	2.1	4.1	2.1	4.1
Left	2.1	4.1	2.1	4.1

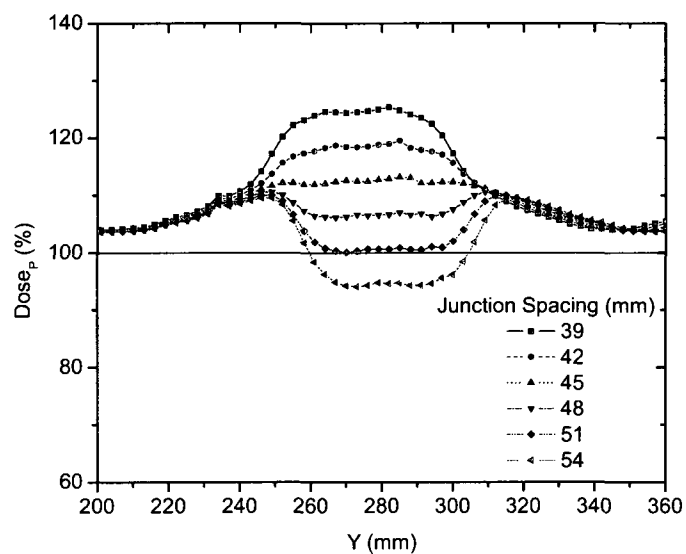
#### 4.3.3 Matching fields of equal width

The best junction uniformity was obtained for fields of equal width. Junctioning of adjacent PTVs treated with a larger field width (e.g., 50 mm) produced more homogeneous junctions than junctions of PTVs treated with smaller field widths (25 mm) as shown in Figure 4.5.

This figure shows the central axis dose profiles across the junction between adjoining PTVs for different JSpac from matching 25 mm fields (a) and 50 mm fields (b). To better illustrate the dose behavior just the section of the profiles within the junction region can be seen in the profile plots.



(a)



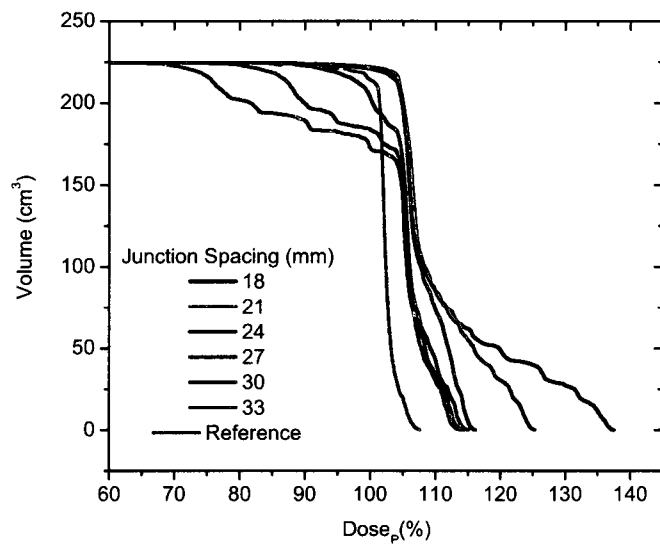
(b)

**Figure 4.5** Comparison of on-axis dose profiles depending on junction spacing resulting from matching fields of equal width of 25 mm (a) or 50 mm (b) for deliveries with a pitch of 0.3.

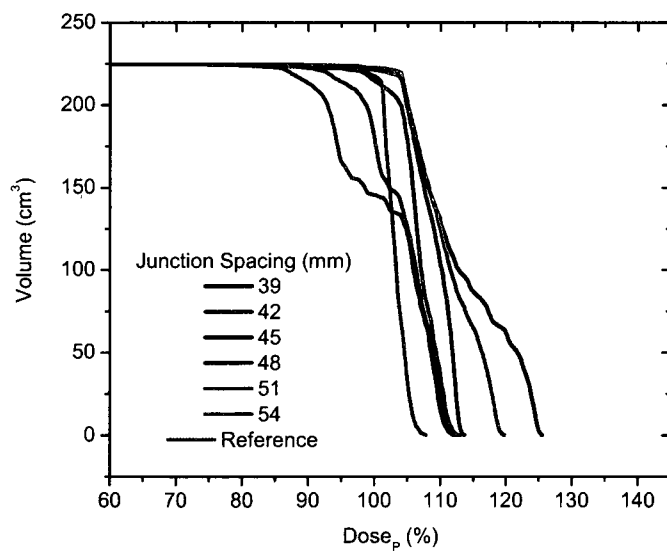
The mean dose, standard deviation (SD), second moment (SM) about  $D_p$  [ $SM = \sum_i (D_i - D_p)^2$ ], minimum (Min) and maximum (Max) doses to the on-axis PTVJ as a function of JSpac are shown in Table 4.4 from matching equal fields of 25 mm or 50 mm. The corresponding values obtained for continuous fields (no junctioning, on-axis PTV) for 25 mm and 50 mm fields are also shown for reference in the last row of Table 4.4. Pitch in the cases shown was 0.3. Figure 4.6 shows the corresponding DVHs for on-axis PTVJ and PTV (reference).

**Table 4.4** On-axis PTVJ mean, SD, Min and Max doses, and SM depending on junction spacing from matching equal fields of 25 mm or 50 mm, and pitch of 0.3.

On-axis PTVJ							
Field Width: 25 mm				Field Width: 50 mm			
JSpac (mm)	Mean/SD (% $D_p$ )	Min-Max (% $D_p$ )	SM ( $Gy^2$ )	JSpac (mm)	Mean/SD (% $D_p$ )	Min-Max (% $D_p$ )	SM ( $Gy^2$ )
18	113 / 10	88-138	.42	39	113 / 7	87-126	.37
21	110 / 7	88-125	.24	42	111 / 5	87-120	.24
24	108 / 4	87-116	.13	45	109 / 3	87-114	.15
27	106 / 5	77-115	.09	48	107 / 3	83-113	.09
30	104 / 8	68-114	.11	51	105 / 5	78-113	.07
33	102 / 11	59-114	.20	54	102 / 7	73-112	.10
Ref	102 / 2	84-107	.02	Ref	103 / 2	85-108	.02



(a)



(b)

**Figure 4.6** DVHs for on-axis PTVJ arising from the matching of equal fields of 25 mm (a) and 50 mm (b) for deliveries with a pitch of 0.3. The references represent the DVH for continuous field (no junction).

Notice that if the DVH curve falls sharply at the prescribed dose or slightly larger, that is an indication that the dose is more homogenous in the junction region, and the treatment is better. If the curve falls gradually beginning at doses lower than the prescribed dose, then the dose is less homogeneous in the junction region and the treatment is worse.

Doses in excess of  $D_p$  were seen in both PTVJs and PTVs. PTVJ average doses, similar to the ones achieved by continuous fields, can be obtained but at the expense of dose homogeneity within the junction as determined by an increase of the SD and SM, with minimum dose reaching as low as 59% and 73% of  $D_p$  for 25 mm and 50 mm fields respectively, as shown in the second last column of Table 4.4.

The optimal  $J_{\text{spac}}$  between adjoining PTVs was determined by finding simultaneously the smallest possible SD, which ensures dose uniformity, and small SM to guarantee doses closer to the prescription. SD is frequently used as a measure of the spread and has been reported as an effective homogeneity index of intensity modulated radiotherapy plans.<sup>56</sup>

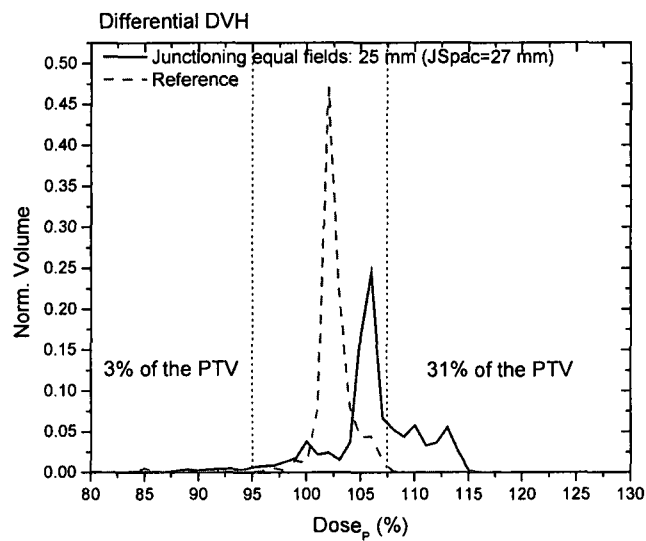
However, SD would be the best estimator if the underlying distribution were normal. Normality is not expected for the dose distribution within the junction in the presence of cold (large  $J_{\text{spac}}$ ) or hot (small  $J_{\text{spac}}$ ) spots (see Figure 4.5), but near the optimal junctioning SD will be a better estimator. Irrespective, the

SD can still be used on a relative basis. SM was also calculated to assess the dose variability about  $D_p$ . In addition, SM was calculated with respect to the prescribed dose. In this case, SM estimates the dose deviation with respect to the prescription within in the junction.

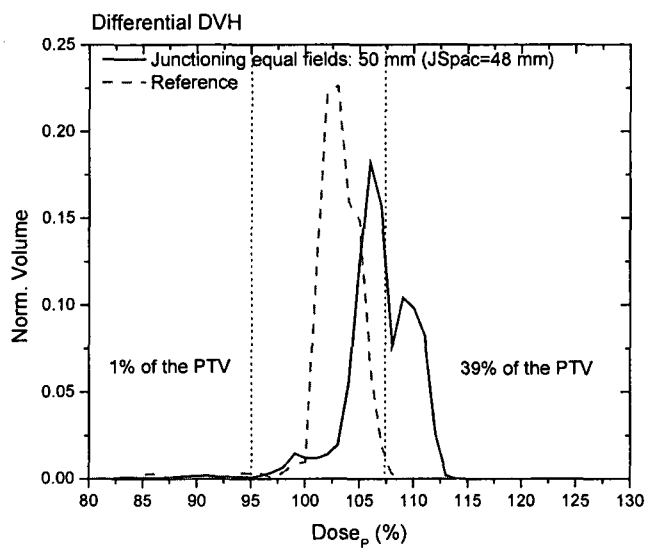
For fields of equal width, the optimal JSpac between adjoining PTVs, defined as described above, was 27 mm and 48 mm for fields of 25 mm and 50 mm respectively. Since no pitch dependence was found and penumbral slope was  $(\approx D_p \times 100\% / \text{field width})$ , the ideal JSpac should be close to the field width for matching fields of equal width.

These optimal junction distances ensured that 95% of the on-axis PTVJ received at least 98% of the  $D_p$  for 25 mm fields and at least 100% of the  $D_p$  for 50 mm fields (optimal junction) for a planned objective of 95% of the PTVs and PTVJs receiving 100% of the  $D_p$ .

Figure 4.7 shows the differential DVH for on-axis PTVJs from matching equal fields of 25 mm (a) and 50 mm (b) for the optimal spacing. The narrowest differential DVH was achieved using equal fields of 50 mm. Here the dose range extended from -17% to +13% of the prescription although only 1% of the on-axis target volume (on-axis PTVJ) received doses lower than 95% of the  $D_p$ .



(a)



(b)

**Figure 4.7** Normalized differential DVHs for on-axis PTVJ arising from the matching of equal fields (optimal JSpac) are represented by solid lines for fields of 25 mm (a) and 50 mm (b) for deliveries with a pitch of 0.3. Corresponding references for on-axis PTV are shown in dashed lines

#### 4.3.4 Matching fields of different widths

Junctioning fields of different widths resulted in a more complex dose distribution than matching fields of equal width. Table 4.5 shows the on-axis PTVJ average doses, SD, SM, Min and Max doses for different JSpac from matching different fields of 25 mm and 50 mm.

**Table 4.5** On-axis PTVJ mean, SD, Min and Max doses, and SM depending on junction spacing from matching different fields of 25 mm and 50 mm, and pitch of 0.3.

On-axis PTVJ			
Fields of 25 and 50 mm			
JSpac (mm)	Mean / SD (% D <sub>P</sub> )	Min-Max (% D <sub>P</sub> )	SM (Gy <sup>2</sup> )
30	112 / 10	84-141	.39
33	110 / 9	80-135	.27
36	107 / 8	74-129	.19
39	105 / 9	68-123	.16
42	103 / 10	63-118	.17
45	101/12	59-115	.22

Figure 4.8 (a) shows the dose profiles along the central axis of the on-axis PTVJ as a function of the JSpac. As can be seen, homogeneous field matching could not be achieved. Unlike matching fields of equal widths, the problem is that the dose gradients grow at different rates for different field widths, and at best the

summed profiles showed two peaks representing a hot and a cold area at the same time. This happens at a JSpac approximately of  $(25\text{mm}+50\text{mm})/2$ . Figure 4.8 (b) shows the reasoning above. The two on-axis profiles for field widths of 25 and 50 mm (black and red curves) are shown and in green the summed profile for JSpac of 36 mm is also included.

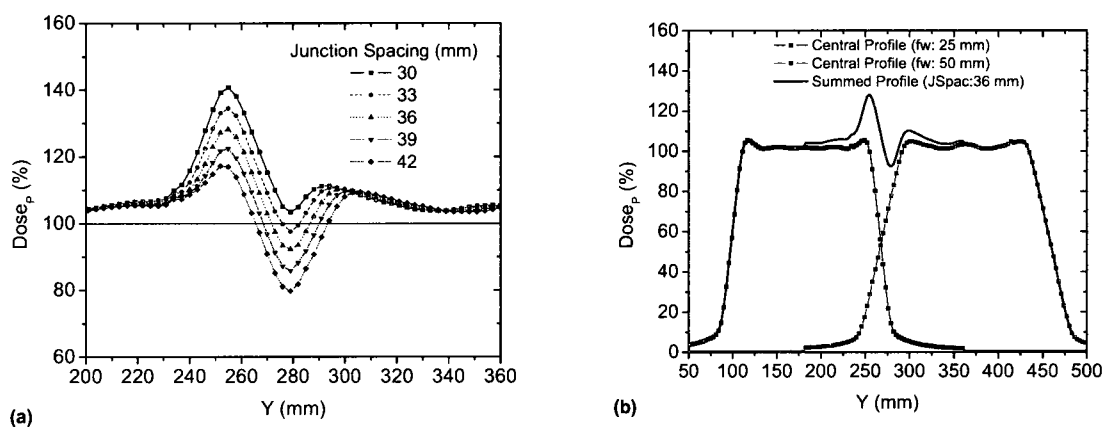


**Figure 4.8** Comparison of on-axis dose profiles depending on junction spacing resulting from matching fields of different widths of 25 mm and 50 mm for deliveries with a pitch of 0.3 (a). Detailed representation of on-axis profiles for fields widths of 25 and 50 mm (black and red curves). In green the summed profile for JSpac of 36 mm is shown.

Figure 4.9 shows the DVH as a function of the JSpac corresponding to the central axis of the on-axis PTV. The minimum volume dose excursion from that prescribed was achieved with a JSpac of about 36 mm at a cost of underdosing by a maximum of 26% and overdosing by 29%.

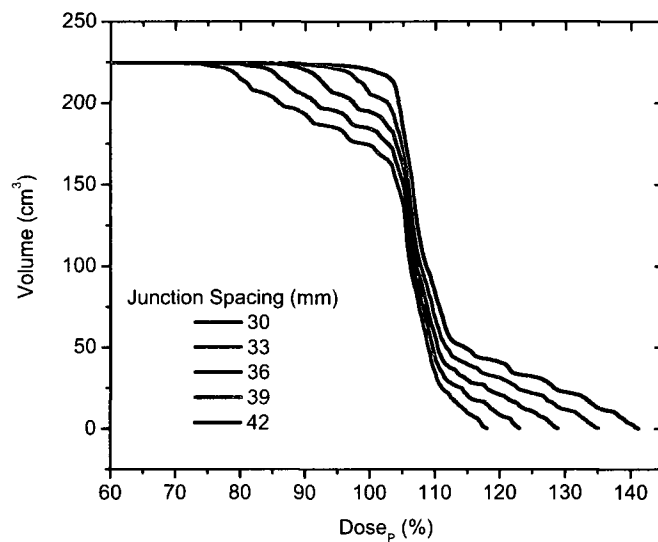


**Figure 4.9** DVHs for on-axis PTVJ arising from the matching of two different fields of 25 mm and 50 mm for deliveries with a pitch of 0.3.

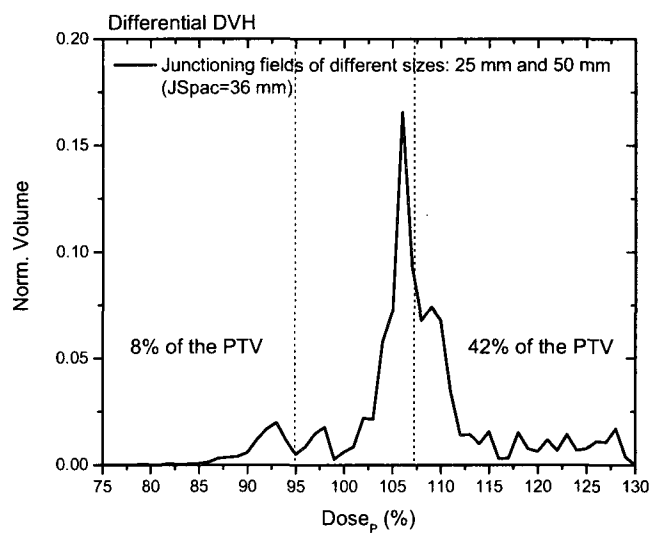


**Figure 4.10** Normalized differential DVH for on-axis PTVJ arising from the matching of different fields of 25 mm and 50 mm (optimal JSpac) for deliveries with a pitch of 0.3.

In this case, 95% of the PTVJ received at least 92% of the  $D_p$ , lower than that obtained for junctions with equal field widths. The normalized differential DVH is shown in Figure 4.10. In this case 8% of the PTVJ received less than 95% of the prescription. More homogeneous dose could be achieved with JSpac of 30 and 33 mm but at the expense of a very high dose area (see red and black curves in Figure 4.9), where more than 130% of the prescribed dose is obtained.

In order to reduce the dose heterogeneity, the PTVs were divided into two or four smaller subPTVs near the junction (only for deliveries with a 25 mm field) with the subPTV prescription dose decreasing toward the junction in such a way as to roughly match the CC dose profile. Simulated profiles based on CC penumbral slopes were first generated to assess the field matching depending on the subPTV dimensions. Figure 4.11 shows examples of the INF end of the PTV simulated profiles for both field widths (25 mm and 50 mm). The stepped dose profiles from breaking the PTVs into smaller subPTVs are also shown.

Dividing each PTV into four multiple contiguous subPTVs with constantly decreasing prescribed dose ( $D_p$ ,  $3/4D_p$ ,  $1/2D_p$ ,  $1/4D_p$ ) allowed PTV matching with dose homogeneity similar to junctioning PTVs of equal CC slope. 95% of the PTV received at least 101% of the  $D_p$ , with dose excursions of -19% to +13% from prescription (1% of the PTV received less than 95% of  $D_p$ ).

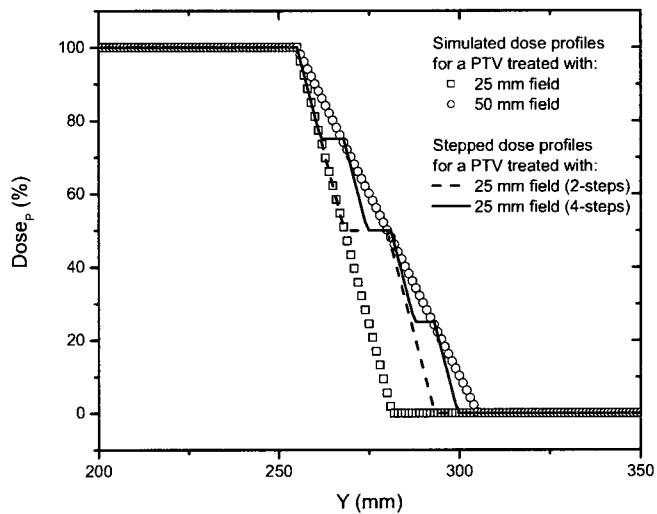


**Figure 4.11** INF end of the PTV simulated profiles for field widths of 25 mm and 50 mm, and the simulated stepped dose profiles from breaking the PTVs into smaller subPTVs for deliveries with 25 mm field width.

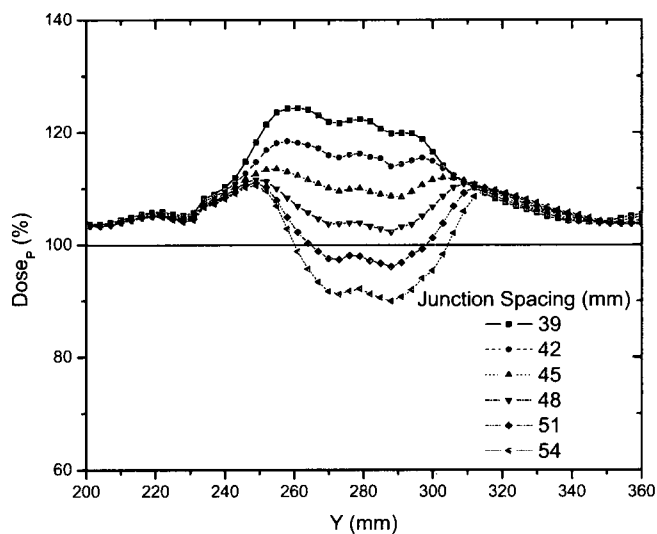


**Figure 4.12** Comparison of on-axis dose profiles depending on junction spacing resulting from matching fields of different widths of 25 mm (4-steps) and 50 mm for deliveries with a pitch of 0.3.

Summed dose profiles from matching PTVs with fields of different widths of 25 mm (4-steps) and 50 mm depending on junction spacing are shown in Figure 4.12. The corresponding DVHs are seen in Figure 4.13. The DVH in blue for JSpac of 48 mm shows that homogeneous dose in the junction is achieved without excessive overdosing.

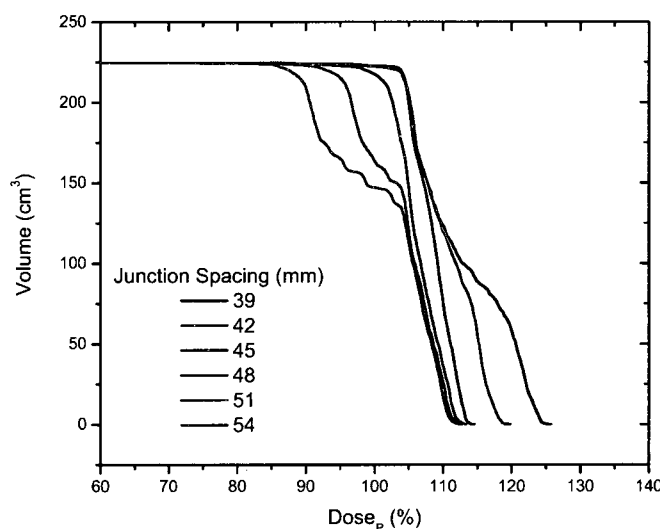


**Figure 4.13** DVHs for on-axis PTVJ arising from the matching of two different fields of 25 mm (4-steps) and 50 mm for deliveries with a pitch of 0.3.

For comparison, the isodose curves for three different cases are shown in Figure 4.14: matching of equal fields of 50 mm width (a), different fields of 25 mm and 50mm (b), and different fields of 25 mm (4-steps) and 50mm (c). In each case, the figures represent the dose distribution arising from optimal inter-PTV spacing (JSpac) corresponding to 48 mm (a), 36 mm (b) and 48 mm (c) respectively. The

dose distributions obtained in (c) from matching fields of different widths are very similar to the ones seen in (a), since the dose gradients for the 25 mm field were smoothed to agree with the 50 mm field dose gradients.

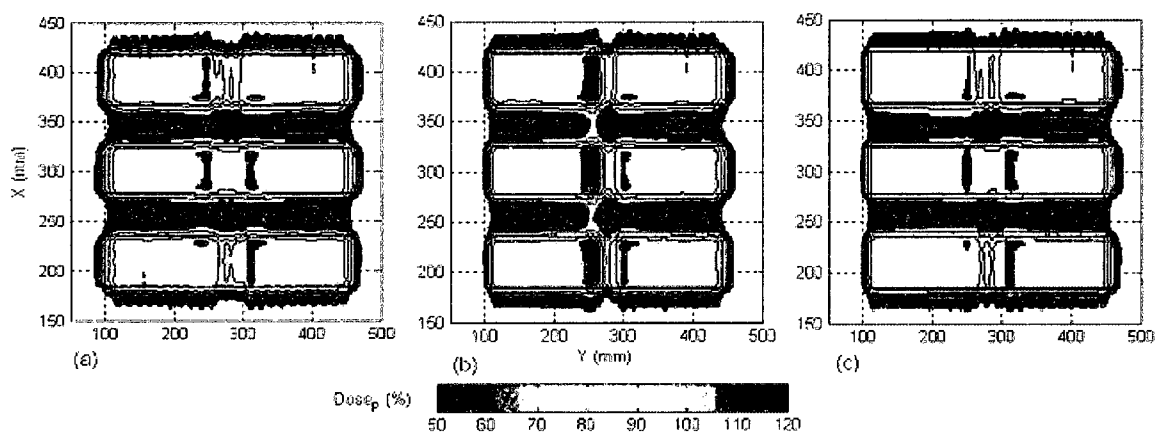


**Figure 4.14** Isodose maps from the matching of equal fields of 50 mm width (a), different fields of 25 mm and 50mm (b), and different fields of 25 mm (4-steps) and 50mm (c). The figures represent the dose distribution for the optimal JSpac corresponding to 48 mm (a), 36 mm (b) and 48 mm (c) respectively.

The junction dose distributions were validated experimentally using film dosimetry. For the cases of optimal JSpac shown above, a maximum difference between calculated and measured of 3.9% anywhere in the junction region was found.

### 4.3.5 Pitch and on/off-axis dependences

No strong pitch dependence was observed from field matching for the pitches used with the exception that the off-axis thread effect was of higher amplitude for larger pitch. The largest thread ripple was observed for a 50 mm field with a pitch of 0.45. Figure 4.15 shows the off-axis dose profiles along the central axis of the right PTVJ from matching fields of 50 mm and pitches of 0.3 and 0.45 (JSpac of 45 mm and 48 mm). There are slight differences between on- and off-axis results due to the small variations of the penumbral dose gradients off-axis (Table 4.3) and the overlaying thread effect.

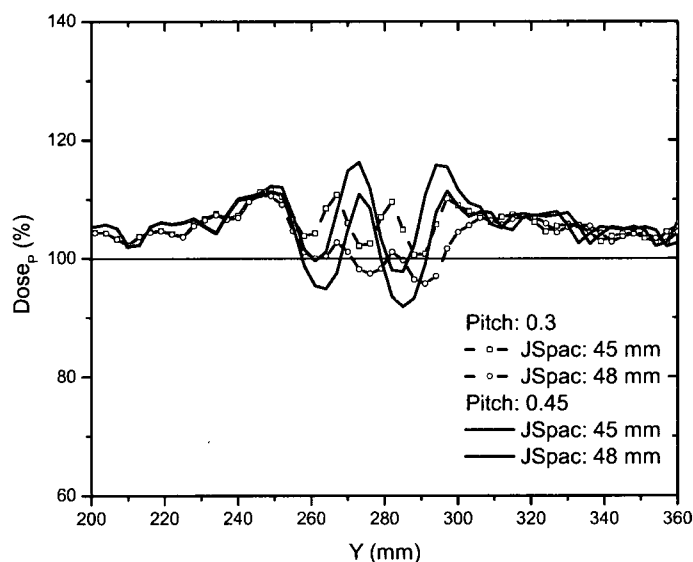


**Figure 4.15** Off-axis threading effect from junctioning two equal 50 mm width fields for pitches of 0.3 and 0.45, and JSpac of 45 mm and 48 mm (profiles along the central axis of the right PTVJ).

## 4.4 Discussion

In this work we examined field matching with HT. Experiments were based on planning studies after the predicted dose distributions of individual fields were verified by film and ion chamber dosimetry. Agreement between measurement and planned CC penumbral slopes was better than 5%, which is quite reasonable since this is a high dose gradient region and dosimetric accuracy of Kodak EDR2 films based on the optical density standard deviation ranges from 7% to 15% of their average values.<sup>57</sup>

The CC penumbral slope was found to be  $(\approx D_p \times 100\% / \text{field width})$  and gradients were not affected by simultaneously treating one, two or all three PTVs. Thus, penumbral dose gradients at 50% of  $D_p$  were inversely proportional to the field width and did not depend on the pitch as shown in Table 4.3. This could be verified with a simple theoretical calculation of the longitudinal dose profiles along the central axis based on a one-dimensional convolution of an ideal slit beam dose profile and an ideal beam intensity distribution.<sup>58</sup> Figure 4.16 (a) shows this example. For unity pitch the ideal longitudinal profile could be described as a triangular function.<sup>55, 58</sup> Pitch is defined as the ratio of the distance that the couch moves per gantry rotation divided by the field width (5 cm in Figure 4.16). Then, the longitudinal profile after the first rotation could be represented as the curve in black, with the following rotations represented in different colours; 2nd in red, 3<sup>rd</sup>

in green, 4<sup>th</sup> in blue and 5<sup>th</sup> in cyan. From the superposition of all these profiles the total dose along the longitudinal profile is represented by the pink line, where the initial and final slopes are  $\sim D_p/f_w$ . Similar analysis can be performed for other pitches as well.

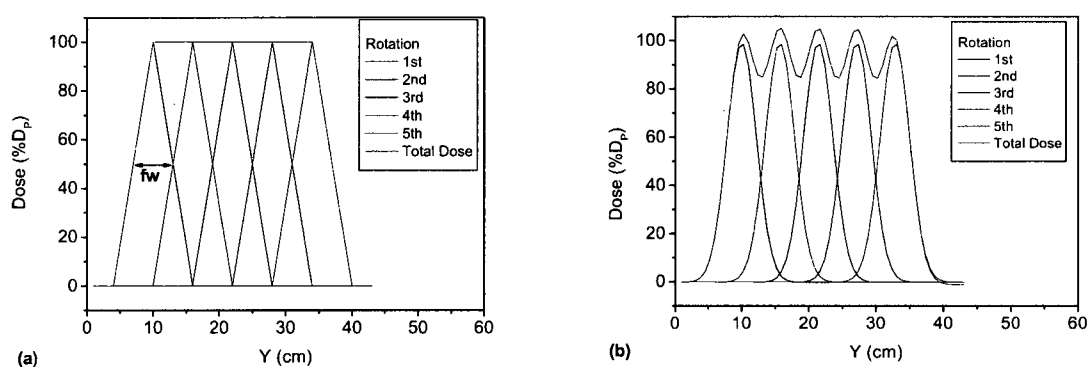


**Figure 4.16.** (a) On-axis longitudinal dose profiles for few ideal rotations for a unity pitch are represented in different colours (1<sup>st</sup> in black, 2<sup>nd</sup> in red, 3<sup>rd</sup> in green, 4<sup>th</sup> in blue and 5<sup>th</sup> in cyan). The total dose is also represented in pink. (b) Similar but real profiles are schematically represented. The thread effect can be seen when single-rotation profiles differ from the ideal triangular shape.

Slightly larger CC penumbral gradients were seen off-axis than on-axis. This is related to the beam divergence and it is a result of the same phenomenon that produces thread effect in helical tomotherapy. In off-axis profiles, dose gradients grow faster than on-axis. For instance, an ideal single rotation on-axis longitudinal dose profile for a unity pitch is similar to a triangular function.<sup>55, 58</sup> However, off-axis profiles differ from a triangular shape and the gradients grow faster than linear as previously reported.<sup>55</sup> Similar behaviour is expected for

smaller pitches as well. The actual field strength delivered by each of the beams varies with the distance to the source. For on-axis profiles this distance is kept constant during the whole rotation. For off-axis profiles this distance varies making the field intensity lower (intensity $\sim 1/r^2$ ) when the source is on the far side or making the field width smaller when on the closer side. This is schematically presented in Figure 4.16 (b). Thread effect can be seen when single-rotation profiles differ from the ideal triangular shape producing the ripple pattern seen in the figure (scales are arbitrary).

In the junction region, better homogeneity was obtained for fields of equal width with larger fields being better than smaller fields as seen in Figure 4.6. Even though junction errors are smaller with larger field widths, there is always an optimal JSpac, which allows a satisfactory dose distribution within the junction even for small fields.

Optimal junction spacing was found to be field width dependent being larger for larger fields because of the smaller penumbral dose gradients. The optimal JSpac could be slightly reduced at a cost of increasing the dose to the PTVJs; however, this will increase the minimum dose within the junction.

Junctioning fields of different widths proved to be more problematic. Figures 4.8, 4.9 and 4.14 (b) show that doses spread within a wider range and homogeneous field matching could not be achieved. However, the dose inhomogeneity resulting

from junctioning fields of different widths was reduced by breaking PTVs into multiple contiguous PTVs with a modified prescription near the junction to feather the effective junctioning region (see Figures 4.12, 4.13 and 4.14). Nevertheless, even with the most uniform junction, doses in excess of the prescribed dose were obtained; the average doses to the adjoined PTVs were 4% higher than the average dose obtained using a single continuous field (PTV).

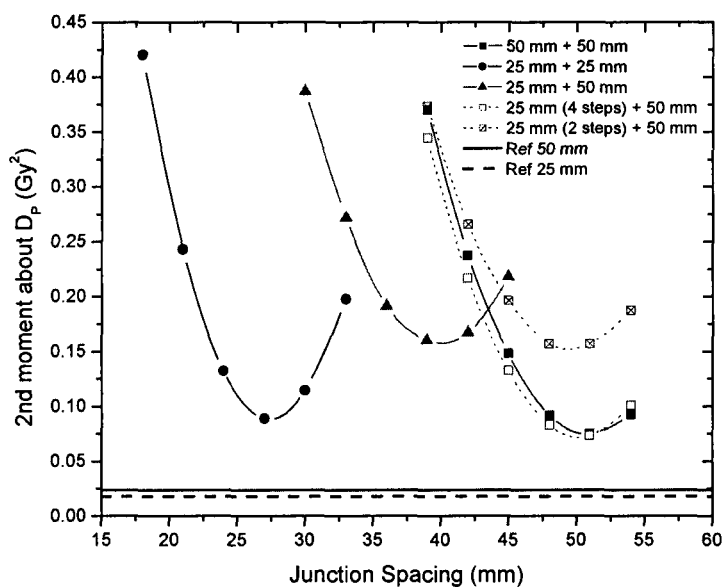


**Figure 4.17** Dose second moments about  $D_p$  as a function of the JSpac for on-axis PTVJ from junctioning equal fields of 50 mm and 25 mm and different fields of 25 mm and 50 mm.

The influence of field width and PTV spacing on the dose in the junction region is summarized in Figure 4.17. How widely the dose is spread about the  $D_p$  is

measured by dose second moments, which reach a minimum where the deviations are smaller. It also shows how breaking the PTV into a smaller subPTVs to feather the effective junction region results in inhomogeneities associated with matching fields of different widths being reduced.

Even though 10 mm fields were not included in this paper, similar reasoning could be applied and an ideal Jspac could be found. Since the penumbral slope would be steeper for 10 mm fields than for 25 or 50 mm fields, a narrower junction region would be obtained.

The objective of this study was to develop methods of producing as homogeneous a dose as possible across a region consisting of multiple contiguous PTVs although some heterogeneity is normally accepted even in the absence of field junctions. Figures 4.7 and 4.10 showed the differential DVHs for on-axis PTVJs and referential PTVs from matching fields of equal or different widths. The dotted vertical lines enclose the range of dose heterogeneity (-5% and +7% of the prescribed dose) as recommended in the ICRU Report.<sup>59</sup> The narrowest differential DVH was achieved using equal fields of 50 mm as shown in Figure 4.7 (b). Here the dose range extended from -17% to +13% of the prescription although only 1% of the on-axis target volume (on-axis PTVJ) received doses lower than 95% of the  $D_p$ . However, 39% of the PTVJ received more than 107% of the  $D_p$ . This deviation from prescription is larger than the 10% reported by other authors.<sup>60</sup>

The pitch had minimal effect on junction dose distributions with the exception that the off-axis thread effect was of higher amplitude for larger pitch (Figure 4.15). However, this effect can be reduced if specific pitch values are used as recommended in a recent study.<sup>55</sup> There were slight differences between on-axis and off-axis results due to the small variations of the penumbral dose gradients off-axis (Table 4.3) and the overlaying thread effect.

The results presented here have limitations and extrapolation to the clinic must be done with caution. For example, the specific numeric values are valid only in unit density material (water). The principle is valid for all biological materials, but the magnitudes will vary depending on the penumbra, which itself is a function of electron transport in the media and media density. Further, we did not constrain the dose in the SUP-INF direction as one might do with an organ at risk longitudinally adjacent to the PTV. Thus, in the case of hard constraint optimizations,<sup>61</sup> the concept presented here remains valid, but specific values for optimal JSpac need further investigation.

In spite of its simplicity, this phantom study addresses the principal dosimetric issues, which arise when matching two different longitudinally adjacent treatment volumes to form a contiguous treated volume, as might occur when junctioning a recurrence (or new lesion) PTV to a previously treated PTV. Another instance of clinical importance where we see this is when breaking a contiguous PTV into two regions to allow one region to be treated with a small field to gain better

PTV/OAR conformance and the second region to be treated with a larger treatment field to reduce the overall treatment time. A clinical example of where this might be useful is total marrow irradiation. In summary, this study describes the dosimetric challenges that arise when junctioning adjacent PTVs and examines clinically viable solutions.

# **Chapter 5**

## **Optimum frequency of spatial registration in image guided radiation therapy for TMI**

### **5.1 Introduction**

Imaging has played an important role in radiation therapy. This includes diagnosis, patient data acquisition, delineation of target regions and organs at risk, treatment planning, patient setup and alignment prior to treatment delivery, treatment quality assurance, and assessment or follow-up of the treatment response. However, IGRT is a term commonly used in the context of inter- and intrafractional patient anatomic and setup variations and is mainly focused on treatment planning and delivery.<sup>62</sup>

Significant variations in shapes and position of treatment targets and surrounding normal tissues have been found in recent studies. Respiratory motion, weight loss, organ motion and tumour shrinkage are only a few examples of such variations, which have an important influence in the treatment response.<sup>62-66</sup>

It is current practice to add margins to the clinical target volume (CTV) yielding the planning target volume (PTV) to account for some of the variations described above. However, surrounding normal tissues can still receive dose, which limits the ability of this technique to deliver higher dose to the tumour without increasing normal tissue toxicity. In addition, there are cases where even using margins, there is a probability of missing marginal target volumes, a situation that may be aggravated with the tight margins common in IMRT.<sup>67-69</sup>

HT is an image guidance technology that integrates a linear accelerator specially designed to deliver highly conformal dose distributions, and a helical MV CT scanner. CT images taken immediately before treatment are used to position the patient and for spatial alignment of the target volume and organs at risk with the planned radiation beams.<sup>13, 14</sup>

This chapter focuses on the spatial image guidance frequency in an attempt to reduce intrafractional variations in a TMI treatment. In TMI the target volume is defined by the entire bony skeleton and the main limitation is treating the large volumes of bone marrow without excessive normal tissue complications, such as

lung and kidney toxicity. The duration of a TMI treatment and the large target volume increase the intrafractional spatial variations discussed above.

An optimal delivery of a very conformal dose distribution requires precise patient positioning. The HT technique allows patient alignment and repeatability by imaging the patient once, prior to each treatment fraction; this procedure is called spatial registration. The daily image is compared to a reference image taken at the time of treatment planning. Image fusion to bony landmarks or manual adjustment by the radiation therapist determines the set of x,y,z translations required to bring the patient position into alignment with the reference image. These linear translations are then applied to the patient position using automatic treatment table shifts.

This approach ignores patient rotations relative to the reference image, which is a reasonable approximation close to the site of the match, but causes increasing uncertainty as we move away from the alignment site. In addition, given the fact that the human body cannot be considered as a rigid body, and also that a usual TMI treatment fraction is long (allowing time for patient and organ motion) and spatially large in the longitudinal direction (Y-axis); the positioning uncertainty increases as the treatment moves further from the alignment position. In order to account for the increasing uncertainties we propose that an increase in the margins should be applied to ensure that the target is covered. There are two different causes of the increased error during the treatment. First, if the patient

has been aligned in a single specific region of the patient's body (which is less than ideal), as we move further from that position the uncertainty increases. Second, even if the patient as whole has been successfully aligned and registered, in time the initial patient registration would be inaccurate since the patient and organs within the patient could move.

In this chapter, an analysis was conducted of the benefits of repeatedly positioning the patient and realigning the target volume with the planned beams within a treatment fraction to correct for intrafractional variations in patient setup and anatomy. This can be implemented for TMI by spatially dividing or splitting the treatment fraction into two or more sub-treatments along the longitudinal direction. This technique allows superior patient alignment by imaging the patient several times during one treatment fraction resulting in greater confidence in patient setup and treatment delivery. This advantage adds to the previously discussed examples in Chapter 3 and 4, where splitting the TMI treatments into at least two sub-treatments may be necessary or beneficial. In Chapter 3 the benefits of using different SUP-INF spatial resolution for adjacent PTVs were presented. Breaking the PTV into two different treatment volumes allows treating one region with smaller field width to gain a better OAR/PTV conformance while treating the second region with a larger field width reducing the overall treatment time. The second example, discussed in Chapter 4, is when the PTV length exceeds the bed travel distance two separate longitudinally adjacent PTVs must be planned and treated to form a contiguous volume.

## **5.2 Materials and methods**

### **5.2.1 Geometry and setup**

The same elliptical pseudo anthropomorphic homogeneous phantom seen in Chapter 4 was used in this study. Within the phantom, left and right ribs and the spine were defined to form the CTV. Left and right lungs were also defined as the only organs at risk (OAR) to represent the most important normal tissue structures in TMI. To simulate the increasing uncertainty along the longitudinal direction (Y-axis) generated from moving further from the position where the patient alignment has been performed prior to the treatment delivery, linearly increasing margins were added to expand the CTV and OARs. This increasing planning treatment volume and organ at risk are referred to as iPTV and iPRV.

In order to assess the influence of the frequency of spatial registration, different cases were investigated. First, one treatment per fraction was only assumed, which corresponds to one patient alignment and setup error correction at the beginning of each treatment fraction. For example, a set of x,y,z linear shifts are applied to bring the bony anatomy near isocentre, as imaged immediately prior to treatment, into alignment with the bony anatomy near isocentre as defined in the treatment planning CT. In the tomotherapy unit the alignment is performed through a few steps. First, prior to the scan the red lasers are automatically positioned based on the planned setup position. Once the patient is on the couch, the system automatically allows moving the couch to the planned setup

position. If needed, the patient's CT fiducials and lasers can be used to achieve the initial setup position. The patient is scanned and a "Tomolmage" is acquired. The procedure of aligning the Tomolmage and the reference image used during the treatment planning is called Tomolmage registration. The system shows the planning and the Tomolmage volumes as seen in the transversal (a) and sagittal (b) views in Figure 5.1. The figures shows in blue the Tomolmage, taken just prior to the treatment and in grey is the planning image. In the example shown in Figure 5.1, the misalignment between both images can be clearly seen.



**Figure 5.1** Transversal (a) and sagittal (b) views of the patient's Tomolmage (blue) and the planning image (grey).

The alignment is performed by either manual or automatic registration, which is implemented through translational and rotational adjustments. The Figure 5.2 shows the registration tab of the TomoTherapy System. On the right panel of the figure, the lateral, longitudinal and vertical shifts as well as the rotational adjustments can be seen.



**Figure 5.2** Register tab of the TomoTherapy System.

The initial case analyzed corresponded to one patient alignment and setup error correction at the beginning of each treatment fraction. This implies that further we move from the alignment position, the more the PTV margins have to be increased to account for the increasing positioning uncertainty. The analysis was performed for a maximum margin increase of 5 mm, 10 mm and 15 mm from the original margin of the CTV and OARs. For instance, Figure 5.3 (a) shows a scheme of the linearly increased margin. In the figure, a lung is represented as a cylinder along the Y-axis. The OAR's margins linearly increase until the final margin of 15 mm is achieved. The total length of the structures in the longitudinal

direction was kept constant and equal to 23.4 cm for both iPTV and iPRV in all cases studied. Therefore, the angle between the edges of the margins and the structures along the Y-axis decreases for maximum margins of 5 mm and 10 mm compared to the 15 mm margin as seen in Figure 5.3 (b).

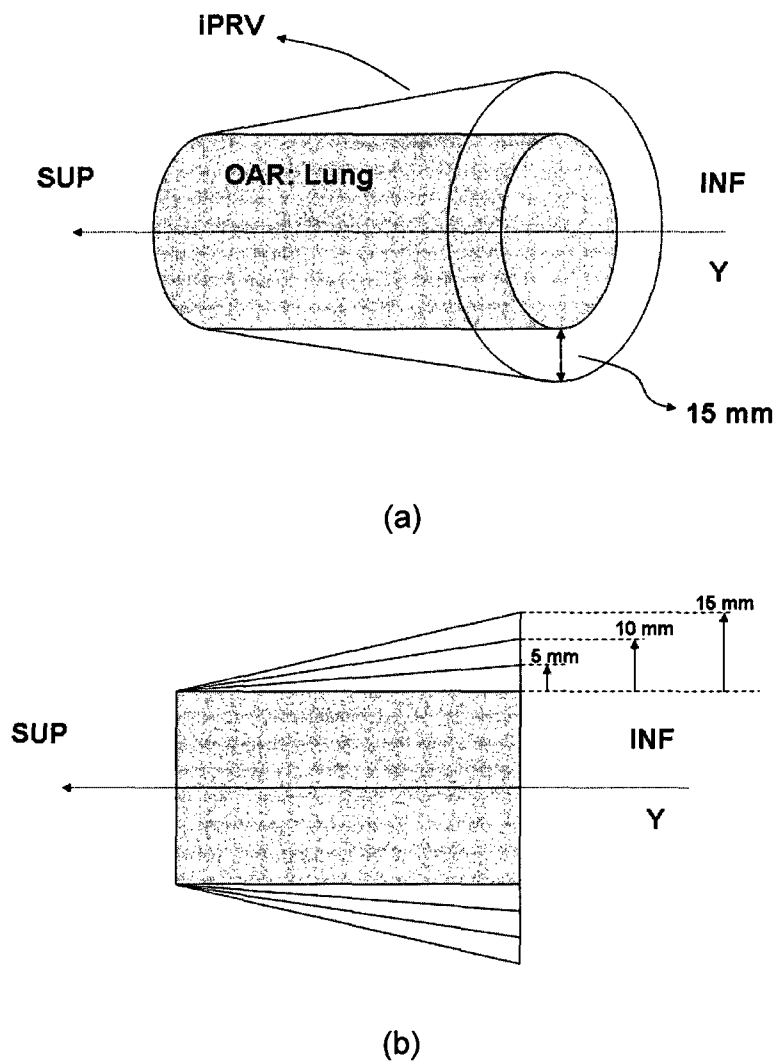


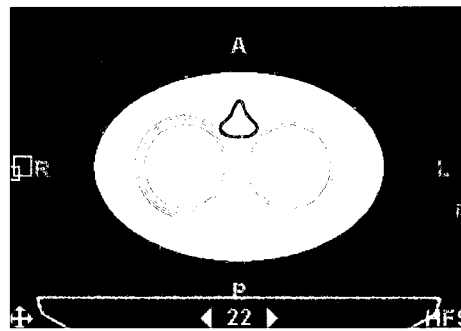
**Figure 5.3** Scheme representing a plane view of the increasing margin along Y-axis for a simulated cylindrical OAR (Lung) (a). Comparison of the increasing margins for different maximum margin of 5 mm, 10 mm and 15 mm at the INF extreme of the structure (b).

Even though the terms CTV and OARs were used to refer to the original structures, these terms are equivalent to the usual PTV and PRV obtained from GTV and OAR expansions with internal and setup margins. These terms were used for the sake of clarity to distinguish between these original structures and the new increasing boundaries established to define the increasing uncertainty along the longitudinal direction.

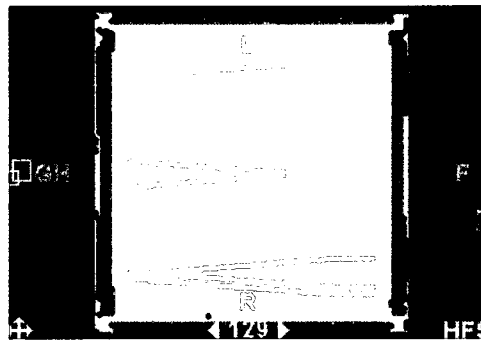
Figure 5.4 (a) shows the axial view of the actual simulated structures in this study. The circles in pink represent the lungs, the structures in dark green and yellow are the ribs and in the centre in blue is the spine. Each subsequent slice in the SUP-INF direction had a linearly increasing margin. Figure 5.4 (b) and (c) show the coronal and sagittal views of the phantom and the iPTV and iPRV. The figures show the increasing margins along the Y-axis in the SUP-INF direction.

The next step was to split the treatment along the longitudinal direction into two or three independent sub-treatments. This technique allows verifying and realigning the patient's position several times during each treatment fraction. Figure 5.5 shows the scheme of this procedure. In the figure, the lung and the increasing margins representing the iPRV for the three cases can be seen: a) no splitting the treatment (no-junction); b) splitting the treatment into two (one-junction); and c) three sub-treatments (two-junctions). The figure represents the case when the margin reaches 15 mm at the end of the structures on the INF

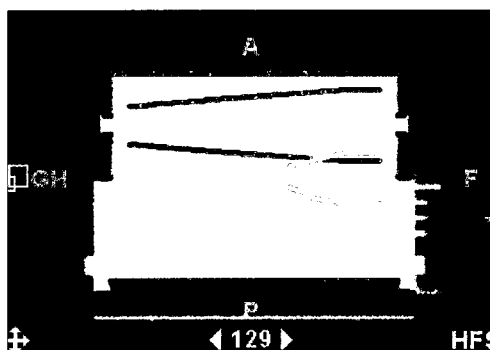
side for the unsplit treatment, but maximum values of the margins of 5 mm and 10 mm were also examined as was mentioned before.



(a)



(b)



(c)

**Figure 5.4** Axial (a), coronal (b) and sagittal (c) views of the phantom, iPTVs and iPRVs. Maximum margin of 15 mm. The circles in pink represent the lungs, the structures in dark green and yellow are the ribs and in the centre in blue is the spine. The linearly increasing margin of the iPTVs and iPRVs can be seen on the coronal and sagittal views.

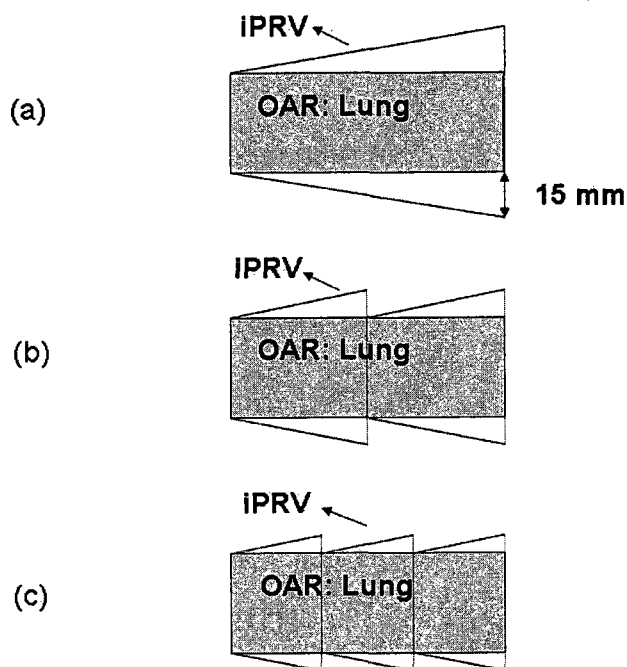


**Figure 5.5** The increasing margins representing the iPRV for a lung for three cases: no-junction (a), one-junction (b) and two-junctions (c). The figures represent the case of a maximum margin of 15 mm

### 5.2.2 Treatment planning procedure

The same CT phantom images taken on a Philips Brilliance CT-Simulator at 120 KV, as in Chapter 4, were used. A total of 120 slices, 3 mm thick, were acquired. The contours were outlined on PINNACLE<sup>3</sup> version 7.6c planning station and exported to the TomoTherapy Planning Station (TPS). The prescription was 20 Gy with 95% of the iPTV to receive the prescribed dose ( $D_p$ ). The maximum dose

permitted to the iPRV was 8 Gy. Field widths of 25 and 50 mm at pitch of 0.287 were examined. The other parameters of the planning process including importance, maximum and minimum doses, DVH dose and penalties were kept constant for all experiments.

The 3D dose matrixes calculated by the TPS and the vectors defining the iPTV and iPRV structures were then exported for offline processing in MATLAB. To represent the split treatments, the unsplit 3D dose matrix such as in the case shown in Figure 5.5 (a) was divided into two or three equal sections and junctioned with the first section two or three times. The result is schematically shown in Figure 5.5 (b) and (c).

### **5.2.3 Radiobiological assessment**

In this phantom study, ribs and spine were defined as the CTV and lungs as OAR to simulate a TMI treatment as explained previously. The radiobiological assessment of the influence of the image-guided spatial frequency was performed using TCP and NTCP models.

Tumour control was evaluated using the two-parameter Poisson model described in Chapter 2. More specifically, Equation 3.4 from Chapter 3 was used, which is an application for inhomogeneous dose distribution. The TCP parameters used

[ $D_{50} = 23\text{Gy}$  (95%CI: 19, 27) and  $\gamma_{50} = 1.2\%/%$  (95%CI: 0.8, 2)] were obtained from the previous work described in Chapter 2.

The assessment of treatment-related normal tissue toxicities was based on the Lyman NTCP model described in Chapter 3 (Equations 3.1, 3.2 and 3.3).

The parameters characterizing NTCP for lungs were obtained from the results published by Burman *et al.* from fitting the tolerance data for many organs compiled by Emami *et al.* The specific values of the NTCP parameters for lungs were shown in Table 3.1.

The radiobiological evaluation of the image-guided spatial frequency was performed for the unsplit treatment and two- and three-sub-treatments corresponding to no-junction, one- junction and two-junctions respectively. The results for different maximum margins of 5 mm, 10 mm and 15 mm; and different field widths of 25 mm and 50 mm were also compared.

### **5.3 Results**

A comparison of the iPTV and iPRV's DVHs between no- junction, one- junction and two-junctions are shown in Figure 5.4 for maximum margin of 10 mm and field width of 50 mm.

The doses for 80%, 50%, 20% and 10% of the volume of the iPRV from 20 Gy treatment plan for the cases of no-junction, one-junction and two-junctions are in Table 5.1. The table shows the values obtained for a maximum margin of 10 mm and field size of 50 mm as an example.

Figure 5.6 and also showed the sparing effect of splitting the treatment into two or three sub-treatments. The difference in the doses received by the iPRV between no-junction and two-junctions was smaller for larger volumes and vice versa. For instance, the dose to 20% of the lungs,  $D_{20}$ , for two-junction case was up to 64.2% smaller compared to unsplit treatment (no-junction). This difference was only of 16.7% for  $D_{80}$ .

**Table 5.1**  $D_{80}$ ,  $D_{50}$ ,  $D_{20}$  and  $D_{10}$  of 20 Gy plan for iPRV with a maximum margin of 10 mm and 50 mm field for the cases of no-junction, one-junction and two-junctions.

Dose (Gy)	No-Junction	One-Junction	Two-Junctions
$D_{80}$	7.7	6.9	6.6
$D_{50}$	11.2	9.2	8.5
$D_{20}$	22.0	16.2	13.4
$D_{10}$	23.7	20.8	18.4

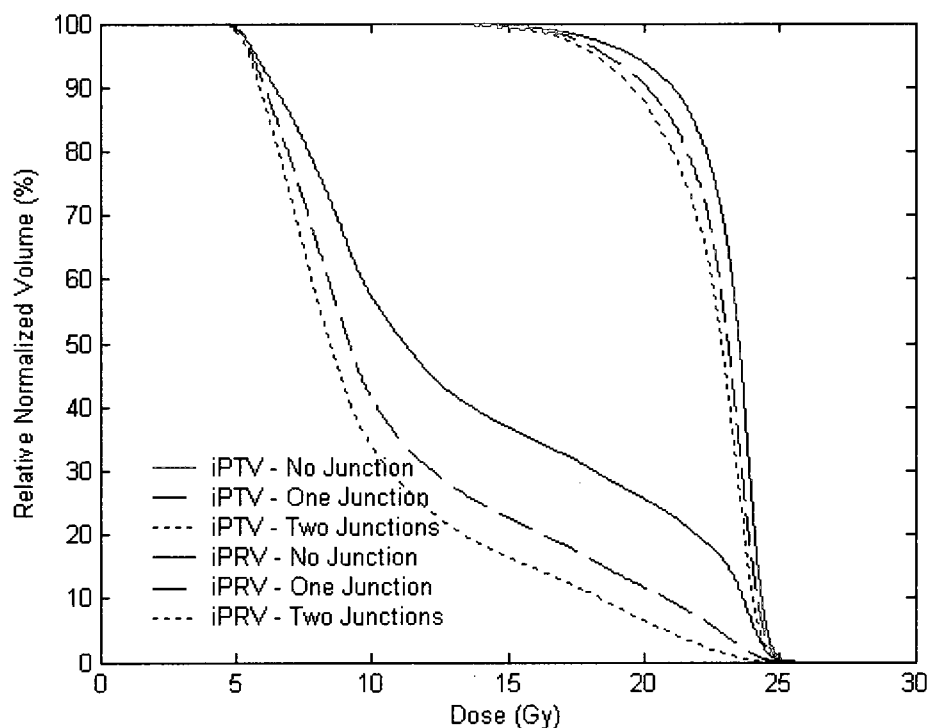


**Figure 5.6** Comparison of the iPTV and iPRV's DVHs between no-junction, one-junction and two-junctions for maximum margin of 10 mm and field width of 50 mm.

Even though there was an ostensible dose reduction to the iPRV, the dose received by the iPTV also decreased when the treatment was split as seen in the DVHs in Figure 5.4. For example, the volume of the iPTV receiving 20 Gy was 93.9%, 90.5% and 88.4% for no-junction, one-junction and two-junction cases respectively.

Figure 5.7 shows the TCP values for 50 mm field width and maximum margins of 5 mm, 10 mm and 15 mm. The figure compares the curves between no-junction, one-junction and two-junctions. Similarly, Figure 5.8 shows the NTCP values for

50 mm field width and maximum margins of 5 mm, 10 mm and 15 mm; and compares no-junction, one-junction and two-junction curves. Tables 5.2, 5.3 and 5.4 show the numerical estimates of TCP and NTCP not just for a treatment with 50 mm field, but also 25 mm field width.

TCP estimates are less affected by the treatment splitting procedure than NTCP estimates. The difference of TCP values between no-junction and two-junction treatments were only 4%, 3% and 2% for a maximum margin of 5 mm, 10 mm and 15 mm respectively (field width of 50 mm).

In contrast to the TCP, the choice of maximum margin strongly affected the NTCP estimates for the no-junction case as seen in Figure 5.8 in solid lines. Less dependence on the maximum margin used was seen for one junction and two- junction cases as seen in also in Figure 5.7 in dashed and dotted lines. The toxicity based on NTCP model was up to 29% lower for two-junction treatment compared to unsplit treatment for a maximum margin of 15 mm. Equivalent values for 5 mm and 10 mm of maximum margin were 1.7% and 11%, respectively. The values represent a treatment with a field of 50 mm.

There was no substantial difference between TCP using 25 mm or 50 mm field width, nor between NTCP values as seen in Tables 5.2, 5.3 and 5.4.

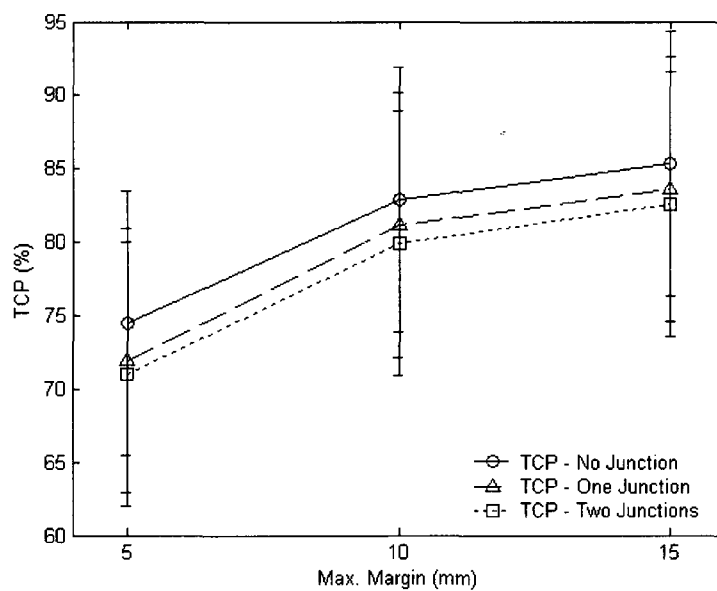


**Figure 5.7** Comparison of the TCP curves as a function of the maximum margin for no-junction, one-junction and two-junction cases. The field width was 50 mm.

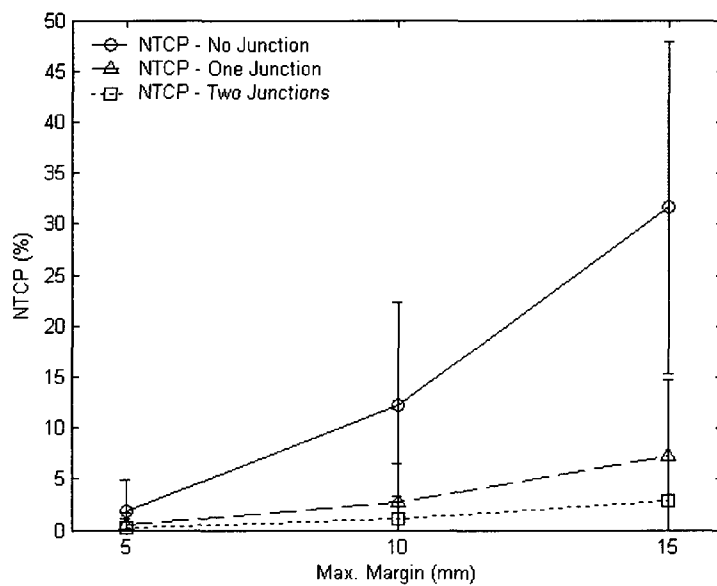


**Figure 5.8** Comparison of the NTCP curves as a function of the maximum margin for no-junction, one-junction and two-junction cases. The field width was 50 mm.

**Table 5.2** TCP and NTCP for iPTV and iPRV for a 20 Gy plan and no-junction. Maximum margins of 5 mm, 10 mm and 15 mm and different field widths of 25 mm and 50 mm are shown.

Field Width	Max. Margin	Probability (%)		
		5 mm	10 mm	15 mm
25 mm	TCP	75 ( $\pm 9$ )	83 ( $\pm 9$ )	84 ( $\pm 9$ )
	NTCP	2 ( $\pm 3$ )	12 ( $\pm 10$ )	29 ( $\pm 16$ )
50 mm	TCP	75 ( $\pm 9$ )	83 ( $\pm 9$ )	85 ( $\pm 9$ )
	NTCP	2 ( $\pm 3$ )	12 ( $\pm 10$ )	32 ( $\pm 16$ )

**Table 5.3** TCP and NTCP for iPTV and iPRV for a 20 Gy plan and one-junction. Maximum margins of 5 mm, 10 mm and 15 mm and different field widths of 25 mm and 50 mm are shown.

Field Width	Max. Margin	Probability (%)		
		5 mm	10 mm	15 mm
25 mm	TCP	72 ( $\pm 9$ )	81 ( $\pm 9$ )	83 ( $\pm 9$ )
	NTCP	0.5 ( $\pm 1.2$ )	3 ( $\pm 4$ )	6 ( $\pm 7$ )
50 mm	TCP	72 ( $\pm 9$ )	81 ( $\pm 9$ )	84 ( $\pm 9$ )
	NTCP	0.5 ( $\pm 1.2$ )	3 ( $\pm 4$ )	7 ( $\pm 7$ )

**Table 5.4** TCP and NTCP for iPTV and iPRV for a 20 Gy plan and two-junctions. Maximum margins of 5 mm, 10 mm and 15 mm and different field widths of 25 mm and 50 mm are shown.

Field Width	Max. Margin	Probability (%)		
		5 mm	10 mm	15 mm
25 mm	TCP	71 ( $\pm 9$ )	80 ( $\pm 9$ )	82 ( $\pm 9$ )
	NTCP	0.3 ( $\pm 0.8$ )	1 ( $\pm 2$ )	2 ( $\pm 4$ )
50 mm	TCP	71 ( $\pm 9$ )	80 ( $\pm 9$ )	83 ( $\pm 9$ )
	NTCP	0.3 ( $\pm 0.8$ )	1 ( $\pm 2$ )	3 ( $\pm 4$ )

The probability of uncomplicated cure defined in Chapter 3 as the product of TCP(1-NTCP) was used to compare the outcomes between no-*junction*, one-*junction* and two-*junction* cases for different maximum margins. Higher values of uncomplicated cure probability represent simultaneously larger values of TCP and lower values of NTCP. Figure 5.9 shows the probability of uncomplicated cure as a function of number of junctions for maximum margins of 5 mm, 10 mm and 15 mm. The probability of uncomplicated cure ranged between 71% and 74% for 5 mm of maximum margin, which represent only 3% difference between no-*junction* and two-*junction* cases. The low probabilities are mainly determined by the low TCP values obtained for 5 mm margins compared to 10 mm and 15 mm of maximum margins as confirmed in Tables 5.2, 5.3 and 5.4.

The largest difference was seen for 15 mm of a magnitude of 22% between no-*junction* and two-*junction* cases. Higher probabilities of uncomplicated cure were found for one- and two-*junction* cases and larger maximum margins of 10 mm and 15 mm. These large probabilities resulted from the lower NTCP values obtained splitting the treatment into two or three sub-treatments.

## **5.4 Discussion**

The DVHs of iPRV and IPTV in Figure 5.6 showed the dosimetric advantages of longitudinally dividing the treatments into two or three sub-treatments. The

sparing effect of splitting the treatment into two or three sub-treatments was also seen from TCP and NTCP estimates.

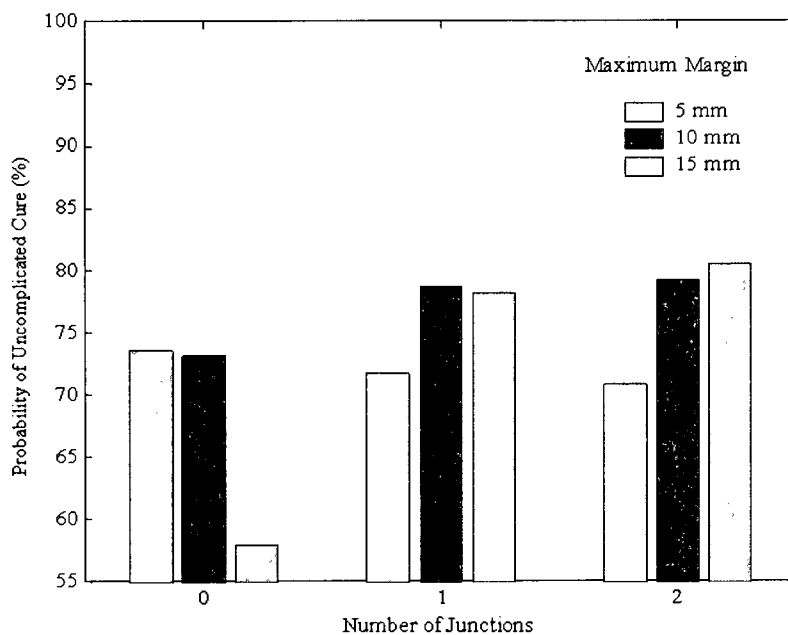


**Figure 5.9** Probability of uncomplicated cure estimates for no-junction, one-junction and two-junction cases and different maximum margins. The field width was 50 mm.

The NTCP and TCP curves as a function of the maximum margin were shown in Figures 5.7 and 5.8 for the three cases studied: no-junction, one-junction and two-junctions. TCP estimates are less affected by the treatment splitting procedure than NTCP since the treatment planning system gives the maximal importance to the PTV coverage. In contrast, the choice of maximum margin strongly affected the NTCP estimates for the no-junction case as seen in Figure

5.7. This is caused by the increased margins to the PTV, which translates into higher doses to the normal surrounding organs. The figure also showed less dependence on the maximum margin used for one-junction and two-junction cases.

NTCP values did not show significant differences between treatments with 25 mm and 50 mm field widths as seen in Tables 5.2, 5.3 and 5.4. This is expected since we have already seen in Chapter 3 for a patient's TMI plan that for large structures of the torso like lungs there was no substantial difference between NTCP estimates using 25 mm or 50 mm fields.

There was no substantial difference either between TCP values using 25 mm or 50 mm as seen in Tables 5.2, 5.3 and 5.4, which was also observed in Chapter 3.

Since we were interested in simultaneously increasing TCP and decreasing NTCP, the probability of uncomplicated cure in Figure 5.9 as a function of number of junctions for the three maximum margins analyzed was plotted. From this analysis, the advantages of splitting spatially and longitudinally large treatments into a few sub-treatments can be seen. This is due to the closeness between the OARs and the PTV and the constraints associated with these structures in the planning system.

Using very small margins lower TCP values were obtained compared to larger margins. On the other hand, 5 mm of maximum margin for maximum structure length of 23.4 cm implies that 5 mm uncertainty is expected at 23.4 cm from the position of the patient and setup alignment and 2.5 mm at half of that distance. This may be unrealistic in an actual clinical situation.

Using larger maximum margins and one- and two-junctions resulted in higher probabilities of uncomplicated cure compared to no-junction and larger margins. These large probabilities resulted from the lower NTCP values obtained splitting the treatment into two or three sub-treatments.

Summarizing, Figure 5.10 shows the TCP vs. NTCP estimates for no-junction, one-junction and two-junction cases and different maximum margins. The field width in the example shown was 50 mm. The probability space was also divided into four quadrants (I, II, III and IV). The regions were divided assuming 80% as the lower limit of the accepted tumour control and 5% as the maximum normal tissue complication probability. A complication probability of 5% is considered the usual acceptable value in clinical radiation oncology. The 80 % of TCP was used since we are expecting about 78% of tumour control in 20 Gy TMI for patient. Even if other values had been used in the plot, the results are still valid on relative basics.

This graph illustrates the interrelation between the maximum margin used (which denotes the increasing uncertainty from the patient and setup alignment), the

number of sub-treatments or junctions (which represents the image-guided spatial frequency) and the radiobiological outcome of the treatment plan (which implies TCP and NTCP).

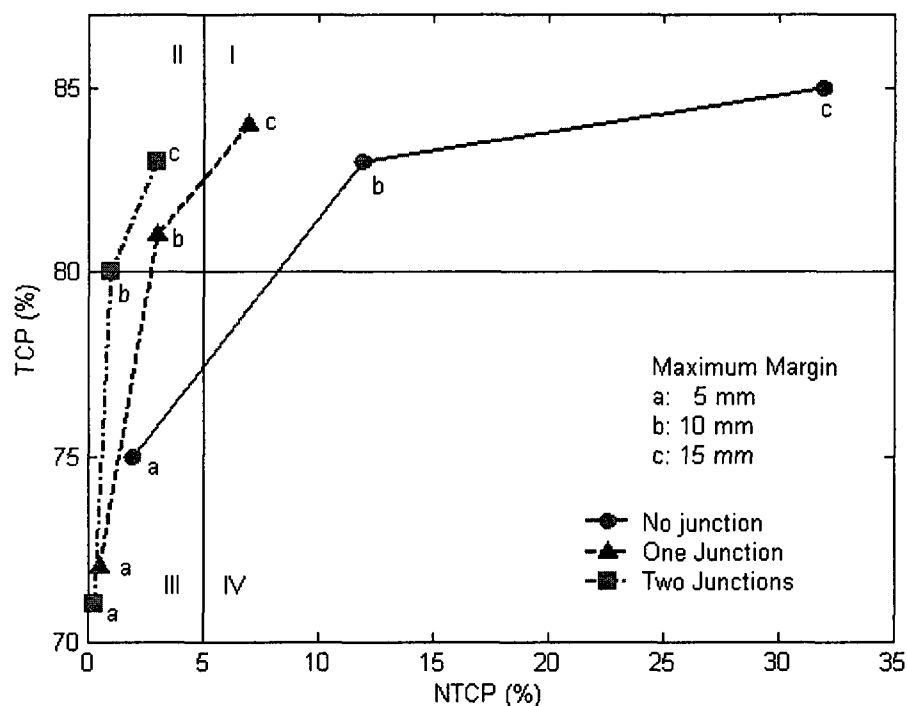


**Figure 5.10** TCP vs. NTCP estimates for no-junction, one-junction and two-junction cases and different maximum margins. The field width was 50 mm. The figure has been divided into four quadrants by two lines at NTCP=5% and TCP= 80%. The second quadrant shows the region for a successful treatment.

Analyzing quadrant III it can be seen that for smaller margins (max. margin of 5 mm) much lower toxicities were obtained. However, tumour control rate was also lower. Quadrant IV is prohibited since it leads to low TCP and high NTCP values. Quadrant I, represented by larger margins and unsplit or just one junction

treatment, gave the highest tumour control rates, but at the expense of larger normal tissue complications.

The second quadrant hypothetically shows the region for a successful TMI treatment plan, for which 80% of tumour control and 5% of normal tissue complication were assumed. Medium and large margins were in this category, but splitting the treatment into two or three sub-treatments (one- or two-junctions) was necessary to reduce lung toxicities.

Even though the values obtained in this study are specific to the geometric setup and treatment planning constraints used in the analysis, this work illustrates the dosimetric advantages of longitudinally dividing the treatments into two or three sub-treatments. The study also illustrates the radiobiological benefits from this procedure. Increasing uncertainties with distance from the registration point can be reduced by splitting large treatments and realigning the patients prior to each sub-treatment. This technique reduces the NTCP and marginal misses of the PTV.

# Chapter 6

## Conclusions

### 6.1 Summary

New clinical trials have been developed for a more targeted treatment in MM patients using HT. The aim of this study was to provide a tool for comparing and predicting the effectiveness of different approaches to TMI using HT. The primary goal was to perform a radiobiological evaluation of different treatment cohorts in a dose escalating study. Due to the lack of dose response data for MM, the expected dose response for plasma cell neoplasms was computed from published clinical data. These results were used to evaluate tumour control. The assessment of treatment-related normal tissue toxicities was based on the parameters obtained from the results published by Burman *et al.*<sup>39</sup> by fitting the

tolerance data for many organs and compiled by Emami *et al.*<sup>40</sup> NTCP and TCP models were applied to an actual TMI treatment plan for a patient.

A secondary goal was to assess the implications of using different longitudinal field widths with the goal of reducing planning and delivery time while maintaining TCP, without causing unacceptable increases in NTCP. Using different field widths within one treatment implies dividing the treatment into a few sub-treatments with different field widths and junctioning longitudinally adjacent PTVs. The parameters which influence the cumulative dose distribution resulting from treating longitudinally adjacent PTVs were examined, including field width, pitch, and PTV location.

An optimal delivery of a very conformal dose distribution requires precise patient positioning. The benefits of spatially dividing the treatment into a few sub-treatments along the longitudinal direction were also analyzed. This technique not only allowed superior patient alignment by imaging the patient a few times during one treatment fraction, resulting in greater confidence in patient setup and treatment delivery, but also resulted in lower toxicities to the normal tissues while achieving similar local control rates.

Although the studies included in this thesis are all interrelated, this work embraced several aspects of TMI. More detailed and separate conclusions for each chapter were considered to be beneficial for the readers.

## 6.2 Conclusions from Chapter 2

An extensive review of published plasmacytoma clinical data was performed. Even though the data suffer from a lack of low dose information and most of the data is reported within a dose range, this approach is a sound assessment of the dose response relationship for plasma cell neoplasms.

The parameters of the TCP empirical model were determined for EMP, SPB and SPB+EMP. Because of the common association between SPB and MM, an extra set of parameters were determined fitting clinical SPB data and a 12 Gy TBI data point (12 Gy TBI has been used with little success in treating MM). A significant difference was seen between the dose response for extramedullary plasmacytomas and solitary plasmacytomas of the bones, with EMP showing greater radioresistance than SPB. These radiation response parameters can be useful for extrapolating clinical dose response data, providing estimates of tumour control probability in the assessment of new therapies and comparing different treatment planning approaches.

## 6.3 Conclusions from Chapter 3

Using the tumour response data determined in Chapter 2 and published normal tissue response data, TCP and NTCP were estimated for a virtual TMI patient, originally receiving 20 Gy and linearly escalating the DVHs to higher doses.

There was no substantial difference between TCP using 25 or 50 mm field width, nor between NTCP values for organs in the torso. The sparing effect seen by using smaller fields in the organs of the head suggests it would be beneficial to use the small field width in the head only; using such small fields for the whole treatment would lead to long treatment times.

Lungs were the most important organs at risk in TMI for which the optimum choice of prescription dose in a TMI treatment was found to be about 39 Gy. This resulted in a calculated value of 95% tumour control and 3% rate of radiation pneumonitis.

#### **6.4 Conclusions from Chapter 4**

Longitudinal junctioning with HT is possible. Junction errors are smaller with larger field widths. Optimal junction spacing may always be found with acceptable dose distributions. Junctioning using different field widths is more difficult than junctioning fields of the same width. However, breaking PTVs into multiple contiguous PTVs with a modified prescription near the junction will extend the effective junction region reducing junction dose heterogeneity from matching fields of different widths.

Feasibility of longitudinal field junctioning while achieving reasonably homogeneous dose distributions with HT extends this technique to clinical

situations where dose to contiguous PTVs are planned or delivered independently (e.g. retreatments).

## **6.5 Conclusions from Chapter 5**

The benefits of spatially dividing or splitting the treatment fraction into a few sub-treatments along the longitudinal direction were analyzed. This technique, which allows superior patient alignment by imaging the patient a few times during one treatment fraction, resulted in higher values of probability of uncomplicated cure.

Using larger maximum margins and one- and two-junctions resulted in higher probabilities of uncomplicated cure compared to the case of no-junction and larger margins. Increasing uncertainties with distance from the registration point can be reduced by splitting large treatments and realigning the patients prior to each sub-treatment. This technique reduces the NTCP and marginal misses of the PTV.

## **6.6 Future directions**

In this study several issues were addressed. A radiobiological evaluation of different treatment cohorts in a dose escalation study and the benefits of spatial image guidance frequency in TMI were performed. The dosimetric challenges

that arise when junctioning longitudinally adjacent PTVs and clinically viable solutions were examined. The implications of using different longitudinal field lengths with the final objective of reducing planning and delivery time without causing unacceptable increases in normal tissue toxicities while achieving similar tumour control were also analyzed.

This study provides scientific background for a *phase III* dose escalation clinical trial using IG-IMRT to deliver high dose to the entire volume of bone marrow with HT. It establishes a rationale for using HT for TMI and guides the choice of maximum dose for patients with MM. The radiobiological modeling was performed from the extension of clinical data from other studies to models of expected tumour control probability and normal tissue complication probability.

More specific results will be found from analyzing the patient response data from the clinical trial, since it has been designed to determine not just the feasibility, but the maximum tolerable dose and a preliminary assessment of the effectiveness of the treatment, including overall survival, progression free survival and validity of the mathematical radiobiological parameters. A detailed radiation dose response will be obtained for these patients since different cohorts consisting of a minimum of 14 Gy up to 28 Gy every 2 Gy will be evaluated. As of September 2009, the clinical trial is open at The Ottawa Hospital Cancer Centre, and has recruited one patient for treatment in January 2010.

# Appendix A

## TMI clinical trial overview

In this appendix the phase I/II of the new TMI clinical trial is briefly introduced.<sup>70</sup> The study has been approved at The Ottawa Hospital Cancer Center by The Ottawa Hospital Research Ethics Board. Only the details that have relevance to this thesis are included.

The complete title of the clinical study is “A dose escalation study of total marrow irradiation and autologous stem cell transplantation for the treatment of relapse or refractory multiple myeloma”. The investigator and co-investigators and their field of expertise are listed in Table A.1.

**Table A.1** Investigators involved in the TMI clinical trial and their field of expertise

Principal Investigators	
Rajiv Samant	Radiation Oncology
Lee Gerig	Medical Physics
Harold Atkins	Bone Marrow Transplantation
Co-Investigators	
Peter Cross	Radiation Oncology
Lothar Huebsch	Bone Marrow Transplantation
Greg Fox	Radiation Technologist
Lourdes Garcia	Radiation Biology
Miller McPherson	Medical Physics
Lynn Montgomery	Radiation Technologist
Peter Raaphorst	Radiation Biology
Dave Wilkins	Radiation Biology

## A.1 Study aim and rationale

The study aim as written in the protocol is "... to determine the feasibility, safety and maximum tolerated dose of TMI that can be delivery to the entire skeleton using IG-IMRT techniques with helical tomotherapy unit" and "...to determine if

this radiotherapy treatment delivery approach can lead to clinical meaningful response for patients with multiple myeloma.<sup>70</sup>

Some of the rationales for this study have been discussed in Chapters 2 and 3 of this thesis. Radiation therapy is a potentially curative modality as indicated by the high radiosensitivity of myeloma and the long-term control of localized plasmacytomas in MM. In addition, new IMRT technologies such as HT allow to deliver very conformal dose distribution reducing the dose to normal tissues. Using a conventional RT modality, the treatment of MM patients is limited to the doses used in TBI because of radiation induced organ dysfunction. The primary objective is to determine the maximum tolerated dose of TMI when followed by stem cell transplantation.

## **A.2 Treatment overview**

Patients with advanced or refractory MM will receive a dose of radiation to the bone marrow using HT. There will be eight different levels of radiation. One cohort consists of at least three patients receiving one level of radiation. The initial cohort of patients will receive 14 Gy TMI in 7 fractions of 2 Gy each. Usually 12 Gy in 6 fractions is the standard delivery for TBI when used in stem transplant conditioning regimens. In additional cohorts, a 2 Gy fraction of radiation will be added to the treatment until the maximum tolerated dose occurs.

The maximum radiation dose level included in the study will be 28 Gy in 8 fractions.

In order to determine the maximum tolerated dose to the patients, the limiting toxicity based upon specific organ toxicities were identified by the Regimen Related Toxicity Scale.<sup>71</sup> During the planning, the volume of marrow receiving the prescribed dose is maximized while minimizing the radiation dose to the normal organs. The radiation doses to normal organs are constrained to keep it below the accepted levels of radiation tolerance. The tolerance dose for the most important organ at risk were reported and referenced in Table 3.1 in Chapter 3.

The duration of the study it is expected to be between 3 and 5 years with recruitment of about 6-8 patients per year.

### **A.3 TMI radiobiological modeling**

TMI of MM patients in a new dose escalating clinical trial offers the opportunity to develop and test radiobiological model of normal tissue complication (NTCP) and tumour control (TCP). The distribution of radiation dose from the patients can be obtained from the TPS and are very close to the actual dose received by the patients. Each of the patients enrolled will have a treatment plan resulting in a 3D matrix with the dose distribution in the body, as well as clinical information

assessing normal tissue toxicity and measures of tumour control such as disease free survival and progression.

In Chapter 2 the radiation dose response for MM was estimated from the little information that could be found in the literature. Following the patient responses from the trial, we will have the possibility to verify the TCP model and introduce new feedbacks in the analysis while reducing the uncertainty associated with some of the limitations of the preliminary model discussed in Chapter 2.

The results of the clinical trial could also be used to refine the parameter estimates of the NTCP models for many organs at risk and compare with previously published values.

## Appendix B. Conferences and publications

### Conferences

- Radiation dose response of plasma cell neoplasms. AAPM, 51st Annual Meeting. Anaheim, California, 2009.
- Radiobiological modeling of a proposed dose escalation in TMI. Canadian Organization of Medical Physicists COMP 55th Annual Scientific Meeting. Victoria, Canada, 2009.
- Feasibility study of longitudinal field junctioning with helical tomotherapy. AAPM, 50th Annual Meeting. Houston. Texas, 2008
- Field junctions with helical tomotherapy. Canadian Organization of Medical Physicists COMP 53rd Annual Scientific Meeting. Toronto, Canada, 2007.

### Publications

- **Garcia, L., Nyiri, B., Wilkins, D., Gerig, L., Atkins, H., Samant, R. and Raaphorst, G.** Radiation dose response of plasma cell neoplasms. *Radiotherapy and Oncology*. (Submitted, 2009)
- **Garcia, L., Gerig, L., Raaphorst, G. And Wilkins, D.** Junctioning of longitudinally adjacent PTVs with helical tomotherapy. *Journal of Applied Clinical Medical Physics* (Accepted, 2009)

# References

1. Wiltshaw E. The natural history of extramedullary plasmacytoma and its relation to solitary myeloma of bone and myelomatosis. *Medicine (Baltimore)* 1976;55(3):217-38.
2. Kyle RA, Rajkumar SV. Multiple myeloma. *N Engl J Med* 2004;351(18):1860-73.
3. Ozsahin M, Tsang RW, Poortmans P, Belkacemi Y, Bolla M, Dincbas FO, et al. Outcomes and patterns of failure in solitary plasmacytoma: a multicenter Rare Cancer Network study of 258 patients. *Int J Radiat Oncol Biol Phys* 2006;64(1):210-7.
4. Shih LY, Dunn P, Leung WM, Chen WJ, Wang PN. Localised plasmacytomas in Taiwan: comparison between extramedullary plasmacytoma and solitary plasmacytoma of bone. *Br J Cancer* 1995;71(1):128-33.
5. Tsang RW, Gospodarowicz MK, Pintilie M, Bezjak A, Wells W, Hodgson DC, et al. Solitary plasmacytoma treated with radiotherapy: impact of tumor size on outcome. *Int J Radiat Oncol Biol Phys* 2001;50(1):113-20.

6. McAfee SL, Powell SN, Colby C, Spitzer TR. Dose-escalated total body irradiation and autologous stem cell transplantation for refractory hematologic malignancy. *Int J Radiat Oncol Biol Phys* 2002;53(1):151-6.
7. Hui SK, Kapatoes J, Fowler J, Henderson D, Olivera G, Manon RR, et al. Feasibility study of helical tomotherapy for total body or total marrow irradiation. *Med Phys* 2005;32(10):3214-24.
8. Hui SK, Verneris MR, Higgins P, Gerbi B, Weigel B, Baker SK, et al. Helical tomotherapy targeting total bone marrow - first clinical experience at the University of Minnesota. *Acta Oncol* 2007;46(2):250-5.
9. Schultheiss TE, Wong J, Liu A, Olivera G, Somlo G. Image-guided total marrow and total lymphatic irradiation using helical tomotherapy. *Int J Radiat Oncol Biol Phys* 2007;67(4):1259-67.
10. Wong JY, Liu A, Schultheiss T, Popplewell L, Stein A, Rosenthal J, et al. Targeted total marrow irradiation using three-dimensional image-guided tomographic intensity-modulated radiation therapy: an alternative to standard total body irradiation. *Biol Blood Marrow Transplant* 2006;12(3):306-15.
11. Wong JY, Rosenthal J, Liu A, Schultheiss T, Forman S, Somlo G. Image-guided total-marrow irradiation using helical tomotherapy in patients with multiple myeloma and acute leukemia undergoing hematopoietic cell transplantation. *Int J Radiat Oncol Biol Phys* 2009;73(1):273-9.
12. Gotoh S. [Revolution in radiation therapy: TomoTherapy HI-ART system]. *Nippon Hoshasen Gijutsu Gakkai Zasshi* 2006;62(12):1611-9.
13. Mackie TR. History of tomotherapy. *Phys Med Biol* 2006;51(13):R427-53.

14. Mackie TR, Holmes T, Swerdloff S, Reckwerdt P, Deasy JO, Yang J, et al. Tomotherapy: a new concept for the delivery of dynamic conformal radiotherapy. *Med Phys* 1993;20(6):1709-19.
15. Knobel D, Zouhair A, Tsang RW, Poortmans P, Belkacemi Y, Bolla M, et al. Prognostic factors in solitary plasmacytoma of the bone: a multicenter Rare Cancer Network study. *BMC Cancer* 2006;6:118.
16. Holland J, Trenkner DA, Wasserman TH, Fineberg B. Plasmacytoma. Treatment results and conversion to myeloma. *Cancer* 1992;69(6):1513-7.
17. Brinch L, Hannisdal E, Abrahamsen AF, Kvaloy S, Langholm R. Extramedullary plasmacytomas and solitary plasma cell tumours of bone. *Eur J Haematol* 1990;44(2):132-5.
18. Corwin J, Lindberg RD. Solitary plasmacytoma of bone vs. extramedullary plasmacytoma and their relationship to multiple myeloma. *Cancer* 1979;43(3):1007-13.
19. Strojjan P, Soba E, Lamovec J, Munda A. Extramedullary plasmacytoma: clinical and histopathologic study. *Int J Radiat Oncol Biol Phys* 2002;53(3):692-701.
20. Frassica FJ, Sim FH, Wold LE. Case report 462: Grade 2 myxoid fibrosarcoma of femur. *Skeletal Radiol* 1988;17(1):77-80.
21. Susnerwala SS, Shanks JH, Banerjee SS, Scarffe JH, Farrington WT, Slevin NJ. Extramedullary plasmacytoma of the head and neck region: clinicopathological correlation in 25 cases. *Br J Cancer* 1997;75(6):921-7.
22. Warkentin B, Stavrev P, Stavreva N, Field C, Fallone BG. A TCP-NTCP estimation module using DVHs and known radiobiological models and parameter sets. *J Appl Clin Med Phys* 2004;5(1):50-63.

23. Brandt S. Statistical and computational methods in data analysis. Rev. ed. Amsterdam; New York: North-Holland Pub. Co.; American Elsevier Pub. Co.; 1976.
24. Cowan G. Statistical data analysis. Oxford; New York: Clarendon Press; Oxford University Press; 1998.
25. Eadie WTea. Statistical Methods in Experimental Physics. North-Holland; Amsterdam; 1971.
26. Shank B, Chu FC, Dinsmore R, Kapoor N, Kirkpatrick D, Teitelbaum H, et al. Hyperfractionated total body irradiation for bone marrow transplantation. Results in seventy leukemia patients with allogeneic transplants. *Int J Radiat Oncol Biol Phys* 1983;9(11):1607-11.
27. Jyothirmayi R, Gangadharan VP, Nair MK, Rajan B. Radiotherapy in the treatment of solitary plasmacytoma. *Br J Radiol* 1997;70(833):511-6.
28. Chao MW, Gibbs P, Wirth A, Quong G, Guiney MJ, Liew KH. Radiotherapy in the management of solitary extramedullary plasmacytoma. *Intern Med J* 2005;35(4):211-5.
29. Dimopoulos MA, Goldstein J, Fuller L, Delasalle K, Alexanian R. Curability of solitary bone plasmacytoma. *J Clin Oncol* 1992;10(4):587-90.
30. Chang MY, Shih LY, Dunn P, Leung WM, Chen WJ. Solitary plasmacytoma of bone. *J Formos Med Assoc* 1994;93(5):397-402.
31. Aviles A, Huerta-Guzman J, Delgado S, Fernandez A, Diaz-Maqueo JC. Improved outcome in solitary bone plasmacytomata with combined therapy. *Hematol Oncol* 1996;14(3):111-7.

32. Mayr NA, Wen BC, Hussey DH, Burns CP, Staples JJ, Doornbos JF, et al. The role of radiation therapy in the treatment of solitary plasmacytomas. *Radiother Oncol* 1990;17(4):293-303.
33. Okunieff P, Morgan D, Niemierko A, Suit HD. Radiation dose-response of human tumors. *Int J Radiat Oncol Biol Phys* 1995;32(4):1227-37.
34. Marks LB. Target volume (TV) radiation dose heterogeneities. *Eur J Cancer* 1993;29(Suppl.6):1236.
35. Thames HD, Schultheiss TE, Hendry JH, Tucker SL, Dubray BM, Brock WA. Can modest escalations of dose be detected as increased tumor control? *Int J Radiat Oncol Biol Phys* 1992;22(2):241-6.
36. Chappell R, Fowler JF. Steepness of dose-response curve for larynx cancer. *Radiother Oncol* 1994;30(1):90.
37. Lyman JT. Complication probability as assessed from dose-volume histograms. *Radiat Res Suppl* 1985;8:S13-9.
38. Cozzi L, Buffa FM, Fogliata A. Comparative analysis of dose volume histogram reduction algorithms for normal tissue complication probability calculations. *Acta Oncol* 2000;39(2):165-71.
39. Burman C, Kutcher GJ, Emami B, Goitein M. Fitting of normal tissue tolerance data to an analytic function. *Int J Radiat Oncol Biol Phys* 1991;21(1):123-35.
40. Emami B, Lyman J, Brown A, Coia L, Goitein M, Munzenrider JE, et al. Tolerance of normal tissue to therapeutic irradiation. *Int J Radiat Oncol Biol Phys* 1991;21(1):109-22.

41. Baisden JM, Benedict SH, Sheng K, Read PW, Larner JM. Helical TomoTherapy in the treatment of central nervous system metastasis. *Neurosurg Focus* 2007;22(3):E8.
42. Bauman G, Yartsev S, Fisher B, Kron T, Laperriere N, Heydari M, et al. Simultaneous infield boost with helical tomotherapy for patients with 1 to 3 brain metastases. *Am J Clin Oncol* 2007;30(1):38-44.
43. Bauman G, Yartsev S, Rodrigues G, Lewis C, Venkatesan VM, Yu E, et al. A prospective evaluation of helical tomotherapy. *Int J Radiat Oncol Biol Phys* 2007;68(2):632-41.
44. Higgins PD, Han EY, Yuan JL, Hui S, Lee CK. Evaluation of surface and superficial dose for head and neck treatments using conventional or intensity-modulated techniques. *Phys Med Biol* 2007;52(4):1135-46.
45. Orton N, Jaradat H, Welsh J, Tome W. Total scalp irradiation using helical tomotherapy. *Med Dosim* 2005;30(3):162-8.
46. Penagaricano JA, Papanikolaou N, Yan Y, Youssef E, Ratanatharathorn V. Feasibility of cranio-spinal axis radiation with the Hi-Art tomotherapy system. *Radiother Oncol* 2005;76(1):72-8.
47. Penagaricano JA, Shi C, Ratanatharathorn V. Evaluation of integral dose in cranio-spinal axis (CSA) irradiation with conventional and helical delivery. *Technol Cancer Res Treat* 2005;4(6):683-9.
48. Sheng K, Molloy JA, Read PW. Intensity-modulated radiation therapy (IMRT) dosimetry of the head and neck: a comparison of treatment plans using linear accelerator-based IMRT and helical tomotherapy. *Int J Radiat Oncol Biol Phys* 2006;65(3):917-23.

49. Welsh JS, Mehta MP, Mackie TR, Orton N, Jaradat H, Khuntia D, et al. Helical tomotherapy as a means of delivering scalp-sparing whole brain radiation therapy. *Technol Cancer Res Treat* 2005;4(6):661-2; author reply 62.
50. Grigorov G, Kron T, Wong E, Chen J, Sollazzo J, Rodrigues G. Optimization of helical tomotherapy treatment plans for prostate cancer. *Phys Med Biol* 2003;48(13):1933-43.
51. Kupelian PA, Langen KM, Zeidan OA, Meeks SL, Willoughby TR, Wagner TH, et al. Daily variations in delivered doses in patients treated with radiotherapy for localized prostate cancer. *Int J Radiat Oncol Biol Phys* 2006;66(3):876-82.
52. Rodrigues G, Yartsev S, Chen J, Wong E, D'Souza D, Lock M, et al. A comparison of prostate IMRT and helical tomotherapy class solutions. *Radiother Oncol* 2006;80(3):374-7.
53. Mahan SL, Ramsey CR, Scaperoth DD, Chase DJ, Byrne TE. Evaluation of image-guided helical tomotherapy for the retreatment of spinal metastasis. *Int J Radiat Oncol Biol Phys* 2005;63(5):1576-83.
54. IEC. Radiotherapy equipment-coordinates, movements and scales. IEC1217; 1996.
55. Kissick MW, Fenwick J, James JA, Jeraj R, Kapatoes JM, Keller H, et al. The helical tomotherapy thread effect. *Med Phys* 2005;32(5):1414-23.
56. Yoon M, Park SY, Shin D, Lee SB, Pyo HR, Kim DY, et al. A new homogeneity index based on statistical analysis of the dose-volume histogram. *J Appl Clin Med Phys* 2007;8(2):9-17.

57. Childress NL, Salehpour M, Dong L, Bloch C, White RA, Rosen, II. Dosimetric accuracy of Kodak EDR2 film for IMRT verifications. *Med Phys* 2005;32(2):539-48.
58. Yang JN, Mackie TR, Reckwerdt P, Deasy JO, Thomadsen BR. An investigation of tomotherapy beam delivery. *Med Phys* 1997;24(3):425-36.
59. ICRU. Prescribing, recording, and reporting photon beam therapy. In: ICRU, editor. Report 50. USA; 1993.
60. Jaradat H, Xu L, Lucas G, Lee T. Helical tomotherapy for craniospinal irradiation with field junctioning. Paper presented at: AAPM, 2008; Houston, Texas.
61. Kissick MW, Flynn RT, Westerly DC, Mackie TR, Hoban PW. On the making of sharp longitudinal dose profiles with helical tomotherapy. *Phys Med Biol* 2007;52(21):6497-510.
62. Khan FM. Treatment planning in radiation oncology. Second ed. Philadelphia: Lippincott Williams & Wilkins; 2007.
63. Hong TS, Tome WA, Chappell RJ, Chinnaiyan P, Mehta MP, Harari PM. The impact of daily setup variations on head-and-neck intensity-modulated radiation therapy. *Int J Radiat Oncol Biol Phys* 2005;61(3):779-88.
64. Meijer GJ, Rasch C, Remeijer P, Lebesque JV. Three-dimensional analysis of delineation errors, setup errors, and organ motion during radiotherapy of bladder cancer. *Int J Radiat Oncol Biol Phys* 2003;55(5):1277-87.

65. Pisani L, Lockman D, Jaffray D, Yan D, Martinez A, Wong J. Setup error in radiotherapy: on-line correction using electronic kilovoltage and megavoltage radiographs. *Int J Radiat Oncol Biol Phys* 2000;47(3):825-39.
66. Weber DC, Nouet P, Rouzaud M, Miralbell R. Patient positioning in prostate radiotherapy: is prone better than supine? *Int J Radiat Oncol Biol Phys* 2000;47(2):365-71.
67. Hector CL, Webb S, Evans PM. The dosimetric consequences of inter-fractional patient movement on conventional and intensity-modulated breast radiotherapy treatments. *Radiother Oncol* 2000;54(1):57-64.
68. Li JG, Xing L. Inverse planning incorporating organ motion. *Med Phys* 2000;27(7):1573-8.
69. Samuelsson A, Mercke C, Johansson KA. Systematic set-up errors for IMRT in the head and neck region: effect on dose distribution. *Radiother Oncol* 2003;66(3):303-11.
70. The Ottawa Hospital Research Ethics Board, TOHRE. A dose escalation study of total marrow Irradiation (TMI) and autologous stem cell transplantation (ASCT) for the treatment of relapsed or refractory multiple myeloma (MM); 2009.
71. Bearman SI, Appelbaum FR, Buckner CD, Petersen FB, Fisher LD, Clift RA, et al. Regimen-related toxicity in patients undergoing bone marrow transplantation. *J Clin Oncol* 1988;6(10):1562-8.